C O L U M N A S L I Q U I D A S
E N I N G R A V I D E Z

I N F O R M E F I N A L 1983

Lamf-ETSIA, Laboratorio de Aerodinámica,
E.T.S.I. Aeronáuticos, Ciudad Universitaria,
MADRID-3

EXPEDIENTE CONIE: 514/83

Madrid, Noviembre 1983

Ref.: Lamf 8311e

EXPEDIENTE nº 514/83

COLUMNAS LIQUIDAS EN CONDICIONES DE INGRAVIDEZ-1983

Convenio de Investigación entre la Comisión Nacional de Investigación del Espacio (CONIE) y la Universidad Politécnica de Madrid (UPM), desarrollado por el Laboratorio de Aerodinámica (LAMF) de la Escuela Técnica Superior de Ingenieros Aeronáuticos (ETSIA), durante el año 1983.

Responsable del trabajo... I. Da Riva de la Cavada

Colaboradores ..... I. Martínez Herranz

J. Meseguer Ruiz

A. Sanz Andrés

J.M. Vega de Prada

D. Rivas Rivas

J.M. Perales Perales

INTRODUCCION

El proyecto de investigación sobre el "Comportamiento de Columnas Líquidas en Ingravidez" viene desarrollándose desde 1975 subvencionado por la CONIE, en el Laboratorio de Aerodinámica de la E.T.S.I. Aeronáuticos (UPM).

Los trabajos de este año han sido particularmente importantes, destacando la organización del 4º Simposio Europeo de Ciencia de los Materiales en Microgravedad (en el cual este grupo presentó cinco comunicaciones sobre dichas investigaciones) y el primer vuelo del Spacelab en el que se realizará el experimento español 1-ES-331, que pretende contrastar muchos de los resultados del programa teórico y de simulación en tierra sobre el comportamiento de estos puentes líquidos en condiciones de gravedad reducida.

Con la inestimable ayuda de la Agencia Espacial Europea, se organizó en Madrid, del 5 al 8 de Abril, el citado simposio (continuación de los celebrados en Italia y Francia en años anteriores) en el que, ante una audiencia de 132 científicos de 15 países diferentes, se presentaron 66 artículos sobre el estado actual de la investigación en microgravedad, sobre materiales compuestos y fases heterogéneas, instalaciones experimentales, fenómenos de transporte, combustión e interfases. A este último apartado pertenecen cuatro de los trabajos presentados sobre diversos aspectos de nuestras investigaciones: invariantes de la zona líquida, inestabilidad en rotación, dinámica de la rotura y estabilidad con apoyos no convencionales; y se presentó una quinta ponencia, esta vez en colaboración con la Universidad de Nápoles, sobre el estado actual de la Física de Fluidos en Microgravedad.

Dentro del estudio del comportamiento de las columnas líquidas, merece especial relevancia el análisis de los efectos de la gravedad,

del que tratan dos de los trabajos que se presentan este año; no en vano, la filosofía de todo el proyecto es la de comprender mejor el comportamiento real de estas zonas flotantes en tierra mediante el estudio simplificado en ausencia de gravedad.

Por tanto, una vez analizado con cierto detalle el caso extremo de gravedad nula, parece natural empezar a relajar este fuerte condicionante, que ni siquiera en el vuelo orbital se va a alcanzar, e iniciar el estudio de la influencia de una pequeña gravedad residual (en el Spacelab se espera que sea 10.000 veces menor que en la Tierra), que, para mayor sencillez, se supone alineada con el eje de simetría de la columna.

El problema de la influencia de una microgravedad axial es además fundamental para la evaluación de los resultados experimentales que se obtienen en tierra usando un baño isodenso (tanque de Plateau), pues la precisión requerida en el equilibrado de densidades es muy superior a la que se puede conseguir ajustando con densímetros comunes, y ha de ser utilizada la propia zona como indicador de gravedad residual, necesitándose un conocimiento de la respuesta de la zona, si se quiere llegar a un calibrado preciso.

En cuanto al soporte de los experimentos en el espacio, por fin, tras cuatro años de retraso sobre la fecha prevista, parece ser que va a tener lugar el primer vuelo del Spacelab. Suponemos que cuando salgan a la luz estas páginas ya se habrá llevado a cabo, esperamos que con éxito, esta primera misión, objetivo crucial de este proyecto de investigación.

VOLUMEN 1

CONTENIDO

VOLUMEN 2

CONTENIDO

VOLUMEN 3

CONTENIDO

FLUID PHYSICS UNDER REDUCED GRAVITY – AN OVERVIEW

I. Da-Riva

Aerodynamics Laboratory
Polytechnic University of Madrid, Spain

L.G. Napolitano

Chair of Aerodynamics
University of Naples, Italy

ABSTRACT

Problems related to several fluid physics experiments to be performed under reduced gravity, onboard Spacelab (1st Mission), are discussed. Special attention is placed on parallel and preparatory work on Earth, which could throw some light on the opportunity, present interest and limitations of these experiments.

The need for strong supporting fundamental research and, in particular, a more precise determination of the parameters involved, is stressed.

Keywords: Microgravity, Spacelab, Spreading of liquids, Surface tension, Contact angle, Liquid bridges, Drops, Marangoni convection.

1. INTRODUCTION

Research in low-gravity fluid physics started in Europe in the middle sixties with the aim of solving problems posed by fluid management in spacecraft. Typical problems were, sloshing, thermal control, capillary liquid retention, gauging of partially filled tanks, etc. Refs. 1 to 5.

On the other hand, industrial processes based on the freezing during free-fall of drops (manufacture of hunting small shots, glass fibers,...) use other than normal gravity conditions at least for short times.

Finally, studies on capillary-dominated fluid configurations, which are relevant to microgravity, were undertaken in the 19th century by scientists quite unaware of the feasibility of orbital laboratories. The names of such distinguished men as Young, Laplace, Gauss, Plateau, Rayleigh should be mentioned in this regard.

Nevertheless, our history begins in 1974 when ESRO (the forerunner of ESA) issued an "invitation to submit ideas for the definition of the experimental objectives for the First Spacelab Mission".

From the nearly 80 ideas received, 13 dealt with pure fluid physics, although several more were in the never clearly defined fringe between fluid physics and material sciences.

Most of the ideas concerning fluid physics were accepted, and those rejected were on the basis of foreseable technical difficulties. This was, for example, the case of two experiments requiring liquid helium temperatures.

The accepted ideas were accomodated in the Fluid Physics Module, and the incorporation of so many conflicting requirements into a single apparatus was not a mean task for which FIAT CR, the developer, should be praised.

2. THE PLATFORMS

Figure 1 shows the microgravity capabilities of three types of platforms which are being used or will be used in the near future to perform experiments under reduced gravity conditions.

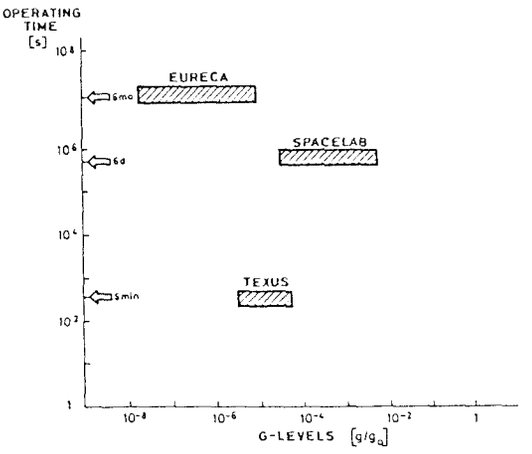

Figure 1. Operating time vs. gravitational levels with three microgravity platforms.

TEXUS Sounding Rocket Programme was initiated in 1976. It is sponsored and financed by the German Ministry of Research and Technology and administered by the DFVLR.

The carrier is the Skylark VII which provides for approximately 6 min of free-fall conditions, with residual accelerations below 10^{-4} g, for a payload

Proceedings of the 4th European Symposium on Materials Sciences under Microgravity, *Madrid, Spain*, 5-8 *April* 1983 (*ESA SP*-191 – *June* 1983).

in the range 330 to 350 kg.

The rockets are launched from ESRANGE, near Kiruna, Sweeden, in cooperation with the Swedish Space Corporation.

Up to the moment six TEXUS Missions have been accomplished. TEXUS VII and VIII are scheduled for April/May 1983.

An overview of experiments conducted so far under TEXUS programme is presented in Ref. 6.

SPACELAB is a modular facility carried a board the Space Shuttle Orbiter. It consists of an enclosed, pressurized laboratory instrumented for the conduct of experiments, and outside platforms where telescopes, antennae and sensors are mounted for direct exposure to space.

SPACELAB is a cooperative venture of ESA and NASA. ESA is responsible for funding, developing and building SPACELAB. NASA is responsible for the launch and operational use.

First SPACELAB Mission is scheduled for September 1983. Second (D1) will follow in 1985.

SPACELAB 1 carries the so called Material Sciences Double Rack (MSDR) where most of the Material Sciences experiments will be performed. Fluid Physics experiments will use the Fluid Physics Module (FPM) which is a part of the MSDR package.

The FPM has been developed by Centro Ricerche Fiat under the sponsorship of the Italian CNR. For recent descriptions of this facility see Refs. 7 and 8.

EURECA is a retrievable space platform the development of which has been recently approved by ESA Member States.

The spacecraft will be launched from and retrieved by the Space Shuttle. Operational lifetime will be 6 months.

The payload, of approximately 1100 kg, will consist of up to six multiuser facilities for processing metallurgical samples and performing botanical investigations. In addition, suit-case type experiments, up to 200 kg in total, can be accommodated.

First EURECA mission is planned for 1987.

3. FIRST SPACELAB MISSION EXPERIMENTS

The experiments, related to low-gravity fluid physics, planned for the first Spacelab mission are sketched in Figure 2.

3.1 Oscillations of a partially free drop

The oscillations of a drop supported on -and disturbed from- an axisymmetric disc are being considered in experiment 1 ES 326. Experimental results by use of the Plateau simulation technique have been reported (Refs. 9-11).

At present there is not analytical tool, even simplified, to evaluate these results. The application of Lamb's linear potential theory for a nearly-spherical liquid drop freely oscillating in an infinite mass of another liquid (Ref. 12) hardly can be justified, since the boundary conditions at the supporting disc couple modes of deformation which in Lamb's solution remain uncoupled. The situation resembles the analogy between a jet and a liquid bridge to be discussed in §3.4.

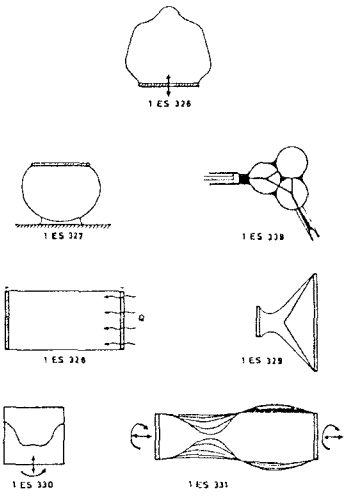

Figure 2. First Spacelab mission experiments on fluid physics.

1 ES 326 Oscillation damping of a liquid in natural levitation.
1 ES 327 Kinetics of spreading of liquids on solids.
1 ES 328 Free convection in low gravity.
1 ES 329 Capillary surfaces in low gravity.
1 ES 330 Coupled motion of liquid-solid systems in near zero gravity.
1 ES 331 Floating zone stability in low gravity.
1 ES 339 Interfacial instability and capillary hysteresis.

The two more relevant results from the above mentioned experiments are:

1. The fundamental frequency varies with the drop diameter, D, as D^{-2}. Inviscid linear analysis predicts $D^{-1.5}$.
2. Extrapolation of experimental data to vanishing supporting-disc radii suggest that an equatorial nodal circle appears for the lowest mode. Lamb's analysis predicts two nodal circles in the North and South hemispheres, respectively.

The difference is due to the very concentrated disturbance resulting in the limit of zero disc radius.

These experiments were performed with kinematic viscosities in the range 5 Cst - 100 Cst.

Neglecting viscosity effects, on the other hand, is certainly justified. Trinh, Zwern & Wang (Ref. 13) measured, by use of the acoustic supporting (and disturbing) technique, the lowest resonance frequencies, as well as the first mode damping constant for a liquid drop oscillating in another liquid of the same density. Viscosities where in the range 1.22 Cst to 124 Cst. For small amplitudes, $\Delta D/D < .1$, the first mode frequency varied as $D^{-1.51}$, close to Lamb's prediction. The damping constant, on the other hand, agreed with results of available viscous linearized theories. The comparison is not so good for higher modes.

Large amplitude oscillations, $\Delta D/D > .1$, have been also explored (Ref. 14). Nonlinear effects on the fundamental resonant frequency are not large, but internal flow patterns not directly predictable by linear theories have been detected.

The influence of surface tension on the above results can not be easily assessed when the Plateau technique is used, because surface tension strongly depends on the density ratio when $\Delta\rho/\rho$ tends to zero.

3.2 Spreading of liquids on solids

Experiment 1 ES 327 deals with the spreading of a liquid drop on a plane surface. This is a highly controversial topic. See the review by Dussan (Ref. 15) and additional comments in Ref. 16.

Hocking & Rivers (Ref. 17) took up again very recently the problem of the fluid motion near an advancing contact line. To this aim they considered a geometry which is very similar to that of the above mentioned experiment.

It is well known that the classical solution of the Navier-Stokes equations with zero slip at the wall results in a force singularity at the contact line. The most simple way of circumventing this difficulty consists in assuming that not too far from the contact line there is a fluid slip at the wall which is proportional to the normal gradient of the velocity component parallel to the wall ($u=\lambda u_z$ on $z=0$), thus introducing a characteristic length, the constant of proportionality λ, which could be related to the wall roughness (Refs. 18,19).

Hocking & Rivers tackle the problem through the method of matched asymptotic expansions showing that there is an outer region, far from the contact line, whose characteristic length is the radius of the drop. There is an inner region, length order λ, enclosing the contact line, where the contact angle is the "static" contact angle, and an intermediate region which appears because terms in $\log\lambda$ from both inner and outer regions do not match.

The "dynamic" contact angle is calculated by extrapolation to the wall of the interface corresponding to the outer region, overlooking the very sharp changes of the interface slope in the inner region.

Incidentally, the outer solution results to be fairly insensitive to the value of the ill-defined λ, Figure 3, a characteristic which this model shares with similar approaches (Ref. 20).

Ngan & Dussan (Ref. 21) showed that and additional characteristic length is required to analyze the experimental results within the framework of continuum theories. They measured the apparent contact angle by use of a "two-dimensional capillary tube": two parallel slice-plates separated by spacers of different thicknesses, thus avoiding the usual criticism to results obtained with capillaries of different bore diameters, which, being manufactured under different conditions, exhibit different surface properties.

The results of Ref. 21 indicate that the ratio h/a, from which the apparent contact angle is deduced, depends on a (Figure 4). Dimensional analysis tells us that some length must be implicit in the problem in order to form with a another dimensionless group. It can be seen that, provided that Reynolds and Bond numbers effects are negligible, no length appears other than h and a, unless λ is introduced.

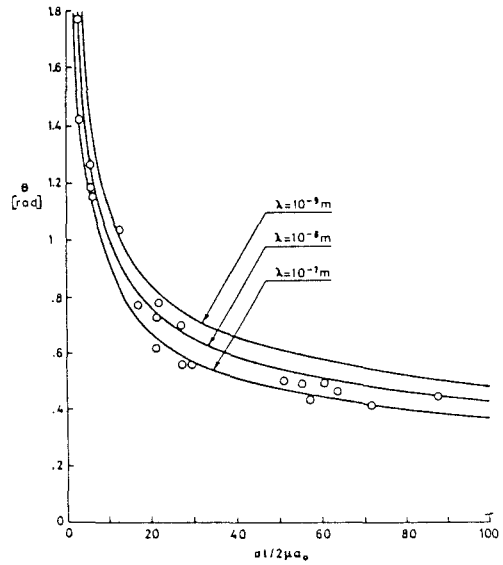

Figure 3. Dynamic contact angle, θ, vs. time, t, for drops of initial radius a_0 spreading on a plane surface. Curves have been calculated with the shown values of the slip length, λ. Experimental points are for drops of molten glasses having slightly different composition and at different ambient temperatures. From Ref. 17.

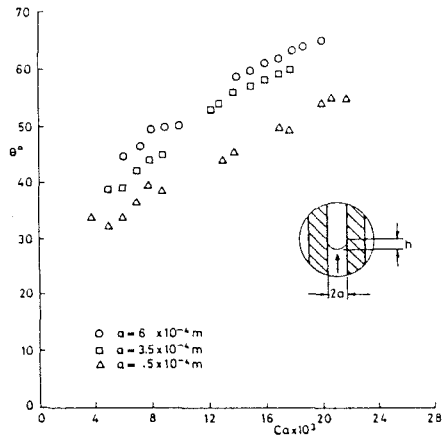

Figure 4. Dynamic contact angle, θ, vs. capillary number, $Ca=\mu V/\sigma$, for the displacement of air by silicone oil between plane parallel glass surfaces of nominal separation 2a. ○ $a=6\times10^{-4}$ m, □ $a=3.5\times10^{-4}$ m, △ $a=.5\times10^{-4}$ m. From Ref. 21.

Microgravity increases the outer characteristic length by a factor of 10 or more. We do not think that λ will increase in the same proportion because from out limited knowledge on λ we infer that it will depend on the surface texture. Nevertheless, with larger values of the drop diameter, the characteristic time will be larger, the spreading rates smaller and the capillary number quite negligible. Thus, the shape of the free surface will not depend on the velocity field, dynamical effects will be minimized and the experimental conditions more easily controlled.

Wetting phenomena in porous media present an intrinsic scientific value and technological importance. It is not surprising that experiments simulating these phenomena under reduced gravity conditions were proposed, and some of them already accomplished.

In Spacelab experiment 1 ES 339 (Fig. 2) the porous medium is simulated by three mutually contacting spheres through which exactly metered volumes of liquid are injected or sucked in order to produce advancing or receding contact lines and, if detectable, contact angle hysteresis.

In Texus III experiment the model of porous medium is a tube with axial corrugations (Ref. 22).

3.3. Marangoni convection

The relevance of reduced gravity levels becomes paramount when interfaces are present and imposed pressure gradients and velocities are absent. This is due to the increased importance of surface forces and greater extensions of interfaces in the direction of the residual gravity vector.

Even when buoyancy forces are negligible, free convection may be caused by the shear stresses acting on the interface to balance surface gradients of interface tension. The resulting flow field in the bulk of the interfacing fluids is strongly coupled via the transport (convective or diffusive) of mass, momentum and energy in both volume and surface phases.

Whereas coupling due to buoyancy forces is distributed throughout the volume and fades out with diminishing gravity levels, coupling due to surface forces is concentrated on the interface, depends strongly on its dynamics and thermodynamics (Ref. 23), and increases at low g levels because larger interfaces can be stabilized under these conditions.

Marangoni convection is induced by surface tension gradients at the interface. These gradients can be due to gradients of temperature (thermal convection), of concentration (solutal convection), or of electric potential. Here we are mainly concerned with thermal convection.

The imposed temperature gradients could have a component parallel to and/or a component normal to the undisturbed interface.

The parallel component produces the surface tractions which induce the motion in the bulk through the viscous forces. The motion immediately results whenever a temperature gradient exists, no matter how small.

The normal component of the temperature gradient transfers thermal energy to or from the surface, this would imply a work of surface tension forces and, thence, motion. But the fluid remains in a state of unstable equilibrium until a critical temperature gradient is exceeded. This threshold value decreases to zero when the surface becomes wrinkled (Ref. 24) thus indicating that both convection driven mechanisms are coupled.

As pointed out, velocity, temperature and concentration fields are influenced by convective and diffusive fluxes of mass, momentum and energy. In order to determine a priori whether the effect of the different convective and diffusive processes are dominant one must resort to appropriate dimensionless numbers. These are, for the thermal Marangoni convection in Newtonian fluids:

$$\text{Reynolds number, } Re = \frac{V_r L}{\nu}$$

$$\text{Peclet number, } Pe = RePe = \frac{V_r L}{\alpha},$$

where V_r is a reference velocity and L the length of the interface parallel to the imposed temperature gradient. ν and α are the viscous and thermal diffusivities respectively.

Diffusive fluxes in the direction normal to the main flow may be larger than those in the direction of motion and thence and additional scale factor, ℓ, is required.

When there is not imposed velocity field, the choice of the reference velocity poses some problems. An order of magnitude analysis of the equations and boundary conditions of each specific problem leads to expressing V_r as the product of a known characteristic speed, V_m, and a power, p, of the scale factor, ℓ. For thermal Marangoni flows in liquid-gas systems the characteristic velocity is the Marangoni speed of the more viscous liquid, $V_m = |\Delta\sigma|/\mu$ and p = 1 (Ref. 25).

Marangoni boundary layers occur (Refs. 25-28) when the Reynolds or Peclet numbers based on V_m are much greater than one. For giving interfacing fluids Re_m and Pe_m increase with the length L. Hence, under microgravity conditions the flow pattern may be controlled by boundary layers, contrary to what will happen on earth.

Most of the work dealing with surface driven forces is based on the so-called "liquid bridge" configuration. That is, a liquid column held by surface tension forces between two parallel discs. The overall behavior of the configuration is reasonably well understood; it has large, controllable and geometrically simple interfaces and, finally, it simulates the floating zone crystal growth technique. However, from the analytical point of view this configuration presents the drawback of the very complicated flow pattern existing near the end discs.

Up to now, the vast majority of the theoretical models disregards end effects, either assuming infinitely long columns and Stokes approximation (Refs. 29-31), Poiseuille-type flows where the axial coordinate is missing (Refs. 32,33), or fully developed boundary layers (Refs. 25-28). Very useful qualitative results have been obtained this way.

End effects have been only taken into account in restricted cases, f.e. when the Stokes approximation is valid (vanishing Re and Pe numbers), for which case very efficient mathematical tools are presently available (Refs. 34,35). Nevertheless, substantial analytical work should be devoted to this problem which may be crucial to improve many crystal growth processes.

Experiments have shown (Refs. 36,37) that the steady Marangoni convection in a liquid bridge can become oscillatory when the Marangoni number exceeds some critical value. This could results in striations in monocrystals. Although the non-steady processes are at present not fully understood, experimental evidence has been reported (Refs. 38-40) indicating that oscillatory Marangoni convection can be suppressed rotating the bridge through one or both end plates or contaminating the interface (Ref. 41).

Given the geometry of the system, fluid character-

istics and gravity level, Marangoni convection will depend on the imposed temperature gradient. Because of strict safety regulations, these temperature gradients will be small in Spacelab experiments. Thus visual observation and photographic recording of fluid motion is probably difficult.

Working with bridges as close as possible to the maximum stable length ($L=\pi D$) looks an obvious way of enhancing observable effects. But the only case in which this possibility has been analyzed (Ref. 34) indicates quite the contrary. In the Stokes limit the velocity becomes smaller the larger the ratio L/D. This conclusion seems to be strongly dependent on the low Reynolds number required to ensure the validity of the Stokes approximation.

Cylindrical bridges of annular cross-section have been suggested as a mean to enhance surface effects (Ref. 42) but, to the best of our knowledge, this idea has not been fully explored.

That Marangoni convection will increase the heat transfer between end discs is a third possibility. Nevertheless, since transparent liquids normally used in liquid bridge simulation are not much more thermally conductive than the surrounding air, a sufficiently accurate thermal balance must take into account the influence of the environment and this will require a simple and clearly defined geometry of the surroundings. It seems that no sufficient attention has been paid to this important point.

Recent European contribution to the study of surface tension driven thermal convection can be classified into three categories.

1. Experimental

   1a. Microgravity is simulated by the so-called short zone technique, where the length in the direction of gravity action is kept as small as possible (Refs. 36-41,43,44).

   1b. Sounding rocket experiments within TEXUS programme (Refs. 45-47).

Additional references will be found in these Proceedings.

2. Numerical simulation

Complete equations are solved by computer with appropriate boundary conditions in order to study the influence of the several relevant parameters. The fulfillment of the boundary conditions at the free surface, the position of which is unknown beforehand, poses serious problems (Refs. 48-50).

3. Analysis of simplified cases

   3a. Poiseuille-type flows (Refs. 32,33).

   3b. Creeping flows (Stokes approximation) (Refs. 29-31,34,35).

   3c. Fully developed boundary layer configurations (Refs. 23-28).

3.4 Mechanics of a liquid bridge

It has been said that interfaces are longer under reduced than under normal gravity conditions. This is one of the connections between the floating zone technique in crystal growth and microgravity.

In order to analyze such a complex configuration as the floating zone the first is to consider independently its several aspects. Thus, the mechanics of the liquid bridge is studied by assuming that it consists of a pure liquid with uniform properties, in thermodynamic equilibrium with the surrounding atmosphere, and held by surface tension forces between parallel coaxial supports.

Many results concerning the static stability of liquid bridges are well known (Refs. 51-54). New developments appear in these Proceedings. These results hardly can be checked experimentally unless extreme care is paid in avoiding parasitic disturbances and in the control of the liquid properties.

Dynamical problems which have been considered up to the moment were of two main types.

1. Study of the internal structure of the bridge just following a sudden disturbance such as a spin-up from rest or a small spin-up or down induced from the end supports in an already rotating bridge.

The available body of work on rotating flows in enclosures is really impressive. The rotating liquid bridge presents the new feature of the free lateral surface. Unfortunately, the internal structure of spinning-up axisymmetric cylindrical bridges only differs from its rigid-walled counterpart in thin layers near the lateral boundaries (Ref. 55). We do not think that these fine details can be detected with the presently available FPM visualization system. Thus it is advisable concentrating on those phenomena most disturbing the shape of the free surface.

2. Dynamic stability of the bridge. The time evolution of an initially cylindrical interface after a disturbance is imposed has been considered in Ref. 56. Although these studies are based on recent work with capillary jets and some results look alike, the main quantitative differences result from the fact that the supports do not exactly play the role of the nodal sections of the free jet. Thus, Figure 5, although the Rayleigh stability limit equally applies to liquid bridges and to jets the time evolution of both configurations is really different.

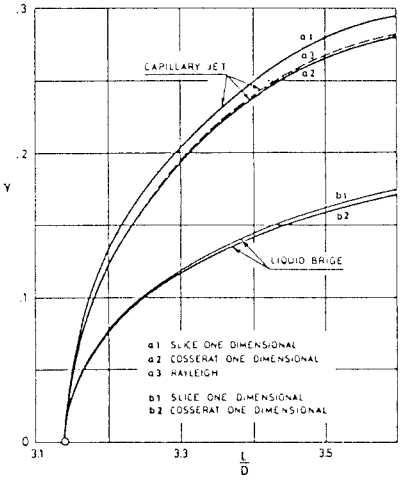

Figure 5. Unstable disturbances grow faster with jets than with liquid bridges. Figure shows the growth factor, γ, vs. dimensionless wave length (slenderness), L/D, for capillary jets (cylindrical liquid bridges) as predicted by several available methods. From Ref. 56.

Let us finish this paragraph with some comments on Plateau simulation. Plateau simulation is a simple way toward low Bond number operation. It consists in suspending a liquid inside another of precisely the same density with which it is immiscible, thus simulating zero gravity conditions for configurations at rest.

The static Bond number for a liquid column surrounded by another liquid can be written as

$$Bo = \frac{RL}{L_b^2}\frac{\delta\rho}{\rho_1} \qquad (1)$$

where R and L are the characteristic radius of curvature and the length in the direction of gravity action, respectively. $L_b = \sqrt{\sigma/\rho_1 g}$ is the so-called Bond length. ρ_1 is the density of the denser fluid and $\delta\rho$ the density difference.

A simple version of the FPM, the so-called Plateau Tank Facility (PTF) has been developed (Ref. 57). With this and similar facilities interesting results have been obtained (Refs. 9-11). Nevertheless, here are two words of caution on Plateau simulation.

1) When dynamical effects are present the static Bond number is no longer the only controlling parameter. Thus Plateau simulation of microgravity could be deceptive (Ref. 58).

2) For most couples of liquids of interest and normal gravity conditions, L_b in Eq. 1 is of the order of 10^{-3} m. In a Plateau facility where R and L are of the order of several centimeters, RL/L_b^2 could reach a value of the order of 10^3. Thus, the utmost precision is required in the control of the density of the balancing liquid. It is well known (Refs. 59, 60) that surprisingly small values of the density differences lead to results far different from those corresponding to neutral buoyancy.

4. ACHIEVING MICROGRAVITY

The body force due to earth's gravity, which in near-earth orbit is slightly less than at the earth's surface, is almost completely balanced by the force due to centripetal acceleration.

Although the achieved weightless condition is not so perfect as it could seem at first glance, the investigator must pay a large tribute in terms of experimental complexity to benefit of these low gravity levels.

Experiments performed onboard microgravity platforms are hindered with limitations regarding time, power, cooling, safety, etc. (Ref. 16).

Although the investigator should not overlook problems of this nature, the main concern here is the required vs. achieved gravity level.

The gravity environment onboard a spacecraft is not uniform. Many forces alter the nearly weightless condition (Refs. 61,62). In particular, transient disturbances (the so-called g-jitter) which can arise from spacecraft maneuvers, mechanical vibrations and crew motion, are a matter of concern. The available information indicates that in the Spacelab the oscillatory part of the g-jitter can be as great as 10^{-3} g.

Although this value can be reduced, at least while running sensitive experiments, the quoted figure is a bit disappointing for two main reasons:

1. Steps should be taken to accurately measure the acceleration vector at the correct places.
2. Analysis of the effects of g-jitter on fluids is at present in the beginnings and available information is scanty.

The stationary component which, according to most authors, is smaller is not so harmful, not to mention that, as will be discussed, our skill in accurately measuring, on earth, thermodynamic and transport properties seems to be incomparably less than that displayed in achieving microgravity levels.

Predictive analysis by the investigators is, of course, paramount. Usually this analysis follows three steps of increasing sophistication:

1. Zero-gravity step. Gravity is assumed to be literally zero. Second order effects, normally overshadowed by gravity, become apparent. The resulting configuration of the system is predicted on this basis. This step leads to overoptimistic expectancies on the usefulness of zero gravity.

2. Critical estimation step. An order of magnitude analysis, accounting for small (but not zero) gravity, and based on appropriate dimensionless parameters, provides information on the dependence of the flow regime on the data of the problem.

Such type of analysis displays the extreme richness of interdependent and previously unforeseen phenomena which could appear under microgravity conditions. For example, it can be shown (Ref. 63) that more than a dozen different configurations may appear with steady buoyancy induced, surface tension induced and coupled free convections in systems involving two interfacing fluids.

This approach also substantiates two points which were already mentioned in passing:

1. Limitations of partial simulation. Simulation of microgravity on earth would require, in principle, to exactly reproduce every non-dimensional parameter appearing in the real phenomena.

For example, to reduce the value of a parameter representing the ratio of gravity to other force, this force can be increased, but then a certain number of ratios of the other forces to the second one are also decreased and, thence, the real phenomena are not properly modelled.

2. Sometimes the requirement of a precisely fixed gravity level is unjustified (although the requirement of steadiness is not) in the face of the poor accuracy with which some physical fluid properties are known.

Let us consider an example. For thermal Marangoni convection in a liquid bridge, in a reduced gravity environment, and in the absence of dissipative layers, i.e., when viscous (and thermal) effects penetrate deeply into the fluids, a Reynolds number appears based on Marangoni speed and Bond length.

$$Re_m = \frac{\sigma_T \Delta T}{\mu\nu}\sqrt{\frac{\sigma}{\rho g}} \, . \qquad (2)$$

Equation 2 indicates that the influence of a given relative error in σ_T (which is measured fairly in-

accurately and is sensitive to contamination and aging) is twice that of the same relative error in g. The situation worsens when solutal Marangoni convection is considered or when fluid properties are strongly temperature dependent.

The third step in the predictive effort of the investigator consists in the search for analytical (and numerical) solutions for configurations under reduced gravity. In most cases gravity action is assumed to be constant and its direction such that the symmetry of the system is preserved. It is realized at this step that in many cases 10^{-4} g is not the same as zero and that effects whose observation was foreseen during the first step still remain hidden or strongly coupled to other effects.

5. CONCLUSIONS

An overview of microgravity fluid physics in Europe has been made, mainly in connection with Spacelab experiments. In the presentation of such a broad topic some choice has to be made. Thence, the authors touched upon points which are at present the subject of their interest and concern.

The need for a better fundamental understanding should be strongly emphasized. This understanding requires a very substantial work in the terrestrial laboratory which is absolutely necessary if future space experiments are to be carried out in a systematic and efficient basis.

6. REFERENCES

1. Delattre M & Dubois G 1966, Mise en place à l'ONERA d'une installation d'essais en impesanteur, *La Recherche Aérospatiale*, 110, 19-28.

2. Maulard J L & Jourdin A 1966, Expériences sur le comportement des liquides en impesanteur, *La Recherche Aérospatiale*, 110, 29-37.

3. Boulay J L 1968, La transmission de chaleur dans l'azote liquide en impesanteur, *La Recherche Aérospatiale*, 122, 35-50.

4. ESRO CR-19 1970, *Feasibility study for the development of a vaporizing liquid-fuel gauge*, by Fraga E & Muñoz Torralbo A.

5. Sanmartín J R, Fraga E & Muñoz Torralbo A 1972, Zero-g gauging systems, ELDO Contract No 17/8/4. INTA, Madrid.

6. Walter H U 1982, Scientific results and accomplishments of the TEXUS programme, *XXXIII Congress-IAF*, Paris, France, 26 Sept.-2 Oct., 1982, IAF-82-151.

7. Martínez I 1979, *Fluid Physics Module utilization brochure*, ESA.

8. Galotto C P & Rovera G 1981, The Italian Fluid Physics Module, *XXXII Congress-IAF*, Rome, Italy, Sept. 6-12, 1981, IAF-81-151.

9. Rodot H, Bisch C & Lasek A 1979, Zero gravity simulation of liquids in contact with a solid surface, *Acta Astronautica*, 6(9), 1083-1092.

10. Bisch C, Lasek A & Rodot H 1982, Comportement hydroynamique de volumes liquides sphériques semi-libres en apesanteur simuleé, *Journal de Mecánique*, 1(1), 165-183.

11. Bisch C 1982, Existence et position de cercles nodaux sur un calotte sphérique liquide oscillant en microgravité a sa frequence principale de resonance F_R, *XXXIII Congress-IAF*, Paris, France, Sept. 26-Oct. 2, 1982, IAF 82-135.

12. Lamb H 1916, *Hydrodynamics*, Cambridge University Press, 468-469.

13. Trinh E, Zwern A & Wang T G 1982, An experimental study of small amplitude drop oscillations in immiscible liquid systems, *J. Fluid Mech.*, 115, 453-474.

14. Trinh E & Wang T G 1982, Large-amplitude free and driven drop-shape oscillations: experimental observations, *J. Fluid Mech.*, 122, 315-338.

15. Dussan V E B 1979, On the spreading of liquids on solid surfaces, static and dynamic contact lines, *Annual Review of Fluid Mechanics, Vol. 11*, Annual Reviews Inc., Palo Alto, Calif., 371-400.

16. Malmejac, Y, Bewersdorff A, Da Riva I & Napolitano L G 1981, Challenges & prospectives of microgravity research in space, *ESA BR-05*, 12 and 66-69.

17. Hocking L M & Rivers A D 1982, The spreading of a drop by capillary action, *J. Fluid Mech.*, 121, 425-442.

18. Hocking L M 1977, A moving fluid interface on a rough surface, *J. Fluid Mech.*, 76, 801-817.

19. Hocking L M 1977, A moving fluid interface.Part 2. The removal of the force singularity by a slip flow, *J. Fluid Mech.*, 79, 209-229.

20. Dussan V E B 1976, The moving contact line: the slip boundary condition, *J. Fluid Mech.*, 77, 665-684.

21. Ngan C G & Dussan V E B 1982, On the nature of the dynamic contact angle: an experimental study, *J. Fluid Mech.*, 118, 27-40.

22. Sell P J, Maisch E & Siekmann J 1982, Note on fluid transport in capillary systems under microgravity, *XXXIII Congress-IAF*, Paris, France, Sept. 26-Oct. 2, 1982, IAF-82-151.

23. Napolitano L G 1979, Thermodynamics and dynamics of surface phases, *Acta Astronautica*, 6(9), 1093-1112.

24. Smith K A 1966, On convective instability induced by surface tension gradients, *J. Fluid Mech.*, 24, 401-414.

25. Napolitano L G 1979, Marangoni boundary layers, *Proc. Third European Symposium on Material Sciences in Space*, Grenoble, France, 24-27 April 1979, ESA SP-142, 349-358.

26. Napolitano LG & Golia C 1980, Similar solutions of Marangoni boundary layers, *3rd Levich Conference*, Madrid, Spain, March 30-April 2, 1980.

27. Napolitano L G & Golia C 1981, Coupled Marangoni boundary layers, *Acta Astronautica* 8(5-6), 417-434.

28. Napolitano L G & Russo G 1982, Similar axially symmetric Marangoni boundary layer, *XXXIII Congress-IAF*, Paris, France, Sept. 26-Oct. 2, 1982, IAF-82-142.

29. Bauer H F 1981, Velocity distribution due to thermal Marangoni effect in a liquid column under zero-gravity environment, *LRT-WE-9-FB-5-81*, Hochschule der Bundeswehr München.

30. Bauer H F 1982, Liquid surface oscillations in a viscous liquid column induced by temperature fluctuations, *LRT-WE-9-FB-3*, Hochschule der Bundeswehr München.

31. Bauer H F 1982, Combined thermal Marangoni convection and buoyancy in a circular liquid column in microgravity, *LRT-WE-9-FB-14*, Hochschule der Bundeswehr München.

32. Napolitano L G 1980, Plane Marangoni-Poiseuille flow of two immiscible fluids, *Acta Astronautica*, 7(4), 461- 478.

33. Napolitano L G 1980, Temperature field in Marangoni-Poiseuille plane flows, *XXXI Congress-IAF*, Tokyo, Japan, Sept. 21-28, 1980, IAF-80-C-110.

34. Da Riva I & Alvarez Pereira E 1982, A regular perturbation approach to surface tension driven flows, *Acta Astronautica*, 9(4), 217-224.

35. Napolitano L G & Golia C 1982, Effects of gravity levels on Marangoni-Stokes flow in Plateau configurations, *XXXIII Congress-IAF*, Paris, France, Sept. 26-Oct. 2, 1982, IAF-82-148.

36. Chun Ch H & Wuest W 1979, Experiments on the transition from the steady to the oscillatory Marangoni convection in a floating zone under reduced gravity effect, *Acta Astronautica*, 6(9), 1073-1082.

37. Schwabe D, Scharmann A & Preisser F 1979, Steady and oscillatory Marangoni convection in floating zones under 1-g, *Proc. Third European Symposium on Material Sciences in Space*, Grenoble, France, 24-27 April 1979, ESA SP-142, 327-333.

38. Chun Ch H 1980, Marangoni convection in a floating zone under reduced gravity, *J. Crystal Growth*, 48, 600-610.

39. Wuest W & Chun Ch H 1980, Oscillatory Marangoni convection, *XXXI Congress-IAF*, Tokyo, Japan, Sept. 21-28, 1980, IAF-80-C-113.

40. Chun Ch H & Wuest W 1982, Suppresion of temperature oscillations of thermal Marangoni convection in a floating zone by superimposing of rotating flows, *Acta Astronautica*, 9(4), 225-230.

41. Schwabe D, Sharmann A & Preisser F 1982, Studies of Marangoni convection in floating zones, *Acta Astronautica*, 9(3), 183-186.

42. Napolitano L G, Prospects for space materials sciences experiments, *21° Convegno Internazionale Scientifico Sullo Spazio*, Rome, Italy, March 25-26, 1981.

43. Chun Ch H & Wuest W 1978, A micro-gravity simulation of the Marangoni convection, *Acta Astronautica*, 5(9), 681-686.

44. Monti R & Napolitano L G 1980, Experimental validation of kinematic and thermal scaling laws in Marangoni flows, *XXXI Congress-IAF*, Tokyo, Japan, Sept. 21-28, 1980, IAF-80-C-138.

45. Schwabe D, Preisser F & Scharmann A 1982, Verification of the oscillatory state of thermocapillary convection in a floating zone under low gravity, *Acta Astronautica*, 9(4), 265-273.

46. Schwabe D & Scharmann A 1982, Measurement of the critical Marangoni number in a floating zone under reduced gravity, *XXXIII Congress-IAF*, Paris, France, Sept. 26-Oct. 2, 1982, IAF-82-154.

47. Chun Ch H 1982, Numerical study on the thermal Marangoni convection and comparison with experimental results from the Texus-rocket program, *XXXIII Congress-IAF*, Paris, France, Sept. 26-Oct. 2, 1982, IAF-82-155.

48. Piva R & Strani M 1980, Numerical solutions for surface tension driven flows, *XXXI Congress-IAF*, Tokyo, Japan, Sept. 21-28, 1980, IAF-80-C-112.

49. Graziani G, Strani M & Piva R 1982, Effect of the free surface radiation in axisymmetric thermocapillary flows, *Acta Astronautica*, 9(4), 231-243.

50. Graziani G, Strani M & Piva R 1982, Local boundary layers in Marangoni convection, *XXXIII Congress-IAF*, Paris, France, Sept. 26-Oct. 2, 1982, IAF-81-140.

51. Strutt J J (Baron Rayleigh) 1945, *The Theory of Sound*, Vol. II, Dover, New York, 351-355.

52. Erle M A, Guillette R D & Dyson D C 1970, Stability of interfaces of revolution with constant surface tension. The case of the Catenoid, *Chem. Eng. J.*, 1, 97-109.

53. Gillis J 1961, Stability of a column of rotating viscous liquid, *Proc. Camb. Phil. Soc.*, 57, 152-159.

54. Martínez Herranz I 1978, Floating zone-equilibrium shapes and stability criteria, *Cospar: Space Research Vol. XVIII*, Pergamon Press, Oxford, 519-522.

55. Da Riva I & Manzano D R 1981, Impulsive motions of the floating zone, *PCH PhysicoChemical Hydrodynamics*, 2(2-3), 165-176.

56. Meseguer J 1983, On the breaking of axisymmetric slender liquid bridges, *J. Fluid Mech.*, 130, 123-151.

57. Martínez I & Rivas D 1982, Plateau tank facility for simulation of Spacelab experiments, *Acta Astronautica* 9(5), 339-342.

58. Da Riva I 1981, Stability of liquid bridges, *Applications of Space Developments*, L.G. Napolitano Ed., Pergamon Press, Oxford, 69-80.

59. Sanz A & Martínez I 1983, Minimum volume for a liquid bridge between equal discs, *J. Colloid Interface Sci.*, will appear.

60. Olbricht W L & Leal L G 1982, The creeping motion of liquid drops through a circular tube of comparable diameter: the effect of density differences between the fluids, *J. Fluid. Mech.*, 115, 187-216.

61. Knabe W & Eilers D 1982, Low-gravity environment in Spacelab, *Acta Astronautica*, 9(4), 187-198.

62. Kamotani Y, Prasad A & Ostrach S 1981, Thermal convection in an enclosure due to vibrations aboard spacecraft, *AIAA Journal*, 19(4), 511-516.

63. Napolitano L G 1982, Surface and buoyancy driven free convection, *Acta Astronautica*, 9(4), 199-215.

ALMOST CYLINDRICAL ISOROTATING LIQUID BRIDGES FOR SMALL BOND NUMBERS

J.M. Vega & J.M. Perales

ETSI, Aeronáuticos, Universidad Politécnica de Madrid, Spain

ABSTRACT

In the absence of gravity, a cylindrical-shaped liquid bridge becomes unstable as the slenderness of the bridge Λ exceeds a critical value Λ_c, which depends on the rotational Weber number W. The unstable mode is either axisymmetric (amphora-mode) or non-axisymmetric (C-mode) depending on whether W is smaller or bigger than 1/3.

Almost cylindrical bifurcating stationary shapes, with a cylindrical volume, are calculated for $|\Lambda-\Lambda_c|<<1$. It is seen that the bifurcation is always subcritical, i.e., the bifurcating non-cylindrical shapes appear for $\Lambda < \Lambda_c$.

The effect of a small axial gravity, i.e., a small gravitational Bond number B is also considered. It is seen that $\Lambda_c(0,\Lambda) - \Lambda_c(B,\Lambda)$ is of the order of $B^{2/3}$ for amphora modes, and of the order of B^2 for C-modes.

Finally, a comparison is made with numerical and experimental results available in the Literature, and some comments on the dynamical behaviour of the liquid bridge are given.

Keywords: Floating zone, Liquid bridge, Microgravity, Interfaces, Bifurcation.

1. INTRODUCTION

It is well known (Refs. 1-4) that, in the absence of gravity, a cylindrical-shaped rotating liquid bridge, bounded by two coaxial end discs (see Figure 1), becomes unstable if the slenderness of the bridge Λ (Λ = L/2R where L is the distance between the discs and R is their radius) satisfies

$$\Lambda > \Lambda_c \equiv \begin{cases} \pi/\sqrt{1+W} & \text{if} \quad W\leq 1/3 \\ \pi/\sqrt{4W} & \text{if} \quad W\geq 1/3 \end{cases}$$

i.e., if the point (Λ,W) is above the curve ABC in Figure 2. The Weber number W is defined as $W = \rho\Omega^2R^3/\sigma$, where ρ is the density of the liquid, σ is its surface tension coefficient and Ω is the angular velocity.

Local bifurcation Theory will be used, in sections 2-3, to obtain an axymptotic description, as $\Lambda \to \Lambda_c$, of the bifurcating noncylindrical shapes. For numerical computations see Ref. 5, where an asymptotic analysis, as $\Lambda \to \Lambda_c$, of the (axisymmetric) case $W \leq 1/3$ may also be found.

The effect of a small axial gravity g, which is measured by the gravitational Bond number $B = \rho gR^2/\sigma$, will be considered in section 4. A typical value of $\sigma/\rho R^2$ is 5 cm/sc^2 (R = 4 cm, water); therefore, the gravitational effect should not be ignored even for extremely small values of g (say, $5\cdot10^{-4}$ times its value at the surface of the Earth).

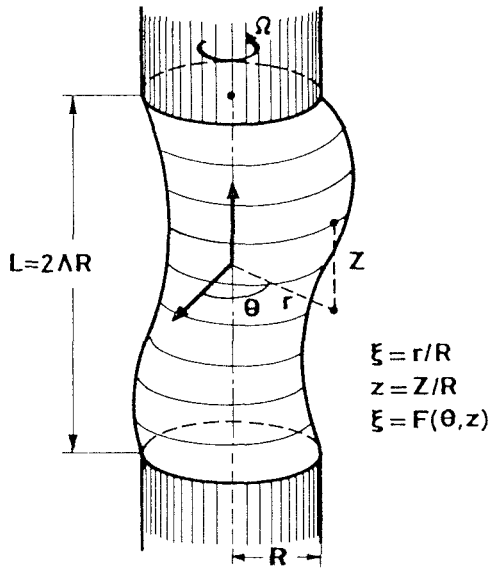

Figure 1. Sketch of the liquid bridge.

1.1 Equilibrium equation

The equation governing the steady shape of the liquid bridge is obtained by expressing the equilibrium between surface tension and local pressure forces at the free surface of the liquid. After suitable non-dimensionalization, it may be written as

$$M(F) + p + \frac{1}{2} WF^2 - Bz = 0 \qquad (1)$$

Proceedings of the 4th European Symposium on Materials Sciences under Microgravity, *Madrid, Spain*, 5-8 *April* 1983 (*ESA SP*-191 – *June* 1983).

where $\xi = F(\theta,z)$ is the equation of the free surface in cylindrical coordinates (see Figure 1), p is the (nondimensional) pressure at $\xi = z = 0$, and the local mean curvature M(F) is (Ref. 6),

$$M(F) = \frac{F(1+F_z^2)(F_{\theta\theta}-F)+FF_{zz}(F^2+F_\theta^2)-2F_\theta(F_\theta+FF_zF_{\theta z})}{[F^2(1+F_z^2)+F_\theta^2]^{3/2}} \quad (2)$$

Equation 1 is to be integrated with the boundary conditions

$$F(\theta,\pm\Lambda) = 1 \ , \ F(\theta+2\pi,z) \equiv F(\theta,z) \quad (3)$$

(liquid bridge anchored to the edges of the end discs, azimuthal periodicity), and the condition of conservation of the volume of the bridge,

$$\left| \int_{-\Lambda}^{\Lambda} dz \int_0^{2\pi} F^2 d\theta \right| = 4\pi\Lambda \quad (4)$$

1.2 Linear stability in the absence of gravity (B=0)

Let us look for solution of Eqs. 1-4 of the form

$$F = F_e + \varepsilon\bar{F} + o(\varepsilon) \ , \quad p = p_e + \varepsilon\bar{p} + o(\varepsilon)$$

where $F_e \equiv 1$, $p_e = 1 - W/2$ (cylindrical liquid bridge) and $\varepsilon << 1$. $\bar{F}$ and $\bar{p}$ are seen to be given by the linear problem

$$\bar{F}_{zz} + \bar{F}_{\theta\theta} + (1+W)\bar{F} + \bar{p} = 0 \quad (5)$$

$$\bar{F}(\theta,\pm\Lambda)=0 \ , \ \bar{F}(\theta+2\pi,z)\equiv\bar{F}(\theta,z) \ , \ \int_{-\Lambda}^{\Lambda} dz \int_0^{2\pi} \bar{F} d\theta = 0 \quad (6)$$

which has the nontrivial solutions:

Axisymmetric:

- If $\Lambda\sqrt{1+W} = j\pi$ $(j = 1,2,\ldots)$,

  $\bar{F}(\theta,z) = \sin(\sqrt{1+W}z)$, $\bar{p} = 0$.

- If $\Lambda\sqrt{1+W} = \lambda_k$ $(\tan\lambda_k = \lambda_k$, $k = 1,2,\ldots)$

  $$\bar{F}(\theta,z) = \frac{\bar{p}}{\sqrt{1+W}}\left[1 - \frac{\cos(\sqrt{1+W}z)}{\cos(\sqrt{1+W}\Lambda)}\right]$$

Non-axisymmetric:

- If $\Lambda\sqrt{1+W-n^2} = m\pi/2$ $(n,m = 1,2,\ldots)$

  $\bar{F}(\theta,z) = \cos n\theta \sin(\sqrt{1+W-n^2}z + m\pi/2)$, $\bar{p} = 0$

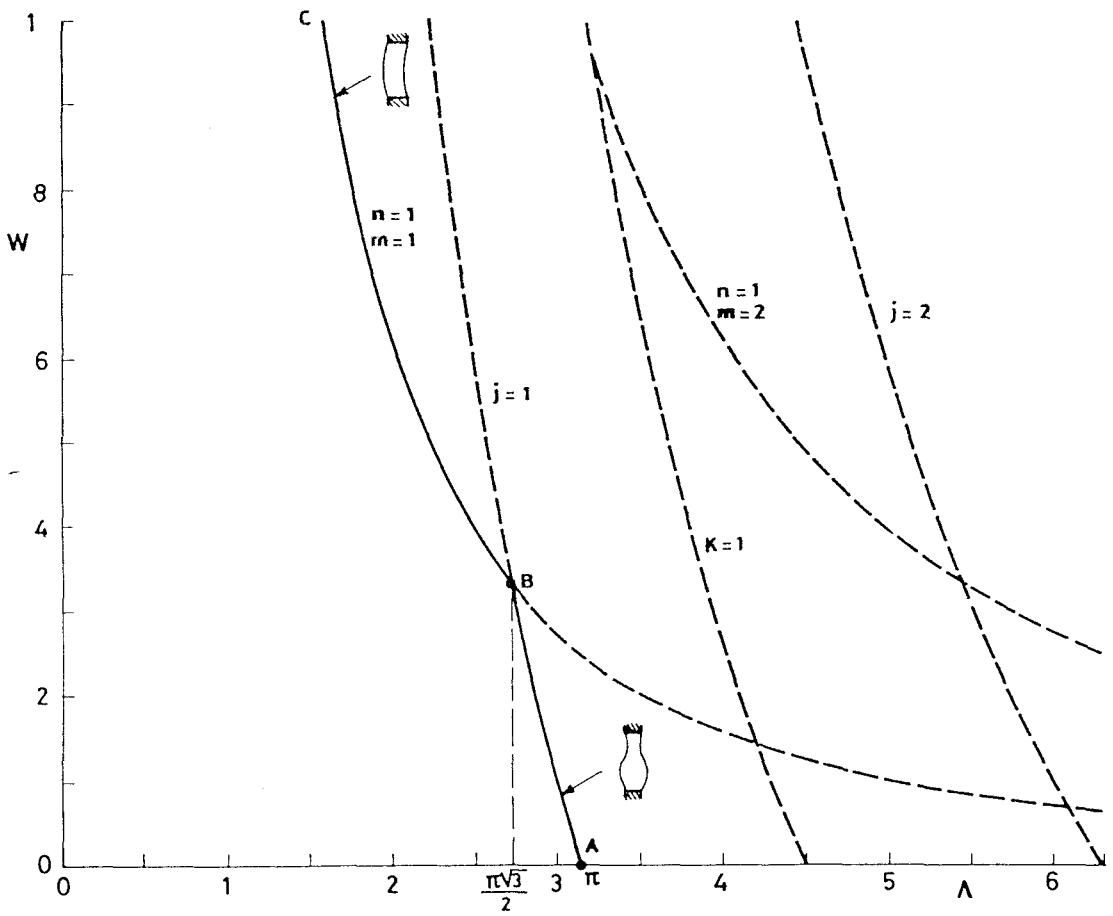

Figure 2. Stability diagram (no gravity).

Bifurcation (from cylinders) to noncylindrical equilibrium shapes appears only (Implicit Function Theorem, Ref. 7) near the curves $\Lambda\sqrt{1+W} = k\pi$, $\Lambda\sqrt{1+W} = \lambda_k$, $\Lambda\sqrt{1+W-n^2} = k\pi/2$, which are plotted in Figure 2. Nevertheless, only the bifurcations from the curves AB ($\Lambda\sqrt{1+W} = \pi$) and BC ($\Lambda\sqrt{W} = \pi/2$) are significant in practice (the curve ABC represents the transition from stable to unstable cylinders).

2. BIFURCATION TO EQUILIBRIUM SHAPES

Let $W = W_o(\Lambda)$ be the equation of any of the curves AB or BC, and $\bar{F}$ be a nontrivial solution of Eqs. 5-6 for $W = W_o(\Lambda)$. For a fixed value of Λ, the variables u and q, and the parameters ε and b are introduced as

$$W=W_o+b \ , \ p=1-\frac{1}{2}W_o-\frac{1}{2}b+q \ , \ \bar{F}=1+\varepsilon\bar{F}(\theta,z)+u(\theta,z)$$

Eqs. 1-4 may be written in the form

$$M(1+\varepsilon\bar{F}+u)+1+q+(W_o+b)(2+\varepsilon\bar{F}+u)(\varepsilon\bar{F}+u)/2-Bz = 0 \qquad (7)$$

$$u(\theta,\pm\Lambda)=0 \ , \ u(\theta+2\pi,z)\equiv u(\theta,z) \ , \ <\varepsilon\bar{F}+u,2+\varepsilon\bar{F}+u> = 0 \qquad (8)$$

$$< \bar{F},u > = 0 \qquad (9)$$

in terms of the inner product

$$< f,g > = \int_{-\Lambda}^{\Lambda} dz \int_0^{2\pi} fg\,d\theta$$

Observe that condition (9) defines the parameter ε as

$$\varepsilon = < F,\bar{F} >/< \bar{F},\bar{F} >$$

The problem 7-9 provides ε, $u(\theta,z)$ and q in terms of b and B. As B,b → 0, such functions may be calculated by means of standard Perturbation Techniques (Refs. 8-9). However, a direct use of such techniques, (a) requires to anticipate certain properties of the solution and (b) leads to a singular perturbation problem in the case $B \neq 0$ (Ref. 9). Both difficulties are avoided by using the idea of bifurcation equation. We consider the auxiliary equation

$$M(1+\varepsilon\bar{F}+u)+1+q+(W_o+b)(2+\varepsilon\bar{F}+u)(\varepsilon\bar{F}+u)/2-Bz+\psi\bar{F}=0 \qquad (10)$$

which is identical with Eq. 7 if $\psi = 0$. It may be shown that Eqs. 8-10 uniquely define

$$\psi = \psi(\varepsilon,b,B)$$

$$u = u(\theta,z;\varepsilon,b,B) \quad , \quad q = q(\varepsilon,b,B) \qquad (11)$$

at least as $\varepsilon,b,B \to 0$ (Implicit Function Theorem). Such functions correspond to solutions of Eqs. 7-9 if and only if ε,b and B satisfy

$$\psi(\varepsilon,b,B) = 0 \qquad (12)$$

which is known as the bifurcation equation of the problem. If ε, b and B satisfy the bifurcation equation the functions 11 are solutions of Eqs. 7-9.

3. BIFURCATION EQUATION IN THE ABSENCE OF GRAVITY (B=0)

The Bond number, B, will vanish throughout this section. If, in addition, $\varepsilon = 0$, Eqs. 8-10 have the solution $\psi = q = 0$, $u \equiv 0$; since the solution of Eqs. 8-10 is unique,

$$\psi(0,b,0) = 0 \ , \ u(\theta,z;0,b,0) \equiv 0 \ , \ q(0,b,0) = 0$$

and

$$\psi(\varepsilon,b,0) = \varepsilon g(\varepsilon,b)$$

$$u(\theta,z;\varepsilon,b,0) = \varepsilon v(\theta,z;\varepsilon,b) \ , \ q(\varepsilon,b,0) = \varepsilon r(\varepsilon,b)$$

where g, v and r are C^∞ functions of ε and b; their Taylor series expansions at b = B = 0 yield

$$\psi(\varepsilon,b,0) = \varepsilon\sum g_{ij}\varepsilon^i b^j \ , \ u(\theta,z;\varepsilon,b,0) = \varepsilon\sum v_{ij}(\theta,z)\varepsilon^i b^j \ ,$$

$$q(\varepsilon,b,0) = \varepsilon\sum r_{ij}\varepsilon^i b^j \qquad (13)$$

When the expansions (13) are inserted into the equations 8-10, and the coefficient of each power $\varepsilon^i b^j$ is set to zero, a recursive sequence of linear problems results, to calculate g_{ij}, v_{ij} and r_{ij}.

3.1 Axisymmetric case (Curve AB of Figure 2)

In this case

$$W_o(\Lambda) = (\pi/\Lambda)^2 - 1 \quad , \quad \bar{F} = \sin(\pi z/\Lambda)$$

Then

$$g_{00} = 0 \quad , \ v_{00} \equiv 0 \quad , \quad r_{00} = 0 \quad ; \quad g_{01} = -1$$

$$g_{10} = 0 \quad , \quad r_{10} = \frac{2-W_o}{4} \ ,$$

$$v_{10} = -\frac{W_o}{4(1+W_o)}\cos\frac{\pi z}{\Lambda} - \frac{1}{4} + \frac{1}{4(1+W_o)}\cos\frac{2\pi z}{\Lambda}$$

and

$$g_{20} = -\frac{3(1+W_o+W_o^2/2+W_o^3/4)}{2(1+W_o)} \qquad (14)$$

Then, the bifurcation equation 12 yields

$$b \equiv W - W_o(\Lambda) = g_{20}\varepsilon^2 + o(\varepsilon^2) \qquad (15)$$

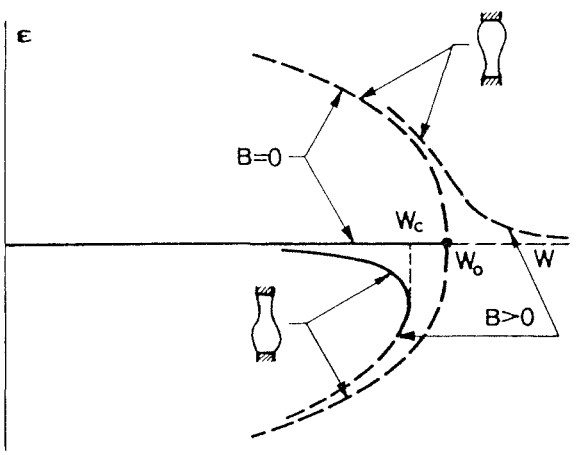

Figure 3. Axisymmetric bifurcation.

When b and satisfy Eq. 15

$$F(\theta,z) = 1+\varepsilon\sin(\pi z/\Lambda)+\varepsilon^2 v_{10}(z)+o(\varepsilon^2)$$

$$p = 1 - W_o/2 + \varepsilon^2 r_{10} + o(\varepsilon^2)$$

is a solution of Eqs. 1-4. Eq. 15 has been plotted in Figure 3, and g_{20} in terms of Λ, in Figure 4. Observe that the bifurcation is subcritical; then, the bifurcated solutions are expected to be unstable.

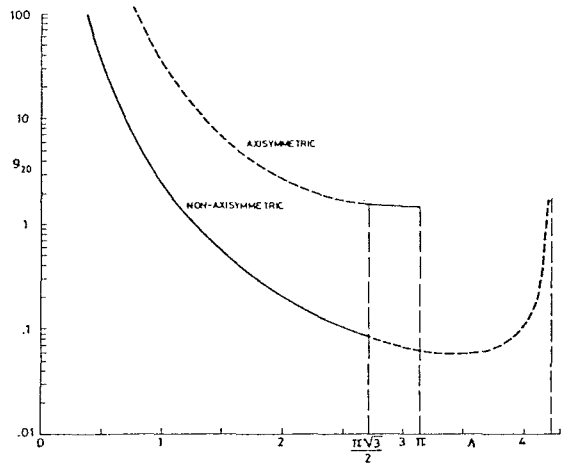

Figure 4. g_{20} vs. Λ for axisymmetric (upper curve) and non-axisymmetric (lower curve) bifurcation.

3.2 Non-axisymmetric case (Curve BC of Figure 2)

In this case

$$W_o(\Lambda) = (\pi/2\Lambda)^2 \ , \ \bar{F} = \cos\theta\cos(\pi z/2\Lambda) \qquad (16)$$

Then

$$g_{00} = 0 \ , \ v_{00} \equiv 0 \ , \ r_{00} = 0 \ ; \ g_{01} = -1 \ , \ g_{10} = 0$$

$$r_{10} = -\frac{1+2W_o}{8} + \frac{1+W_o}{8(3W_o-1)} \frac{(3W_o-1)\sqrt{1+W_o}\Lambda + \tan(\sqrt{1+W_o}\Lambda)}{\sqrt{1+W_o}\Lambda - \tan(\sqrt{1+W_o}\Lambda)}$$

$$v_{10} = -\frac{1+2W_o+8r_{10}}{8(1+W_o)}\left[1 - \frac{\cos(\sqrt{1+W_o}z)}{\cos(\sqrt{1+W_o}\Lambda)}\right] +$$

$$+ \frac{1}{8(3W_o-1)}\left[\cos\frac{\pi z}{\Lambda} + \frac{\cos(\sqrt{1+W_o}z)}{\cos(\sqrt{1+W_o}\Lambda)}\right] +$$

$$+ \frac{3+2W_o}{8(3-W_o)}\left[1 - \frac{\cos(\sqrt{W_o-3}z)}{\cos(\sqrt{W_o-3}\Lambda)}\right]\cos 2\theta +$$

$$+ \left[\cos\frac{\pi z}{\Lambda} + \frac{\cos(\sqrt{W_o-3}z)}{\cos(\sqrt{W_o-3}\Lambda)}\right]\frac{\cos 2\theta}{8(1+W_o)}$$

and

$$g_{20} = \frac{18-7W_o-9W_o^2}{32} - \frac{(2+W_o)(9+4W_o)}{32(1+W_o)} +$$

$$+ \frac{9W_o(1+W_o)}{8(3W_o-1)}\left[\frac{(1+2W_o)^2}{2} - \frac{W_o\sqrt{1+W_o}\Lambda}{\sqrt{1+W_o}\Lambda - \tan(\sqrt{1+W_o}\Lambda)}\right] -$$

$$- \frac{W_o(3+W_o)}{4(1+W_o)(3-W_o)}\left[\frac{3+2W_o}{2} - \frac{W_o(3+W_o)}{1+W_o}\frac{\tan(\sqrt{W_o-3}\Lambda)}{\sqrt{W_o-3}\Lambda}\right] \qquad (17)$$

The bifurcation equation 12 leads to

$$b \equiv W - W_o(\Lambda) = g_{20}\varepsilon^2 + o(\varepsilon^2) \qquad (18)$$

If b and ε satisfy Eq. 18

$$F(\theta,z) = 1 + \varepsilon\cos\theta\cos(\pi z/2\Lambda) + \varepsilon^2 v_{10} + \ldots$$

$$p = 1 - W_o/2 + \varepsilon^2 r_{10} + \ldots$$

is a solution of Eqs. 1-4. Again, Eq. 18 is plotted in Figure 5, and g_{20} vs. Λ, in Figure 4.

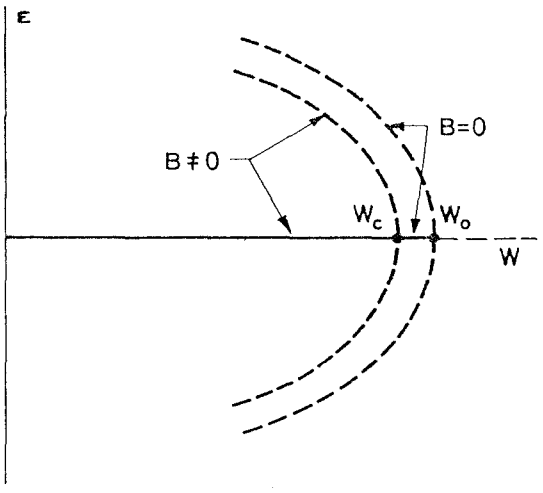

Figure 5. Non-axysimmetric bifurcation.

The area of a section z = const. of the liquid bridge is

$$A(z) = \frac{1}{2}\int_0^{2\pi} F^2 d\theta = \frac{\pi\varepsilon^2}{2}\left[-\frac{W_o+8r_{10}}{1+W_o} + \frac{3W_o}{3W_o-1}\cos\frac{\pi z}{\Lambda} + \right.$$

$$\left. + \frac{1+W_o+(3W_o-1)(1+2W_o+8r_{10})}{(1+W_o)(3W_o-1)}\frac{\cos(\sqrt{1+W_o}z)}{\cos(\sqrt{1+W_o}\Lambda)}\right] + \ldots$$

A(z) is seen to have a maximum at z = 0, and two minima, at $z = \pm|z_{min}|$. At first approximation of A_{max}, A_{min} and $|z_{min}|$ are given in Figure 6.

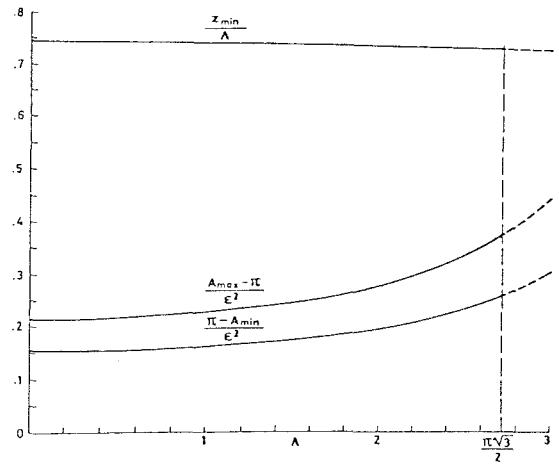

Figure 6. A_{max}, A_{min}, $|z_{min}|$ vs. Λ for non-axisymmetric bifurcated liquid bridges.

4. EFFECT OF A RESIDUAL GRAVITY

4.1 Axisymmetric case

As $\varepsilon,b,B \to 0$

$$\psi(\varepsilon,b,B) = \psi(\varepsilon,b,0) + \psi_1 B + \ldots \qquad (19)$$

$$u(z;\varepsilon,b,B) = u(z;\varepsilon,b,0) + u_1(z)B + \ldots \qquad (20)$$

$$q(\varepsilon,b,B) = q(\varepsilon,b,0) + q_1 B + \ldots \qquad (21)$$

where $\psi(\varepsilon,b,0)$, $u(z;\varepsilon,b,0)$ and $q(\varepsilon,b,0)$ has been calculated in section 3. ψ_1, u_1 and q_1 are calculated from the linear problem obtained by inserting Eqs. 19-21 into Eqs. 8-10, and setting to zero the coefficient of B,

$$\psi_1 = \frac{2}{\sqrt{1+W_o}} \quad , \quad q_1 = 0 \quad , \quad u_1 = z[1+\cos(\sqrt{1+W_o}\,z)]/\sqrt{1+W_o}$$

The resulting bifurcation equation is

$$\varepsilon(-b + g_{20}\varepsilon^2 + \ldots) + 2B/\sqrt{1+W_o} + \ldots = 0 \qquad (22)$$

For B = constant, the curves ε-b given by Eq. 22 are as those plotted in Figure 3. In particular, the new stability limit is found to be

$$b_c \equiv W_c - W_o(\Lambda) = 3[g_{20}B^2/(1+W_o)]^{1/3} + \ldots$$

4.2 Non-axisymmetric case

The equations 8-10 (W_o and $\bar{F}$ as given by Eq. 16) are invariant under the symmetries

$$\theta \to \theta + \pi \quad , \quad \varepsilon \to -\varepsilon \quad , \quad \psi \to -\psi$$

and

$$z \to -z \quad , \quad B \to -B$$

Since the solution of Eqs. 8-10 is unique, these symmetries lead to

$$\psi(-\varepsilon,b,B) \equiv -\psi(\varepsilon,b,B) \quad , \quad \psi(\varepsilon,b,-B) \equiv \psi(\varepsilon,b,B)$$

As a consequence, ψ is an even function of B, and it is an odd function of ε; therefore, it may be written in the form $\psi(\varepsilon,b,B) = \varepsilon\phi(\varepsilon^2,b,B^2)$, where ϕ is a C^∞ function of ε^2, b and B^2, and the bifurcation equation is

$$\varepsilon(-b + g_{20}\varepsilon^2 + a_1 B^2 + \ldots) = 0$$

It provides a relation between ε and b (for a fixed value of B) as that sketched in Figure 5. The stability limit is

$$b_c \equiv W_c - W_o(\Lambda) = a_1 B^2 + \ldots$$

a_1, which is expected to be negative, could be calculated from a (too ugly to deal with) system of recursive linear problems.

5. RESULTS AND CONCLUSIONS

The analysis of sections 2-4 was made for a fixed value of Λ. Bifurcation equations, for a fixed Weber number W, are now easily obtained.

- Axisymmetric case

The bifurcation equation is

$$\varepsilon[-2(1+W)l + g_{20}\varepsilon^2 + \ldots] + 2B/\sqrt{1+W} + \ldots = 0$$

where

$$\Lambda = \Lambda_o(W)(1+l) \quad , \quad \Lambda_o(W) = \pi/\sqrt{1+W}$$

and g_{20} is obtained by a substitution of W_o by W in Eq. 14. The stability limit is

$$l_c \equiv \frac{\Lambda_c - \Lambda_o(W)}{\Lambda_o(W)} = \frac{3}{4}[g_{20}B^2/(1+W)^4]^{1/3} + \ldots$$

For W = 0 (no rotation), $g_{20} = -3/2$, $\Lambda_o = \pi$ and

$$\Lambda_c = \pi[1 - \frac{3}{2}(\frac{3}{2}B^2)^{1/3} + \ldots] \qquad (23)$$

The estimate $\Lambda_c = \pi/\sqrt{1+B}$, which was obtained in Ref. 10, has been used sometimes in the Literature. Observe that it is not asymptotically correct, as $B \to 0$. A comparison of the approximation of Eq. 23 with numerical and experimental values (taken from Ref. 11) is given in Figure 7.

- Non-axisymmetric case

The bifurcation equation is

$$\varepsilon[-2Wl + g_{20}\varepsilon^2 + a_1 B^2 + \ldots] = 0$$

where

$$\Lambda = \Lambda_o(W)(1+l) \quad , \quad \Lambda_o(W) = \pi/\sqrt{4W}$$

and g_{20} is obtained by substitution of W_o by W in Eq. 17.

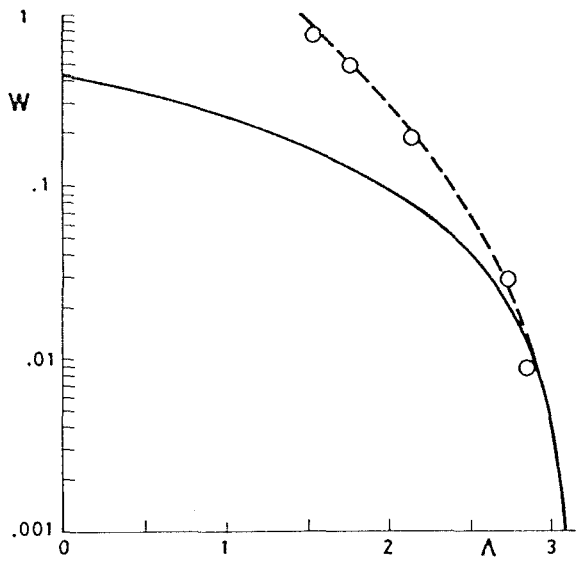

Figure 7. The stability limit vs. the Bond number for W = 0: (---) numerical, (——) as given by Eq. 23, and (o) experimental.

Some comments about the results obtained above are in order:

- In the segment AB of Figure 2, $W \leq 1/3$ and $g_{20} \simeq -3/2$ (see Figure 4). Therefore, the stability limit is

$$\Lambda_c \simeq \frac{\pi}{\sqrt{1+W}} \{1 - \frac{3}{2} [\frac{3B^2}{2(1+W)^4}]^{1/3} + \ldots\}$$

- In part of the segment BC, $|g_{20}|$ is quite small (see Figure 4). Therefore, the size of the perturbations leading to breakage of the bridge is expected to be large in the non-axisymmetric case, as compared with that of the axisymmetric case.

- In a dynamic analysis of the liquid bridge, the mode $F-1 = \varepsilon\bar{F}$, which loses stability as (Λ,W) passes through the curve ABC in Figure 2, is expected to be decoupled, in first approximation, from the remaining oscillating modes. Then, at least in a first stage of a purely non-axisymmetric breakage process, the liquid bridge is expected to be as the bifurcated shapes which were obtained in 3.2, with a central paunch and two symmetric necks.

- The curve AB is much more sensitive than the curve BC to a residual gravitational effect.

REFERENCES

1. Gillis J 1961, Stability of a column of rotating viscous liquid, *Proc. Camb. Phil. Soc.*, 57, 152-159.

2. Hardy S & Corriel S R 1974, Melt shape in weightless crystal growth, *NBS Space Processing Research*, NBSIR 74-611, US Department of Comerce.

3. Fowle A A et al. 1976, *Float-zone processing in a weightless environment*, NASA CR-2768.

4. Martínez I 1978, *Hidrostática de la zona flotante*, Tesis Doctoral, Universidad Politécnica de Madrid.

5. Brown R A & Scriven L E 1980, The shapes and stability of captive rotating drops, *Phil. Trans. R. Soc.* London, 297, 51-79.

6. Struik D J 1957, *Classical Differential Geometry*, Addison Wesley.

7. Lang S 1969, *Real Analysis*, Addison Wesley.

8. Millman M H & Keller J B 1969, Perturbation theory of nonlinear boundary-value problems, *J. Math. Phys.*, 10, 342-361.

9. Matkowsky B J & Reiss E L 1977, Singular perturbations of bifurcations, *SIAM J. Appl. Math.* 33(2), 230-255.

10. Carruthers J R & Grasso M 1972, Studies of Flotating liquid zones in simulated zero gravity, *J. Appl. Phys.* 43(2), 436-445.

11. Corriel et al. 1977, Stability of liquid zones, *J. Colloid Interface*, 60, 126-136.

CONSERVATION LAWS FOR LIQUID BRIDGES

I. Da-Riva

Laboratorio de Aerodinámica, Universidad Politécnica, Madrid, Spain

ABSTRACT

Conservation laws for an inviscid liquid bridge set into motion by conservative forces are given in integral form. These laws provide useful information on the overall motion of the bridge in the presence of unexpected or uncontrolled disturbances and could, in addition, be monitored in a computational solution of the problem as an accuracy check.
Many of the resulting conservation laws are familiar to fluiddynamicists. Nevertheless, a systematic approach providing an exhaustive list of these laws reveals the existence of new conserved properties hardly deducible in the classical way. Although the present analysis concerns the case of axial, and constant, gravity it can be applied, with minor refinements, when the gravity field varies with time in both direction and intensity.

Keywords: Microgravity, Liquid bridge, Water waves, Symmetry groups, Conserved densities, Conservation laws.

1. INTRODUCTION

The idea of looking for groups of continuous transformations with respect to which the equations of some physical phenomena are invariant was developed by Birkhoff (Ref. 1). The mathematical algorithm for seeking the broad group of these transformations (symmetry groups) for ordinary differential equations is due to Lie, see the historical account in the preface to Ref. 2. In recent times a series of results of general character and applications to particular problems of mechanics and physics have been given by Ovsiannikov (Ref. 3), Bluman and Cole (Ref. 2), and Benjamin and Olver (Ref. 4). In particular, the problem of water waves in an otherwise undisturbed ocean is considered in the last reference.

Conservation laws written in integral form are linked to every one-parameter group of symmetries according to a theorem due to Noether which can be applied to variational problems associated to Euler-Lagrange systems (Ref. 3). For the present purposes a version of this theorem for Hamiltonian systems (Ref. 5) looks more adventageous.

2. THE LIQUID BRIDGE

The bridge is a liquid column, more or less cylindrical, held by surface tension forces between two solid supports not too far apart from each other.

The liquid is assumed to be inviscid, and set into motion from rest by conservative forces. The length of the bridge is larger than the characteristic axial length of the surface wave under consideration or the axial distance travelled by the wave during the observation time.

Gravity action either axial or non-axial, steady or non-steady can be taken into account.

2.1 The hydrodynamic problem

The hydrodynamic problem is defined as follows. See Figure 1 for the nomenclature and coordinate frame.

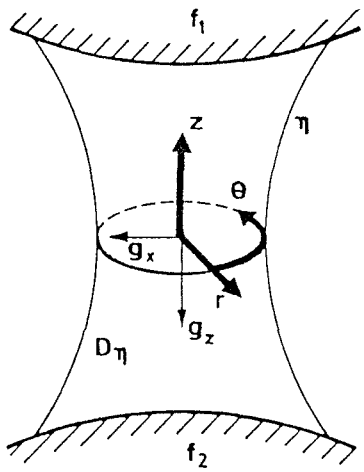

Figure 1. Geometry, coordinate system and fluid velocity components for the liquid bridge

Proceedings of the 4th European Symposium on Materials Sciences under Microgravity, *Madrid, Spain*, 5-8 *April* 1983 (*ESA SP-191 – June 1983*).

1) Differential equation for the velocity potential in cylindrical coordinates

$$\frac{\partial^2\phi}{\partial z^2} + \frac{\partial^2\phi}{\partial r^2} + \frac{1}{r}\frac{\partial\phi}{\partial r} + \frac{\partial^2\phi}{\partial\theta^2} = 0 \quad \text{in } D_\eta \tag{1}$$

2) Kinematic boundary condition at the free surface, $r = \eta(z,\theta,t)$,

$$\frac{\partial\eta}{\partial t} = \frac{\partial\phi}{\partial r} - \frac{\partial\phi}{\partial z}\frac{\partial\eta}{\partial z} - \frac{1}{\eta^2}\frac{\partial\phi}{\partial\theta}\frac{\partial\eta}{\partial\theta} \quad \text{on } \eta. \tag{2}$$

3) Dynamic boundary condition expressed as the Bernoulli integral on the free surface,

$$\frac{\partial\phi}{\partial t} + \frac{1}{2}\{(\frac{\partial\phi}{\partial r})^2 + (\frac{\partial\phi}{\partial z})^2 + \frac{1}{\eta^2}(\frac{\partial\phi}{\partial\theta})^2\} - g_z z - g_x x + \frac{\sigma}{\rho}K = F(t) \quad \text{on } \eta, \tag{3}$$

where σ is the surface tension, ρ the density and K the local mean curvature of the free surface defined as

$$K = \frac{1}{\eta}\{\frac{1+\eta_z^2}{R} - (\frac{\eta\eta_z}{R})_z - (\frac{\eta_\theta}{\eta R})_\theta\}, \tag{4}$$

with $\eta R = \sqrt{\eta^2(1+\eta_z^2) + \eta_\theta^2}$.

$F(t)$ is the integral of Bernoulli equation, which is usually eliminated by redefinition of $\partial\phi/\partial t$.

4) Kinematic boundary condition at the solid end supports, $f_i(z,\theta,t,r) = 0$, $i=1,2,\ldots$, if relevant,

$$\frac{\partial f_i}{\partial t} + \frac{\partial f_i}{\partial r}\frac{\partial\phi}{\partial r} + \frac{\partial f_i}{\partial z}\frac{\partial\phi}{\partial z} + \frac{1}{r^2}\frac{\partial f_i}{\partial\theta}\frac{\partial\phi}{\partial\theta} = 0 . \tag{5}$$

In addition, contact angle conditions at the intersections of the free surface with the solid supports must be stated.

3. INFINITESIMAL ONE-PARAMETER TRANSFORMATION

Let an infinitesimal one-parameter transformation be defined as:

$$\begin{aligned} z^* &= z + \alpha^1(z,\theta,t,r,\phi)\varepsilon \\ \theta^* &= \theta + \alpha^2(z,\theta,t,r,\phi)\varepsilon \\ t^* &= t + \tau(z,\theta,t,r,\phi)\varepsilon \\ r^* &= r + \beta(z,\theta,t,r,\phi)\varepsilon \\ \phi^* &= \phi + \gamma(z,\theta,t,r,\phi)\varepsilon , \end{aligned}$$

where $\alpha^1, \alpha^2, \ldots$ are smooth functions defined in R^5 and ε a small parameter.

Let consider a smooth function $F(z^*,\theta^*,t^*,r^*,\phi^*)$, defined in R^5, which varies along the path curve (or orbit) of an arbitrary initial point z,θ,t,r,ϕ. For small values of ε,

$$\varepsilon\delta F = F(z^*,\theta^*,t^*,r^*,\phi^*) - F(z,\theta,t,r,\phi) = v\{F(z,\theta,t,r,\phi)\}\varepsilon ,$$

where the vector field

$$v = \alpha^1(z,\theta,t,r,\phi)\frac{\partial}{\partial z} + \alpha^2(z,\theta,t,r,\phi)\frac{\partial}{\partial\theta} + \tau(z,\theta,t,r,\phi)\frac{\partial}{\partial t} + \beta(z,\theta,t,r,\phi)\frac{\partial}{\partial r} + \gamma(z,\theta,t,r,\phi)\frac{\partial}{\partial\phi} , \tag{6}$$

is the infinitesimal generator of the one-parameter group of symmetries (tangent vector field). These symmetries are obtained by integration of the system of ordinary differential equations

$$\alpha^1 = \frac{dz}{d\varepsilon} , \quad \alpha^2 = \frac{d\theta}{d\varepsilon} , \quad \tau = \frac{dt}{d\varepsilon} , \quad \beta = \frac{dr}{d\varepsilon} , \quad \gamma = \frac{d\phi}{d\varepsilon} , \tag{7}$$

with $\varepsilon = 0$ taken as the identity element of the group.

The action of the group on a function ζ defined as

$$\phi = \zeta(z,\theta,t,r) ,$$

will be

$$\delta\zeta = \delta\phi - v_1\{\zeta\} , \tag{8}$$

where

$$\delta\phi = \gamma(z,\theta,t,r,\zeta(z,\theta,t,r))$$

and v_1 is the projection of v onto the space of independent variables,

$$v_1 = \alpha^1(z,\theta,t,r,\zeta)\frac{\partial}{\partial z} + \alpha^2(z,\theta,t,r,\zeta)\frac{\partial}{\partial\theta} + \tau(z,\theta,t,r,\zeta)\frac{\partial}{\partial t} + \beta(z,\theta,t,r,\zeta)\frac{\partial}{\partial r} .$$

In order to calculate the action of the group on the derivatives of ϕ which appear in Eqs. 1 to 3, let δ_k represent k times derivation with respect to independent variables. Application of Eq. 8 to

$$\delta_k\phi = \delta_k\zeta(z,\theta,t,r)$$

yields

$$\delta(\delta_k\zeta) = \delta(\delta_k\phi) - v_1\{\delta_k\zeta\}, \tag{9}$$

whereas, by derivating k times

$$\delta_k(\delta\zeta) = \delta_k[\delta\phi - v_1\{\zeta\}] . \tag{10}$$

Since the left hand sides of Eqs. 9 and 10 are equal,

$$\delta(\delta_k\phi) = \delta_k[\delta\phi - v_1\{\zeta\}] + v_1\{\delta_k\zeta\} . \tag{11}$$

Eq. 11 will be incorporated into the formula of prolongation (Ref. 3, pp. 41 and ff),

$$prv = v + \delta\phi_k\frac{\partial}{\partial\phi_k} , \tag{12}$$

where the subscript $k \geq 1$ denotes all the k-th and lower order derivatives of ϕ with respect to independent variables. Eq. 12 represents the tangent vector field prolonged up to order k to the space of ϕ derivatives.

3.1 Invariance of the differential equation 1

The infinitesimal criterion for invariance of Eq. 1, i.e.,

$$prv\{\Delta\phi\} = 0 \quad \text{whenever } \Delta\phi = 0 ,$$

will be explicited by taking into account Eqs. 6,

11 and 12, and by expressing ϕ_r in terms of second order derivatives through Eq. 1. This will lead to and expression which should vanish no matter the values of ϕ_k. Then the coefficients of the monomials involving ϕ_k or products of ϕ_k must vanish.

Table 1 below gives the coefficients of those monomials which, not being identically nil a priori, provide information on the functions α^1, α^2, τ, β and γ.

Table 1.

Terms Appearing in $prv\{\Delta\phi\} = 0$

Monomial	Coefficient
$\phi_z\phi_{zz}, \phi_r\phi_{zr}, \phi_\theta\phi_{z\theta}/r^2$	$-2\alpha^1_\phi$
$\phi_z\phi_{z\theta}, \phi_r\phi_{\theta r}, \phi_\theta\phi_{\theta\theta}/r^2$	$-2\alpha^2_\phi$
$\phi_z\phi_{zt}, \phi_r\phi_{tr}, \phi_\theta\phi_{\theta t}/r^2$	$-2\tau_\phi$
$\phi_z\phi_{zr}, \phi_r\phi_{rr}, \phi_\theta\phi_{\theta r}/r^2$	$-2\beta_\phi$
ϕ_z^2 , ϕ_θ^2 , ϕ_r^2	$\gamma_{\phi\phi}$
ϕ_{zr}	$-2(\alpha^1_r + \beta_z)$
$\phi_{z\theta}/r^2$	$-2(\alpha^1_\theta + r^2\alpha^2_z)$
$\phi_{\theta r}/r^2$	$-2(r^2\alpha^2_r + \beta_\theta)$
ϕ_{zt}	$-2\tau_z$
$\phi_{\theta t}/r^2$	$-2\tau_\theta$
ϕ_{rt}	$-2\tau_r$
ϕ_{zz}	$-2\alpha^1_z + \frac{\beta}{r} + r\Delta\beta - 2r\gamma_{\phi r}$
$\phi_{\theta\theta}/r^2$	$-2\{\alpha^2_\theta + \frac{\beta}{r}\} + \frac{\beta}{r} + r\Delta\beta - 2r\gamma_{\phi r}$
ϕ_{rr}	$-2\beta_r + \frac{\beta}{r} + r\Delta\beta - 2r\gamma_{\phi r}$
ϕ_z	$-\Delta\alpha^1 + 2\gamma_{\phi z}$
ϕ_θ/r^2	$-r^2\Delta\alpha^2 + 2\gamma_{\phi\theta}$
ϕ_t	$-\Delta\tau$
	$\Delta\gamma$

The differential equations which result from equating to zero the different coefficients are fulfilled by the following set of functions:

$$\alpha^1(z,\theta,t,r) = a^o(t) - b^1(t)z + c^1(\theta,t)r - 2c^2(\theta,t)zr \quad , \quad (13)$$

$$\alpha^2(z,\theta,t,r) = b^o(t) - \frac{\partial}{\partial\theta}\{c^o(\theta,t)\frac{1}{r} + c^1(\theta,t)\frac{z}{r} - c^2(\theta,t)\frac{z^2+r^2}{r}\},$$

$$\tau(t) \quad ,$$

$$\beta(z,\theta,t,r) = -c^o(\theta,t) - c^1(\theta,t)z - b^1(t)r + c^2(\theta,t)(z^2-r^2),$$

$$\gamma(z,\theta,t,r,\phi) = \phi\{c^2(\theta,t)r + C_{13}\} + \gamma^2(z,\theta,t,r) \quad ,$$

with

$$c^i(\theta,t) = C^i(t)\cos\theta + S^i(t)\sin\theta \quad , \quad i=0,1,2.$$

C_{13}, as well as the C_j used below, are integration constants. Subscripts and superscripts are arranged so that a cross-checking with the symmetries in the threedimensional case (Ref. 4) is facilitated as far as possible.

3.2 Invariance of the boundary condition Eq. 2

To express the invariance of the boundary conditions on $r = \eta(z,\theta,t)$ the vector field v must be prolonged to the derivatives of η on the free surface (Ref. 4).

$$prv_S = v_S + (\partial\phi_k)_S \frac{\partial}{\partial\phi_k} + \partial\eta_k \frac{\partial}{\partial\eta_k} \quad , \quad (14)$$

where S indicates that functions involved are to be calculated on the free surface.

Now, following with the function h

$$\eta = h(z,\theta,t)$$

the same steps as in Eqs. 8 to 11 with ζ,

$$\partial\eta_k = \partial_k[\partial\eta - v_o\{h\}] + v_o\{h_k\} \quad , \quad (15)$$

where

$$\partial\eta = \beta(z,\theta,t,\eta(z,\theta,t)) \quad ,$$

and

$$v_o = \alpha^1(z,\theta,t,\eta(z,\theta,t))\frac{\partial}{\partial z} + \alpha^2(z,\theta,t,\eta(z,\theta,t))\frac{\partial}{\partial\theta} + \tau(t)\frac{\partial}{\partial t} \quad .$$

(Recall Table 1 in connection with α^1, α^2 and τ).

The invariance of boundary condition Eq. 2 provides a set of ordinary differential equations, most of them duplicating those already established. The only coefficients which are not identically nil, after taking into account the results from Table 1, are summarized in Table 2.

Table 2.

Terms Appearing in $prv_S\{\eta_t - \phi_z\eta_z - \frac{1}{\eta^2}\phi_\theta\eta_\theta + \phi_r\}$

Monomial	Coefficient
$\eta_\theta\phi_\theta/\eta^2$, $\eta_z\phi_z$, ϕ_r	$\tau_t - 2\beta_r + \gamma_\phi$
η_z	$\alpha^1_t - \gamma_z$
η_θ/η^2	$\eta^2\alpha^2_t - \gamma_\theta$
	$\beta_t - \gamma_r$

The additional differential equations yield the following expressions for the components of v:

$$\alpha^1(z,\theta,t,r) = a^o(t) + \frac{C_{12}+C_{13}}{2}z + \{C_{10}\cos\theta + C_{11}\sin\theta\}r \quad , \quad (16)$$

$$\alpha^2(z,\theta,t,r) = \{C^o(t)\sin\theta - S^o(t)\cos\theta\}\frac{1}{r} + C_2 + \{C_{10}\sin\theta - C_{11}\cos\theta\}\frac{z}{r} ,$$

$$\tau(t) = C_{12}t + C_3 ,$$

$$\beta(z,\theta,t,r) = -\{C^o(t)\cos\theta + S^o(t)\sin\theta\} - \{C_{10}\cos\theta + C_{11}\sin\theta\}z + \frac{C_{12}+C_{13}}{2} r ,$$

$$\gamma(z,\theta,t,r,\phi) = C_{13}\phi - \{C_t^o(t)\cos\theta + S_t^o(t)\sin\theta\}r + a_t^o(t)z + \gamma^3(t) .$$

3.2 Invariance of the boundary condition Eq. 3

The process is quite similar to that pursued with Eq. 2.

The very involved expression of the curvature at the free surface, Eq. 4, greatly complicates the algebra. To circumvent this difficulty we first assume $\sigma = 0$ and calculate the symmetries, testing afterward which among the obtained symmetries also belong to the surface tension term.

The sole additional equation is

$$\gamma_t = g_z\alpha^1 + g_x\beta\cos\theta - g_x r\alpha^2\sin\theta + (C_{12}-C_{13})g_z z + (C_{12}-C_{13})g_x r\cos\theta . \qquad (17)$$

After substitution of α^1, α^2 and β from Eqs. 16 into Eq. 17, the following system of ordinary differential equations result:

$$C_{tt}^o = -C_{10}g_z - \frac{3C_{12}-C_{13}}{2} g_x , \qquad (18)$$

$$S_{tt}^o = -C_{11}g_z + C_2 g_x ,$$

$$a_{tt}^o = \frac{3C_{12}-C_{13}}{2} g_z - C_{10}g_x ,$$

$$\gamma_t^3 = a^o(t)g_z - C^o(t)g_x ,$$

which can be integrated both when the gs are constants or known functions of t.

In order to keep the analysis of the results within reasonable bounds we will restrict ourselves to the case

$$g_x = 0 , \quad g_z = g , \quad g \text{ time independent} ,$$

this furnishes the following expressions for the components of v:

$$\alpha^1(z,\theta,t,r) = C_1 + C_9 t + \frac{3C_{12}-C_{13}}{2} gt^2 + \frac{C_{12}+C_{13}}{2} z + \{C_{10}\cos\theta + C_{11}\sin\theta\}r , \qquad (19)$$

$$\alpha^2(z,\theta,t,r) = C_2 - \{(\frac{C_{10}}{2} gt^2 - C_7 t - C_5)\sin\theta - (\frac{C_{11}}{2} gt^2 - C_8 t - C_6)\cos\theta\}\frac{1}{r} + \{C_{10}\sin\theta - C_{11}\cos\theta\}\frac{z}{r} ,$$

$$\tau(t) = C_3 + C_{12}t ,$$

$$\beta(z,\theta,t,r) = \{(\frac{C_{10}}{2} gt^2 - C_7 t - C_5)\cos\theta + (\frac{C_{11}}{2} gt^2 - C_8 t - C_6)\sin\theta\} - \{C_{10}\cos\theta + C_{11}\sin\theta\}z + \frac{C_{12}+C_{13}}{2} r ,$$

$$\gamma(z,\theta,t,r,\phi) = C_4 + C_1 gt + \frac{C_9}{2} gt^2 + \frac{3C_{12}-C_{13}}{2} g^2t^3 + \frac{3C_{12}-C_{13}}{2} gtz + C_9 z + \{(C_{10}gt - C_7)\cos\theta + (C_{11}gt - C_8)\sin\theta\}r + C_{13}\phi .$$

4. RESULTING SYMMETRIES

The Lie algebra of infinitesimal symmetries can be obtained by asigning arbitrary values to the integration constants, C_1, C_2, ..., in turn, with the rest equal to zero.

In the case of axial, constant, gravity these symtries are:

1 $C_1 = 1$ $\quad z^* = z + \varepsilon$,
$\phi^* = \phi + \varepsilon gt$,

whereas the other variables remain unchanged. This symmetry represents an axial translation.

2 $C_2 = 1$ $\quad \theta^* = \theta + \varepsilon$,
Rotation around the z axis.

3 $C_3 = 1$ $\quad t^* = t + \varepsilon$,
Time translation.

4 $C_4 = 1$ $\quad \phi^* = \phi + \varepsilon$,
Variation of ϕ level.

5 $C_5 = -1$ $\quad r^*\cos\theta^* = r\cos\theta + \varepsilon$,
$r^*\sin\theta^* = r\sin\theta$,
x - translation.

6 $C_6 = -1$ $\quad r^*\cos\theta^* = r\cos\theta$,
$r^*\sin\theta^* = r\sin\theta + \varepsilon$,
y - translation.

7 $C_7 = -1$ $\quad r^*\cos\theta^* = r\cos\theta + \varepsilon t$,
$r^*\sin\theta^* = r\sin\theta$,
$\phi^* = \phi + \varepsilon r\cos\theta + \frac{1}{2}\varepsilon^2 t$,
x - Galilean boost.

8 $C_8 = -1$ $\quad r^*\cos\theta^* = r\cos\theta$,
$r^*\sin\theta^* = r\sin\theta + \varepsilon t$,
$\phi^* = \phi + \varepsilon r\sin\theta + \frac{1}{2}\varepsilon^2 t$,
y - Galilean boost.

9 $C_9 = 1$ $\quad z^* = z + \varepsilon$,
$\phi^* = \phi + \varepsilon(z + \frac{1}{2} gt^2) + \frac{1}{2}\varepsilon^2 t$,
z - Galilean boost.

10 $C_{10} = 1$ $\quad r^*\cos\theta^* = r\cos\theta\cos\varepsilon + (\frac{1}{2}gt^2 - z)\sin\varepsilon$,
$r^*\sin\theta^* = r\sin\theta$,
$z^* = z\cos\varepsilon + r\cos\theta\sin\varepsilon + \frac{1}{2}gt^2(1-\cos\varepsilon)$,
$\phi^* = \phi + gt\{r\cos\theta\sin\varepsilon + (\frac{1}{2}gt^2 - z)(1-\cos\varepsilon)\}$,
Gravity-compensated rotation around y-axis.

11 $C_{11} = 1$ $\quad r^*\cos\theta^* = r\cos\theta$,
$r^*\sin\theta^* = r\sin\theta\cos\varepsilon + (\frac{1}{2}gt^2 - z)\sin\varepsilon$,
$z^* = z\cos\varepsilon + r\sin\theta\sin\varepsilon + \frac{1}{2}gt^2(1-\cos\varepsilon)$,
$\phi^* = \phi + gt\{r\sin\theta\sin\varepsilon + (\frac{1}{2}gt^2 - z)(1-\cos\varepsilon)\}$,
Gravity-compensated rotation around x-axis.

12 $C_{12} = \frac{3}{2}$ $\quad z^* = \lambda\{z - \frac{1}{3}gt^2(1-\lambda^2)\}$,
$C_{13} = \frac{1}{2}$ $\quad t^* = \lambda^{3/2}t$,
$r^* = \lambda r$,
$\phi^* = \lambda^{1/2}\{\phi - \frac{4}{5}gtz(1-\lambda^2) + \frac{2}{45}g^2t^3(1 - 6\lambda^2 + 5\lambda^4)\}$,
Scaled acceleration.

All these symmetries remain as such when surface tension is taken into account. In particular, it can be seen that 12 is the only combination of C_{12} and C_{13} leading to a symmetry even when $\sigma \neq 0$.

Notice that the above symmetries are related to the ten-parameter Galilei-Newton group of classical Mechanics, namely:

1. The three-parameter subgroup of space-translations.
2. The one-parameter subgroup of time-translations.
3. The three-parameter subgroup of rigid rotations.
4. The three-parameter subgroup of changes to moving axes being translated with constant velocity.

On the other hand, the scaling $(\lambda z, \theta, \lambda^{1/2}t, \lambda r, \lambda^{3/2}\phi)$, which looks obvious from considerations of Dimensional Analysis, is absent because it is not a symmetry when $\sigma \neq 0$. It can, however, be deduced from Eqs. 19 with $C_{12} = 1/2$, $C_{13} = 3/2$.

4.1 Additional boundary conditions

The fulfillment of additional boundary conditions decreases the number of symmetry groups. For example, if the bridge is supported between two quiescent, coaxial, solid discs of diameter D placed at $z = \pm 1$, and the free surface is assumed to remain attached to the disc edges, the following additional boundary conditions must be fulfilled:

$$\phi_z = 0 \quad \text{on } z = \pm 1$$
$$\eta = D/2 \ .$$

$\delta\phi_z = 0$ implies $C_9 = C_{10} = C_{11} = C_{12} = C_{13} = 0$, and $\beta = 0$ adds to the above the following restrictions, $C_5 = C_6 = C_7 = C_8 = 0$.

Then, only 1 to 4 remain as symmetry groups. Nevertheless, 5 to 12 should not be overlooked as they presumably describe the behavior of the bridge (and, particularly, surface waves) far from the end discs.

5. THE HAMILTONIAN FORMULATION

Consider an infinitely long liquid column disturbed in such a manner that $\eta - D/2$ vanishes together with all its derivatives as $|z| \to \infty$.

Specification of the quantities $\eta(z,\theta,t)$ and $\psi(z,\theta,t) = \phi(z,\theta,t,\eta(z,\theta,t))$ fully defines the fluid flow since the boundary value problem for Laplace's equation has a unique solution. Furthermore, it has been shown by Zakharov (Ref. 6) that if E is the total energy of the system, then

$$\eta_t = \frac{\delta E}{\delta \psi} \qquad (20)$$
$$\psi_t = -\frac{\delta E}{\delta \eta} \ ,$$

where the symbols $\delta E/\delta\psi$ and $\delta E/\delta\eta$ denote variational or functional derivatives. See Appendix I.

Equations 20 are Hamilton's equations, ψ and η are cannonical variables, ψ is a generalized coordinate and η a generalized momentum.

For later reference, Eq. 20 can be written down in matrix form as follows:

$$\begin{bmatrix} \eta_t \\ \psi_t \end{bmatrix} = J \begin{bmatrix} E_\eta \\ E_\psi \end{bmatrix} \quad \text{with} \quad J = \begin{pmatrix} 0 & 1 \\ -1 & 0 \end{pmatrix} . \qquad (21)$$

5.1 Olver's version of Noether theorem

Let

$$v = \sum_i \alpha^i \frac{\partial}{\partial x^i} + \tau\frac{\partial}{\partial t} + \sum_j \gamma^j \frac{\partial}{\partial \phi^j} \ ,$$

be the infinitesimal generator of a one-parameter group of symmetries.

$\phi = (\phi^1 \ \ldots \ \phi^q)$ is the set of dependent variables, and

$x = (x^1 \ \ldots \ x^p)$ the independent space variables.

If P^j is deduced from

$$\sum_j J_{ij}P^j = \gamma^i - \sum_j \alpha^j\phi^i_j - \tau\phi^i_t \ ,$$

and a T exists such that

$$dT = \sum_j P^j d\phi^j \qquad (22)$$

then (Refs. 4,5) T is a conserved density. This means that for any p-dimensional region with piecewise smooth boundary $\delta\Omega$, any time interval $t_o \leq t \leq t_1$, and for all solutions ϕ of an evolution equation like Eq. 21, the difference on the value of a spatial integral of T at two different instants depends only on the behavior of ϕ and its derivatives at the boundary of the region

$$\int_\Omega T(x,t,\phi)dx \Big|_{t=t_o}^{t=t_1} = \int_{t_o}^{t_1}\{\int_{\partial\Omega} A\,ds\}dt \ , \qquad (23)$$

for some p-tuple functions A.

In our particular case: $\alpha^i = (\alpha^1, \alpha^2)$, $\tau = \tau$, $\gamma^i = (\beta, \gamma)$, $\phi^i = (\eta, \psi)$, and the conserved densities, T, are given by

$$dT = -\{\gamma - \alpha^1\psi_z - \alpha^2\psi_\theta - \tau\psi_t\}d\eta + \{\beta - \alpha^1\eta_z - \alpha^2\eta_\theta - \tau\eta_t\}d\psi \ . \qquad (24)$$

In order to calculate α^i, τ and γ^i, we come back to Eqs. 19 asigning values to the constants $C_1, \ldots, C_{13}$.

5.2 The conserved densities

Taking $C_1 = -1$, $C_j = 0$ otherwise, Eqs. 19, 22 and 24 furnish the first conserved density, T_1.

$$dT_1 = gtd\eta + \psi d\eta_z + \eta_z d\psi - \frac{d}{dz}\{\psi d\eta\} .$$

Terms like $d\{\psi d\eta\}/dz$ will have influence only on the right hand side of Eq. 23, through integration by parts, and then can be left aside

$$T_1 = gt\eta + \eta_z\psi . \qquad (25)$$

If we take $C_2 = -1$, $C_{j\neq 2} = 0$ or $C_4 = -1$, $C_{j\neq 4} = 0$, we arrive, respectively, to

$$T_2 = \eta_\theta\psi \quad , \quad T_4 = \eta .$$

With $C_3 = -1$, $C_{j\neq 3} = 0$ the following expression results:

$$dT_3 = -\psi_t d\eta + \eta_t d\psi .$$

This equation, together with Eqs. 20, indicates that T_3 is the hamiltonian density function the volume integral of which equals the energy, E, of the system.

$$T_3 = \frac{1}{2}\psi\nabla\phi\cdot\vec{n}R - \frac{1}{2}gz\eta + \frac{\sigma}{\rho}R , \qquad (26)$$

where $\vec{n}R = \vec{i}_r - (\eta_\theta/\eta)\vec{i}_\theta - \eta_z\vec{i}_z$, (27)

and R was given in connection with Eq. 4.

Taking $C_5 = -1$, $C_{j\neq 5} = 0$

$$dT_5 = d[\psi \frac{\partial}{\eta\partial\theta}\{\eta\sin\theta\}] - \frac{\partial}{\eta\partial\theta}[\psi d\{\eta\sin\theta\}] ,$$

then

$$T_5 = \psi \frac{\partial}{\eta\partial\theta}\{\eta\sin\theta\} \qquad (28)$$

and, similarly

$$T_6 = -\psi \frac{\partial}{\eta\partial\theta}\{\eta\cos\theta\} .$$

T_7 to T_9 can be expressed as combinations of T_1, T_5 and T_6 as follows:

$$T_7 = tT_5 \quad , \quad T_8 = tT_6 \qquad (29)$$

$$T_9 = tT_1 + \{z - \frac{1}{2}gt^2\}\eta .$$

Concerning T_{10} and T_{11},

$$dT_{10} = (z - \frac{1}{2}gt^2)dT_5 - \eta\cos\theta dT_1$$

$$dT_{11} = (z - \frac{1}{2}gt^2)dT_6 - \eta\sin\theta dT_1 ,$$

from which the following two conserved densities result,

$$T_{10} = (z - \frac{1}{2}gt^2)T_5 + \frac{1}{2}gt\eta^2\cos\theta + \frac{1}{2}\psi(\eta^2)_z\cos\theta , \qquad (30)$$

$$T_{11} = (z - \frac{1}{2}gt^2)T_6 + \frac{1}{2}gt\eta^2\sin\theta + \frac{1}{2}\psi(\eta^2)_z\sin\theta .$$

Finally, when $C_{12} = 3/2$, $C_{13} = 1/2$, $C_j = 0$ otherwise, the resulting expressions of dT_{12} is not an exact derivative of a density.

5.3 Physical interpretation of the conserved densities

In order to look at the physical meaning of the conserved densities, the integral in the left hand side of Eq. 24 will be calculated over part of the free surface. To this aim, we introduce the simply-connected control volume, $\mathcal{D}$, sketched in Figure 2. This control volume is bounded by the part, S, of the free surface plus a permeable, fixed in space, control surface, Γ, within the liquid column. Since Γ can be chosen at convenience it is supposed to be normal to the undisturbed cylindrical free surface at the intersection.

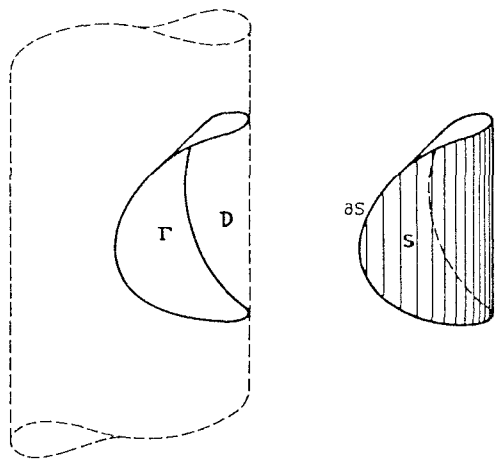

Figure 2. The control volume $\mathcal{D}$ bounded by a portion, S, of the free surface and an arbitrary surface, Γ.

Let a vector $\vec{F}_i = F_i^r\vec{i}_r + F_i^\theta\vec{i}_\theta + F_i^z\vec{i}_z$, be deduced from

$$T_i = F_i^r - F_i^\theta\frac{\eta_\theta}{\eta} - F_i^z\eta_z . \qquad (31)$$

By Gauss theorem

$$I_i = \int_{\partial\mathcal{D}} T_i\eta d\theta dz = \int \nabla\cdot\vec{F}_i dV , \qquad (32)$$

where the divergence $\nabla\cdot\vec{F}_i$ is given by

$$\nabla\cdot\vec{F}_i = \frac{1}{r}\{\frac{\partial}{\partial r}(rF_i^r) + \frac{\partial}{\partial\theta}F_i^\theta + \frac{\partial}{\partial z}(rF_i^z)\} .$$

The resulting integrals of conserved densities, I_i, are listed in the following

$$I_1 = 2gtV - \int_{\mathcal{D}} V_z dV , \qquad (33)$$

z-momentum.

$$I_2 = \int_{\mathcal{D}} rV_\theta dV , \qquad (34)$$

z-angular momentum.

$$I_3 = \int_{\mathcal{D}} (\frac{1}{2}q^2 - gz)dV + \frac{\sigma}{\rho}\int_{\partial\mathcal{D}} R\eta d\theta dz , \qquad (35)$$

kinetic, potential and surface energy.

$$I_4 = 2V , \qquad \text{mass.} \qquad (36)$$

$$I_5 = \int_{\mathcal{D}} V_x dV \quad , \quad I_6 = \int_{\mathcal{D}} V_y dV , \qquad (37)$$

x and y momenta

$$I_7 = tI_5 \quad , \quad I_8 = tI_6 \ . \tag{38}$$

$$I_9 = 2\int_{\mathcal{D}} (z + \frac{1}{2} gt^2)d\mathcal{V} - t\int_{\mathcal{D}} V_z d\mathcal{V} \ . \tag{39}$$

$$I_{10} = \int_{\mathcal{D}} (z - \frac{1}{2}gt^2)V_x d\mathcal{V} + \frac{3}{2} gt \int_{\mathcal{D}} x d\mathcal{V} - \int_{\mathcal{D}} xV_z d\mathcal{V} \ . \tag{40}$$

$$I_{11} = \int_{\mathcal{D}} (z - \frac{1}{2}gt^2)V_y d\mathcal{V} + \frac{3}{2} gt \int_{\mathcal{D}} y d\mathcal{V} - \int_{\mathcal{D}} yV_z d\mathcal{V} \ . \tag{41}$$

The physical interpretations attached to these conserved densities, which are trivial at first, become more complicated in the last five cases, Eqs. 38 to 41. Nevertheless, some information can be deduced from the corresponding symmetries listed in §4. For instance, whereas Eqs. 37 come from time-independent x or y translations, Eqs. 38 concern a fluid domain observed in a frame of reference being translated with constant velocity in x or y directions. On the other hand, I_{10} and I_{11}, Eqs. 40 and 41, can be easily interpreted when g = 0 as representing y and x angular momenta, respectively. Clearly these angular momenta are observed in axes accelerating vertically to cancel gravity.

6. THE CONSERVATION LAWS

The last step in the search for conservation laws for liquid bridges will consist in calculating time derivatives of the integrals I_i. This will bring to light the dependence of the conserved densities on the fluid behavior at the boundaries of the control volume.

Let T_i be a conserved density not explicitly including the variable t, as is the case for T_2 to T_6. Differentiation under the volume-integral sign in Eq. 32, remembering that Γ is fixed in space whereas S is not, yields

$$\frac{dI_i}{dt} = \int_{\mathcal{D}} \nabla\cdot\vec{F}_{it} d\mathcal{V} + \int_S \nabla\cdot\vec{F}_i (\nabla\phi\cdot\vec{n}) R\eta d\theta dz \ . \tag{42}$$

Application of Gauss theorem to the first term in the right hand side of Eq. 42 results in:

$$\frac{dI}{dt} = \int_S (\vec{F}_{it} + \nabla\cdot\vec{F}_i \nabla\phi)\cdot\vec{n} R\eta d\theta dz + \int_\Gamma \vec{F}_{it}\cdot\vec{n} R r d\theta dz \ . \tag{43}$$

Development of the cases i = 4 and i = 1, the final results of which are well known (conservation of mass and of z-momentum, respectively), could guide in the derivation of the different conservation laws.

When i = 4, Eq. 31 gives $\vec{F}_4 = \eta\vec{i}_r$ and $\nabla\cdot\vec{F}_4 = 2$.

On the other hand, $\vec{F}_{4t} = 0$ everywhere except on S where, according to Eq. 2,

$$\vec{F}_{4t} = (\nabla\phi\cdot\vec{n}R)\vec{i}_r \ .$$

Thus, Eq. 42, together with Gauss theorem, yields

$$\frac{dI_4}{dt} = -2\int_\Gamma \nabla\phi\cdot\vec{n} R r d\theta dz \ , \tag{44}$$

which merely indicates that the volume changes in $\mathcal{D}$ are due to the fluid flowing through surface Γ.

The case i = 1 is a bit more complicated but it illustrates how to proceed in other cases.

Let us consider the combination $T_1 - gtT_4$. Equation 43 with $\vec{F}_1 = -\psi\vec{i}_z$, $\nabla\cdot\vec{F}_1 = -\psi_z$ becomes,

$$\frac{dI_1}{dt} - gI_4 - gt\frac{dI_4}{dt} =$$

$$= -\int_S (\psi_t \vec{i}_z + \psi_z \nabla\phi)\cdot\vec{n} R\eta d\theta dz - \int_\Gamma \psi_t \cdot\vec{n} R r d\theta dz \ . \tag{45}$$

Bernoulli's equation reads

$$\psi_t = -\frac{1}{2}|\nabla\phi|^2 + gz - \frac{\sigma}{\rho} K \quad \text{on S} \tag{46}$$

and

$$\psi_t = -\frac{1}{2}|\nabla\phi|^2 + gz - \frac{p}{\rho} \quad \text{on } \Gamma \ .$$

The first of Eqs. 46 is again Eq. 3, with $g_x = 0$, rewritten in a form more convenient for present purposes.

Bringing Eqs. 46 to Eq. 45 and applying Gauss theorem to the solenoidal vector

$$\frac{1}{2}|\nabla\phi|^2\vec{i}_z - \phi_z\nabla\phi$$

yields

$$\frac{dI_1}{dt} - gI_4 - gt\frac{dI_4}{dt} = \int_\Gamma \phi_z \nabla\phi\cdot\vec{n} R r d\theta dz -$$

$$- g\int_{\partial\mathcal{D}} z\vec{i}_z\cdot\vec{n} R r d\theta dz + \frac{\sigma}{\rho}\int_S K\vec{i}_z\cdot\vec{n} R\eta d\theta dz +$$

$$+ \frac{1}{\rho}\int_\Gamma p\vec{i}_z\cdot\vec{n} R r d\theta dz \ .$$

The first and last terms in the right hand side of Eq. 47 are, respectively, the z-momentum flux and z component of pressure forces on Γ. Application of Gauss theorem to the vector $z\vec{i}_z$ indicates that the second term is equal to $-gI_4/2$, partially cancelling a similar term in the left hand side. Finally, the third term is the z-component of the capillary pressure on S, which can be expressed as a line integral along the intersection of S and Γ by application of Green's formula (Ref. 7).

$$\int_S K\vec{i}_z\cdot\vec{n} R\eta d\theta dz = \int_{\partial S} P d\theta + Q dz \ , \tag{48}$$

where P and Q are deduced from

$$\frac{\partial P}{\partial z} - \frac{\partial Q}{\partial\theta} = K\eta_z\eta \ .$$

Taking the mean curvature, K, from Eq. 4,

$$P = \frac{\eta^2 + \eta_\theta^2}{\eta R} \quad , \quad Q = \frac{\eta_z\eta_\theta}{\eta R} \ . \tag{49}$$

The line integral in Eq. 47 should be taken such that the interior of the surface S lies on the left when moving along ∂S.

The other conservation laws follow in a completely similar way.

7. CONCLUSIONS

Integral Conservation Laws for surface disturbances in inviscid liquid bridges have been systematically obtained. Although the aim of the present exercise

has been mastering the mathematical routine through the obtention of physically palatable results, the same technique can be used in more complicated cases, for instance, when the gravity field, although still parallel, is no longer time independent in both intensity and direction.

Acknowledgment: The interest of the author in this mathematical technique aroused after attending a short course given by P.J. Olver at the School of Aeronautics, Madrid, in July 1982.
The author is also indebted to his colleague J.M. Vega for most useful advice.
This work has been sponsored by the Spanish Space Reasearch Commission (CONIE).

APPENDIX I

Derivation of Eqs. 20

Let E_K, V_g and V_σ be respectively the kinetic, potential and surface energy of a fluid volume, D_η, limited by a free surface η. The total energy of the system, E, will be:

$$E = E_K + V_g + V_\sigma$$

1. Variation of the kinetic energy, E_K.

$$E_K = \frac{1}{2}\int_{D_\eta} |\nabla\phi|^2 dV ,$$

$$\delta E_K = \int_{D_\eta} \nabla\delta\phi\cdot\nabla\phi dV + \frac{1}{2}\int_\eta |\nabla\phi|^2 \delta\eta\, \eta d\theta dz .$$

Application of Gauss theorem to the first integral in the right hand side yields

$$\delta E_K = \int_\eta (\delta\phi \frac{\partial\phi}{\partial n} R + \frac{1}{2}|\nabla\phi|^2\delta\eta)\eta d\theta dz .$$

Being ψ the velocity potential, ϕ, particularized on η,

$$\delta\psi = \delta\phi + \frac{\partial\phi}{\partial r}\delta\eta ,$$

then

$$\delta E_K = \int_\eta [\frac{\partial\phi}{\partial n} R\delta\psi + (\frac{1}{2}|\nabla\phi|^2 - \frac{\partial\phi}{\partial r}\frac{\partial\phi}{\partial n} R)\delta\eta]\eta d\theta dz .$$

and, finally

$$\frac{\delta E_K}{\delta\psi} = \frac{\partial\phi}{\partial n} R ,$$

$$\frac{\delta E_K}{\delta\eta} = \frac{1}{2}|\nabla\phi|^2 - \frac{\partial\phi}{\partial r}\frac{\partial\phi}{\partial n} R .$$

2. Variation of the potential energy, V_g.

$$V_g = -g_z\int_{D_\eta} dV - g_x\int_D dV .$$

Following with the time-independent vector

$$-g_z z\vec{i}_z - g_x x\vec{i}_x$$

the same steps as with $\phi\nabla\phi$ above, we reach

$$\frac{\delta V_g}{\delta\eta} = -g_z z - g_x x$$

3. Variation of the surface energy, V_σ.

$$V_\sigma = \frac{\sigma}{\rho}\int_\eta R\eta d\theta dz .$$

Now the relevant vector is $\vec{n}$, which on the free surface, η, is related to the mean curvature, K, through $\nabla\cdot\vec{n} = K$ (Eq. 4). Then

$$\frac{\delta V_\sigma}{\delta\eta} = \frac{\sigma}{\rho} K$$

Adding up the several contributions to the total energy

$$\frac{\delta E}{\delta\psi} = \frac{\partial\phi}{\partial n} R$$

$$\frac{\delta E}{\delta\eta} = \frac{1}{2}|\nabla\phi|^2 - \frac{\partial\phi}{\partial r}\frac{\partial\phi}{\partial n} R - g_z z - g_x x + \frac{\sigma}{\rho} K .$$

On the other hand, Eq. 2 indicates that

$$\frac{\partial\phi}{\partial n} R = \eta_t ,$$

whereas Eq. 3,

$$\frac{1}{2}|\nabla\phi|^2 - \frac{\partial\phi}{\partial r}\frac{\partial\phi}{\partial n} R - g_z z - g_x x + \frac{\sigma}{\rho} K = -\frac{\partial\phi}{\partial t} - \frac{\partial\phi}{\partial r}\eta_t ,$$

from which Eqs. 20 follow.

8. REFERENCES

1. Birkhoff G 1960 *Hydrodynamics*, Princeton University Press, Princeton, N.J., 117-147.

2. Bluman G W & Cole J D 1974 *Similarity Methods for Differential Equations*, Springer-Verlag, New York, 143-257.

3. Ovsiannikov L V 1982 *Group Analysis of Differential Equations*, Academic Press, New York, 341-391.

4. Benjamin T B & Olver P J 1982, Hamiltonian structure, symmetries and conservation laws for water waves, *J. Fluid Mech.*, 125, 137-185.

5. Olver P J 1980, On the Hamiltonian structure of evolution equations, *Math. Proc. Camb. Phil. Soc.*, 88, 71-88.

6. Zakharov V E 1968, Stability of periodic waves of finite amplitude on the surface of a deep fluid, *J. Appl. Mech. Tech. Phys.*, 2, 190-194.

7. Struik D J 1950 *Lectures on Classical Differential Geometry*, Addison-Wesley Publishing Company, Inc. Reading, Mass, 153-154.

THE BREAKING OF AXISYMMETRIC NON-CYLINDRICAL LIQUID BRIDGES

J. Meseguer, A. Sanz & D. Rivas

Laboratorio de Aerodinámica, Universidad Politécnica de Madrid, Spain

ABSTRACT

A numerical study of the dynamic behaviour of axisymmetric inviscid liquid bridges near the stability limit of minimum volume has been made by using an one-dimensional slice model. This model has been already used to study the behaviour of cylindrical bridges both analytically and numerically. Although its validity is questionable regarding short bridges, it seems to be appropriate for sufficiently slender bridges. In this study, the interface evolution of non-cylindrical configurations as well as overall data (such as the breaking time, or partial volume of the resulting drops) which can be easily verified experimentally, have been numerically obtained.

Keywords: Floating Zone, Liquid Bridge, One-dimensional Slice Model, Microgravity, Interfaces.

1. INTRODUCTION

The stability of axisymmetric liquid bridges has been studied mainly from the static point of view (Refs. 1,2). Recently attempts have been made to study the dynamics of liquid bridges, and a special attention has been devoted to the breaking of inviscid liquid bridges having cylindrical volume (Ref. 3).

Static considerations show that, when the stability limit is reached, a bifurcation to unstable equilibrium shapes occurs, whose character depend on the slenderness of the bridge, $\Lambda = L/(2R)$; L being the length of the liquid column and 2R the diameter of the disks (Figure 1). The unstable shapes are symmetrical or non-symmetrical (in respect of the middle plane parallel to the disks) if $\Lambda < \Lambda_B$ or $\Lambda > \Lambda_B$, respectively, where $\Lambda_B = 2.128$ (Ref. 2). It could be deduced from that change in the unstable equilibrium shapes that the breaking process will take place in a similar way, producing two caps of equal volume in the former case and different volumes in the latter, and in fact, this phenomenom has been experimentally observed (Ref. 4) and calculated in the case of cylindrical liquid bridges (Ref. 3).

The aim of this paper is to analyse, using an one-dimensional slice model, the aforementioned behaviour, pointing out its main features and yielding results that could be experimentally checked as easily as possible, in order to evaluate the predicting ability of the model.

From experiments and numerical studies it can be deduced that the breaking process consists of two main stages: a very slow starting up and a very fast ending. This initial slowness posses a great problem in checking some theoretical results. For instance, the breaking time is nor clearly defined experimentally because of the difficulty in stablishing the starting point and the initial perturbation, that is, the correspondence between initial conditions and results. However there is another characteristic of the breaking process which may be more easily checked: the volume of the two caps resulting after breakage. Numerical results shown in Ref. 3 seem to indicate that the volume of the

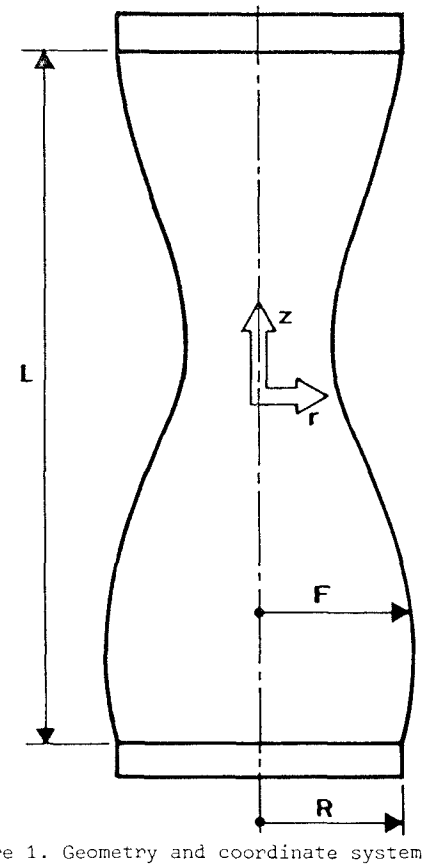

Figure 1. Geometry and coordinate system for the liquid bridge.

Proceedings of the 4th European Symposium on Materials Sciences under Microgravity, *Madrid, Spain*, 5-8 *April* 1983 (*ESA SP-191 – June* 1983).

caps mainly depends on the slenderness of the liquid bridge and not on the initial perturbation of the interface, rendering this volume splitting a good candidate to be experimentally checked.

Although some analytical work can be done in the case of cylindrical bridges, this would be extremely difficult in the non-cylindrical case, due to the complexity of the initial shape and its derivatives, needed to calculate the capillary-pressure gradients acting on the liquid column. Thus we have restricted the study to numerical computations. To carry out this analysis we consider an axisymmetric, inviscid liquid bridge, held by surface-tension forces between two coaxial, parallel, equal-diameter solid disks, with anchored edges as sketched in Figure 1. Additional hypothesis are:

1- Internal movement in the liquid bridge is due only to capillary-pressure gradients generated by the deformation of the interface.
2- The gas atmosphere surrounding the liquid does not affect the dynamics of the liquid bridge.
3- Gravity as well as inertia forces due to a non-uniform displacement of the liquid bridge as a whole are absent.
4- Since only axisymmetric configurations are considered, the problem is independent of the azimuthal coordinate.
5- Liquid density, ρ, as well as surface tension, σ, are uniform and constant.

2. THE ONE-DIMENSIONAL SLICE MODEL

The slice model is similar to the one-dimensional model derived by Lee (Refs. 5-7) for the study of the breaking of inviscid capillary jets. In this model the axial velocity is assumed to depend only on the axial coordinate and time. Within this simplification the radial momentum equation becomes decoupled from the continuity and axial momentum equations, and in this way the study of the liquid-bridge evolution is reduced to solving the last two equations. In the following, all physical quantities are made dimensionless using the characteristic length R and the characteristic time $(\rho R^3/\sigma)^{1/2}$.

Let F(z,t) and W(z,t) represent the liquid-bridge radius and the axial velocity respectively. The problem is better adapted for computations by choosing as working variables $S(z,t) = F^2$ and $Q(z,t) = F^2W$. Using these variables, the complete set of equations for the one-dimensional slice model are:

I) Continuity equation

$$S_t + Q_z = 0 \ . \qquad (1)$$

II) Axial momentum equation

$$Q_t + (Q^2/S)_z = - SP_z \ , \qquad (2)$$

where the pressure is related to S through

$$P = 4(2S + S_z^2 - SS_{zz})(4S+S_z^2)^{-3/2} \ . \qquad (3)$$

Boundary conditions are

$$Q(\pm\Lambda,t) = S(\pm\Lambda,t) - 1 = 0 \ , \qquad (4)$$

and initial conditions

$$Q(z,0) = 0 \ , \ S(z,0) = F_o^2(z) + S_o(z) \ , \qquad (5)$$

$F_o(z)$ being the equation of the undisturbed interface enclosing minimum volume of liquid, that is, the configuration at the stability limit, calculated in Ref. 2 (Figure 2), and $S_o(z)$ the appropriate initial perturbation imposed to break the liquid bridge, namely:

$$S_o(z) = \varepsilon(\varepsilon-2)\sin\frac{\pi z}{\Lambda} \ , \qquad (6)$$

for non-symmetrical perturbations, and

$$S_o(z) = \frac{\varepsilon(\varepsilon-2)}{1-\cos\delta}(\cos\delta - \cos\frac{\delta z}{\Lambda}) \ , \qquad (7)$$

with $\delta = 4.4934$ rad., for symmetrical ones.

In these last two expressions ε is a small parameter giving the amplitude of the interface radius perturbation when $\Lambda = \pi$ (that is, $F_o = 1$). Perturbations are assumed to be sinusoidal in the cross-sectional area and not in the radius because with this choice the volume of the distorted configurations exactly equals that of the undisturbed one.

We have choosen as undisturbed shapes, $F_o(z)$, precisely those corresponding to the stability limit in order to study the breaking from the limit itself. The detailed analysis near the limit has been already made in the cylindrical case (Ref. 3) and the main features remain the same for other shapes in the stability limit.

The numerical integration of this set of hyperbolic differential equations has been performed by using the finite-difference Lax-Wendroff method (Refs. 8,9) on a Hewlett Packard 9845B desktop computer. Details on numerical method and computations, mainly those regarding the formulation of boundary conditions, can be found in Ref. 3 abovementioned.

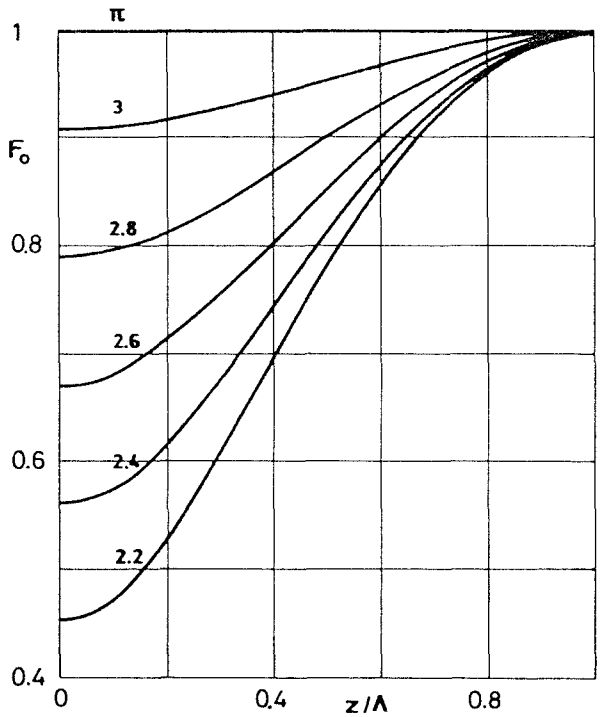

Figure 2. Interface shapes of a liquid bridge at the minimum-volume stability limit. Numbers on curves indicate the value of the slenderness, $\Lambda = L/(2R)$.

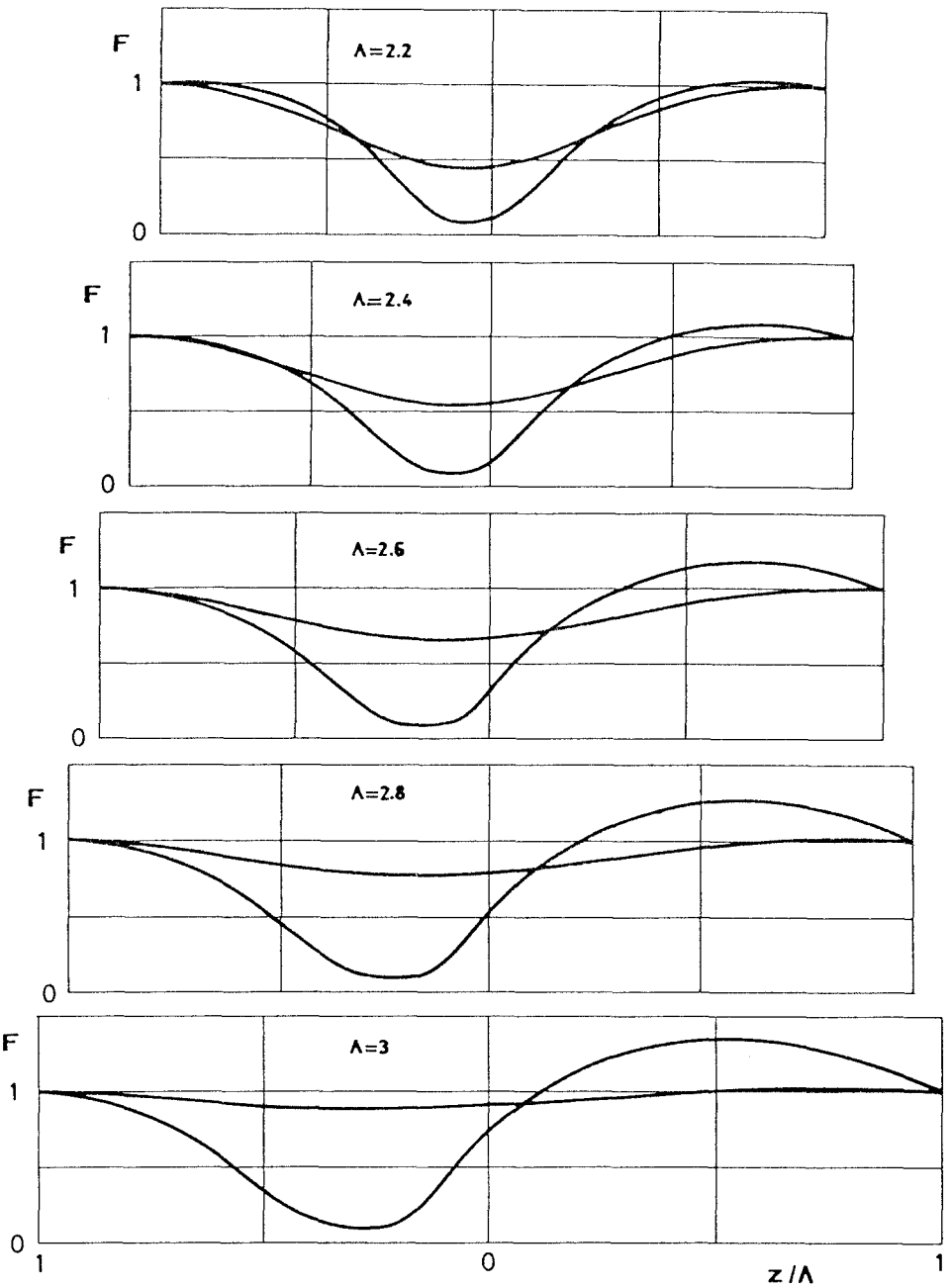

Figure 3. Initial deformed and end-of-computations interface shapes for minimum-volume liquid bridges having different slendernesses, Λ, in the case ε = 0.05.

3. NUMERICAL RESULTS

Although the slice model allows computation of the whole velocity field and the shape of the interface, we only discuss here overall features as breaking time and breaking volume. Breaking time is defined as the time spent by the liquid bridge to reduce the neck from its initial value to zero. Breaking volume is defined as the fraction of the liquid-bridge volume enclosed between one of the disks and the neck of the bridge at breaking time. Owing to numerical stability problems, computations must stop before the zero-neck point is reached. However, the nature of the breaking process makes unnecessary the numerical continuation of the process until the neck bridge vanishes, because close to the breaking point the variation with time of the neck radius and of the volume enclosed between the neck and one of the disks is precisely defined, i.e.: the curves of neck radius and volume-to-neck versus time end with infinite and zero slope, respectively. In computations, the stopping condition has been $S_{min} \leq 0.01$.

In Figure 3 the initial and final computed interface shapes are shown for several values of the slenderness in the case ε = 0.05. In Table 1 the breaking time and breaking volume for configurations having $\Lambda > \Lambda_B$ are summarized. Besides these cases, additional runs for liquid bridges having $\Lambda < \Lambda_B$ have been performed, yielding very small breaking times, so in the following we centered our attention to the more interesting range $\Lambda > \Lambda_B$.

Table 1

	Λ											
	2.2		2.4		2.6		2.8		3.0		π	
ε	t_b	V_p	t_b	V_p	t_b	V_p	t_b	V_p	t_b	V_p	t_b	V_p
0.15	1.16	0.6693	2.62	0.6704	6.13	0.6949	11.64	0.7716	16.02	0.8192	19.06	0.8488
0.12	1.69	0.6404	3.66	0.6430	10.22	0.7156						
0.10	2.15	0.6187	4.79	0.6263	13.04	0.7055	19.37	0.7699	25.06	0.8195	28.98	0.8485
0.08	2.73	0.5966	7.40	0.6175	17.66	0.7117						
0.05	4.18	0.5634	17.65	0.6320	28.83	0.7066	37.66	0.7691	45.59	0.8190	50.96	0.8485
0.03	6.11	0.5401	30.13	0.6328								
0.01	10.70	0.5159										

These numerical results are shown in Figures 4-6. In Figure 4 the variation of the breaking time with the initial deformation is plotted. Breaking time increases as ε decreases, becoming infinite when ε = 0 (that is, no evolution occurs if the initial configuration corresponds to the limit of stability). As can be observed in this figure, the breaking time grows with the slenderness: the behaviour may be explained taking into account geometrical, inertial and capillary-pressure effects. The main reason is that the radius of the neck increases with slenderness (assuming that ε is kept constant) and thence t_b will be greater. Even more, the mass of liquid to be displaced increases and inertial effects, that tend to slow the motion, become more and more important. On the other hand, the forcing actions in the liquid-bridge problem are the capillary-pressure gradients which, roughly speaking, are proportional to the deformation of the interface which, in turn, becomes smoother as Λ increases.

The variation of the breaking volume with the initial deformation is plotted in Figure 5 for several values of the slenderness. As can be observed, if the slenderness is large the breaking volume does not depend on the initial perturbation for the range of values of ε considered. As Λ decreases, numerical results show an increasing dependence on ε. Let us discuss in more detail the case Λ = 2.4 which incorporates all the features of the phenomenom (the same reasoning applies to other values of the slenderness). When the imposed perturbation is large, a thin neck is created in the liquid bridge and the imposed capillary-pressure gradients are so strong that the evolution is determined from the starting time by the imposed disturbance. In this part of the curve the breaking volume is nearly equal to that existing at the beginning between one of the disks and the neck section, and breaking volume varies almost linearly with ε. When the initial deformation is small, the breaking volume happens to be independent of ε or, in other words, the breaking volume becomes an intrinsic characteristic of the breaking process.

Finally, the dependence of the breaking volume on the slenderness is shown in Figure 6. According to this plot, if ε is small enough, the breaking volume varies smoothly with slenderness from 0.85 at Λ = π to 0.5 at Λ = 2.128.

As stated above, in addition to the cases enclosed in Table 1 other runs for liquid bridges having slendernesses below 2.128 have been performed. Calculations show that, provided ε is small enough, these liquid-bridge configurations do not break when subjected to non-symmetrical perturbations like Eq. 6. In constrant, if the perturbations are symmetrical respect to the middle plane, the liquid bridge will break, the breaking volume being 0.5.

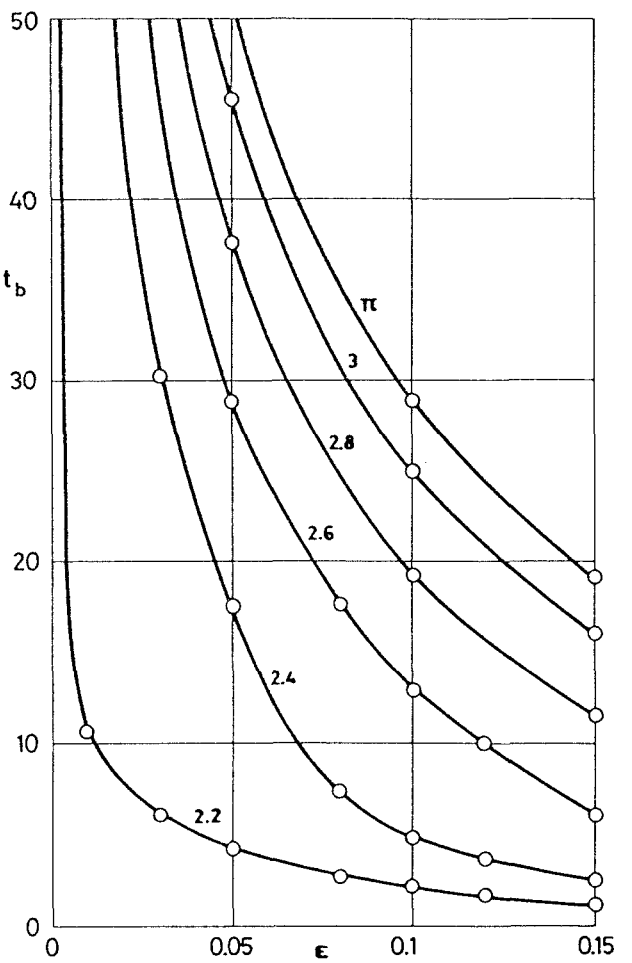

Figure 4. Breaking time, t_b, versus initial deformation, ε, of minimum-volume liquid bridges. Numbers on curves indicate the value of the slenderness, Λ.

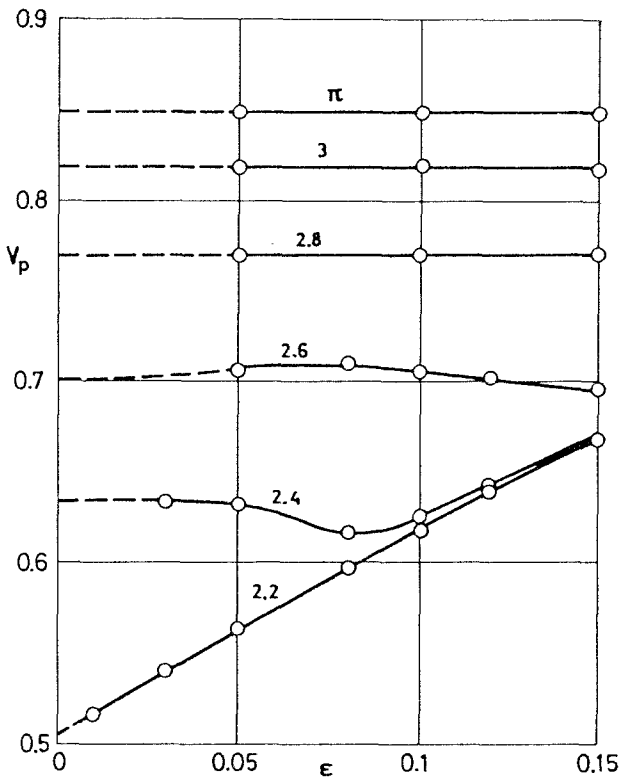

Figure 5. Breaking volume, V_p, versus initial deformation, ε, of minimum-volume liquid bridges. Numbers on curves indicate the value of the slenderness, Λ.

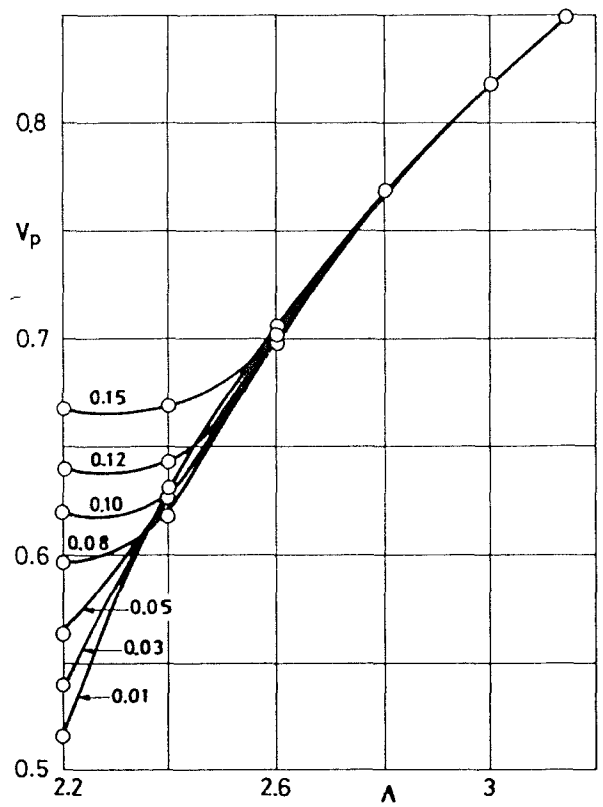

Figure 6. Breaking volume, V_p, versus slenderness, Λ, of minimum-volume liquid bridges. Numbers on curves indicate the value of the initial deformation, ε.

This work has been sponsored by the Spanish Space Reasearch Commission (CONIE).

4. REFERENCES

1. Gillette R D & Dyson D C 1971, Stability of fluid interface of revolution between equal solid circular plates, *Chem. Engng. J.*, 2, 44-54.

2. Martínez I 1978, Hidrostática de la zona flotante, *Tesis Doctoral*, Universidad Politécnica de Madrid.

3. Meseguer J 1983, The breaking of axisymmetric slender liquid bridges, *J. Fluid Mech.* To appear.

4. Sanz A & Martínez I 1983, Minimum volume for a liquid bridge between equal discs, *J. Colloid Interface Sci.* To appear.

5. Lee H C 1974, Drop formation in a liquid jet, *IBM J. Res. Dev.* 18, 364-369.

6. Pimbley W T 1976, Drop formation from a liquid jet: a linear one-dimensional analysis considered as a boundary value problem, *IBM J. Res. Dev.* 20, 148-156.

7. Pimbley W T & Lee H C 1977, Satellite droplet formation in a liquid jet, *IBM J. Res. Dev.* 21, 21-30.

8. Roache P J 1972, *Computational Fluid Dynamics*, Albuquerque, Hermosa Publishers.

9. Mitchell A R & Griffiths D F 1980, *The Finite Difference Method in Partial Differential Equations*, New York, John Wiley & Sons Ltd.

STABILITY OF AXISYMMETRIC LIQUID BRIDGES

I. Martínez

E.T.S.I. Aeronáuticos, Universidad Politécnica de Madrid, Spain

ABSTRACT

A simple formulation and a compact set of graphic data are presented for the equilibrium shapes and stability limits of axisymmetric liquid bridges. The stability analysis is based on the bifurcation of static configurations and gives the minimum liquid volume a bridge can hold, and the breaking mode. The end supports considered are: equal discs, unequal discs, free edge plates and paraboloidal supports.

Keywords: liquid bridge, stability, capillarity, interfaces, microgravity.

1. INTRODUCTION

Small liquid volumes, partially attached to solid boundaries, naturally appear in a variety of applications, and some basic phenomena as capillary hysteresis are not yet fully understood. Levitation of large samples under reduced gravity, allows for a more detailed analysis to be performed, while orbiting platforms as Spacelab promise to provide the appropriate environment.

In this frame, this paper presents some theoretical results on the stability limits, what seems to be of great value in the undestanding of other, less easily controlled, phenomena.

The modelling is quite simple: only equilibrium shapes are considered, satisfying Laplace equation of capillary pressure, that, in a dimensionless form, reads

$$K+P+Wr^2/2-Bz=0 \qquad (1)$$

K being the local mean curvature at a point in the interface, P a constant related to the origin of pressures, W the imposed rotation Weber number, B the imposed Bond number due to a residual microgravity, and r and z the radial and axial coordinates. Explicit expressions for W and B will depend on the length chosen to nondimensionalize.

Two integration constants from the second order differential operator K, plus the constant P are to be substituted by the three imposed boundary conditions: one at the solid contact at each end of the bridge, and the volume of liquid, which is supposed to be controlled.

Two different simplifying boundary conditions are considered (Figure 1): fixed end-points (liquid borders anchored at a sharp solid edge) and free end-points with fixed contact angle; the latter seems the less controllable assumption in practice.

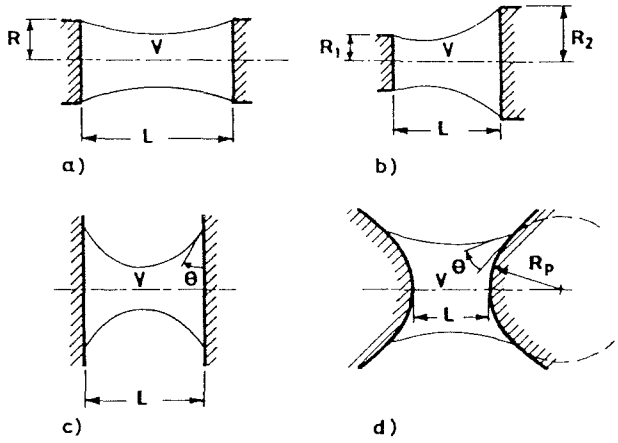

Figure 1. Bridge geometries considered: a) equal discs, b) unequal discs, c) free edge plates, d) paraboloidal supports.

Equilibrium shapes for axisymmetric bridges when W=B=0 are pieces of Plateau's constant-curvature surfaces of revolution, what greatly reduces the effort to find the stability limit that here is just performed by plotting every possible equilibrium point in a volume-slenderness diagram and checking for the free energy of similar points to be a minimum (further insight is to be gained from the different cases described below in detail).

2. EQUAL DISCS

The disc radius R is taken as unit length and thus $W=\rho\Omega^2R^3/\sigma$ and $B=\rho gR^2/\sigma$ in Eq. 1. Two additional nondimensional variables are introduced: the slenderness of the bridge $\Lambda=L/(2R)$ and the volume v=

Proceedings of the 4th European Symposium on Materials Sciences under Microgravity, *Madrid, Spain*, 5-8 *April* 1983 (*ESA SP-191 – June* 1983).

V/R^3. The configuration is determined by the disc radius R, their separation L, and the volume V of liquid (see Figure 1a), and the relevant fluid properties are the density difference ρ and the interface tension σ with the surrounding fluid (a gaseous atmosphere or an outer liquid as in the Plateau tank technique).

In absence of rotation and gravity, i.e. for W=B=0, with $v=2\pi\Lambda$, the trivial solution of a cylindrical shape takes place, being stable when $0\le\Lambda\le\pi$ as already known for more than a century. The cylinder is also the stable shape when a solid body rotation $W\neq 0$ exists, provided a combination $f(\Lambda,W)=0$ is not exceeded; the exact expression for f was given in Ref. 1 and approaches $\Lambda=\pi(1-W/2)$ for small W.

When an axial microgravity is present, i.e. for $B\ll 1$ with W=0 and $v=2\pi\Lambda$, the cylinder r=1 is no longer an equilibrium shape, deforming to (Ref. 2)

$$r = 1 + B\left(\frac{1}{\sin\Lambda} - \frac{\pi}{2\Lambda}\right)\sin\frac{\pi z}{\Lambda} \qquad 0\le z\le 2\Lambda \quad (2)$$

with a limit of stability $\Lambda=\pi\left[1-(9B/4)^{3/2}\right]$ for small B, given in Ref. 3.

The whole volume-separation stability diagram in the absence of rotation and gravity was presented in Ref. 4, but if only slight volume departures from that of a cylinder are envisaged, i.e. for W=B=0 with $v-2\pi\Lambda\ll 1$, the combination $f(\Lambda,v)$ bounding the stability region can be approximated to $\Lambda=\pi\left[1+(v-2\pi\Lambda)/4\right]$; this excess in volume forces the cylinder r=1 to deform to (Ref. 2)

$$r = 1 + \frac{v-2\pi\Lambda}{2\pi\Lambda}\,\frac{1-\cos\Lambda}{4\sin\Lambda-2\cos\Lambda}\,\sin\frac{\pi z}{2\Lambda} \qquad 0\le z\le 2\Lambda \quad (3)$$

On the other hand, if an initial deformation is imposed on the cylinder in the case W=B=0 with $v=2\pi\Lambda$, a dynamical evolution will follow, except in the limiting case it coincides with the unstable equilibrium shapes described in Ref. 2 (Figure 2) that can be approximated by

$$r^2 = 1 + \left[\frac{4}{\sqrt{3}}\,\lambda^{1/2}(1-\lambda)\right]\sin\frac{\pi z}{\Lambda} \qquad 0\le z\le 2\Lambda \quad (4)$$

where $\lambda=1-\Lambda/\pi$. The square of r is used to extend the range of validity of Eq. 4 since it fully satisfies the v=const constraint for any Λ.

In conclusion, the influence of the above perturbations on the well-known stability limit $\Lambda=\pi$ for a cylindrical bridge anchored at its edges is best visualized by the reduction they impose on the maximum attainable slenderness

$$\Lambda_{max} = \pi\left[1 - \frac{W}{2} - \left(\frac{9}{4}B\right)^{3/2} - \frac{3}{16}a^2 + \frac{v-2\pi\Lambda}{4\pi}\right] \quad (5)$$

where a stands for the amplitude of a sinusoidal perturbation. Although Eq. 5 is just a linear approximation, it is worth noticing that the exact dependence on all the mentioned effects, assumed isolated, is known (Refs. 2 and 5). Further results concerning the celebrated C-mode rotational instability that may arise for $\Lambda<\sqrt{3}\pi/2$ can be found in Ref. 3.

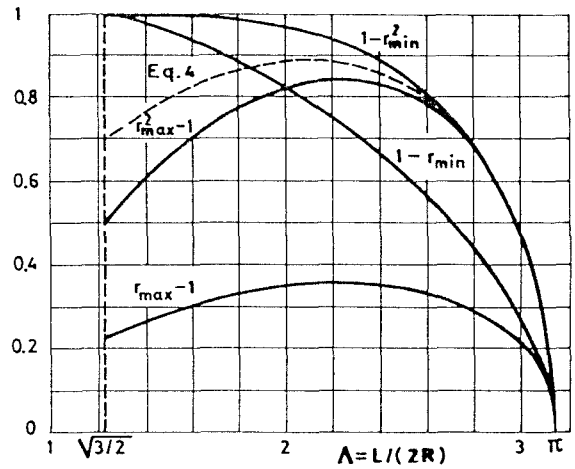

Figure 2. Extremal deviations from the cylinder r=1 corresponding to unstable equilibrium shapes of cylindrical volume $v=2\pi\Lambda$. Both the maximum and the minimum for the radius r and the cross-section r^2 are plotted versus the bridge slenderness Λ. The dashed line correspond to the approximation of Eq. 4.

3. UNEQUAL DISCS

Let w be the diameter ratio of the smaller to the larger diameter disc (Figure 1b); w=1 recovers the analysis for equal discs. The shape of the bridge r=r(z) can best be described (in an internal coordinate system used for Plateau's curves) as $r=r(\alpha,\phi)$ and $z=z(\alpha,\phi)$, where α measures the curvature characterizing the curve, and ϕ serves to generate points along it. With the origin in a maximum and its ordinate as unit length, the expressions for the curve points (r,z), the slope angle γ, and the volume v and surface area s up to this section are given by:

$$\left.\begin{aligned} r(\alpha,\phi) &= \sqrt{1-\sin^2\alpha\sin^2\phi} \\ z(\alpha,\phi) &= \cos\alpha\,\Gamma(\alpha,\phi) + E(\alpha,\phi) \\ |\gamma(\alpha,\phi)| &= \arccos\frac{r+\cos\alpha/r}{1+\cos\alpha} \\ v(\alpha,\phi) &= \frac{\pi}{3}\left[r\sqrt{(1-r^2)(r^2-\cos^2\alpha)} - \right. \\ &\qquad \left. - z\cos\alpha + 2(1+\cos\alpha)^2 E(\alpha,\phi)\right] \\ s(\alpha,\phi) &= 2\pi(1+\cos\alpha)E(\alpha,\phi) \end{aligned}\right\} \quad (6)$$

where Γ and E are the alliptic integrals of the first and second class. The only Plateau curve not included in this formulation is the catenoid, but its study is much simple.

The aim is to know which of the several possible equilibrium shapes is the stable one (in some neighbourhood), for predefined values of R_1, R_2, L and V (radius of the discs, disc separation and liquid volume). The procedure is as follows; once $w=R_1/R_2$ fixed, a bidimensional scan in α and ϕ allows to compute the dimensionless parameters

$$\frac{L}{R_1+R_2} = \frac{z(\alpha,\phi')-z(\alpha,\phi)}{r(\alpha,\phi')+r(\alpha,\phi)} \qquad (7)$$

$$\frac{V}{(R_1+R_2)^3} = \frac{v(\alpha,\phi')-v(\alpha,\phi)}{[r(\alpha,\phi')+r(\alpha,\phi)]^3} \qquad (8)$$

$$\frac{S}{(R_1+R_2)^2} = \frac{s(\alpha,\phi')-s(\alpha,\phi)}{[r(\alpha,\phi')+r(\alpha,\phi)]^2} \qquad (9)$$

with ϕ' given by the constrain in the disc-diameter ratio w

$$w = \frac{\sqrt{1-\sin^2\alpha\sin^2\phi'}}{\sqrt{1-\sin^2\alpha\sin^2\phi}} \qquad (10)$$

If then $V/(R_1+R_2)^3$ is plotted versus $L/(R_1+R_2)$ as Figure 3 shows for w=0.99, a minimum-volume curve appears. Figure 4 is a summary of this stability limit, the most important from the practical point of view, for different disc-diameter ratios w (upper volume limits are dealt with in the same way).

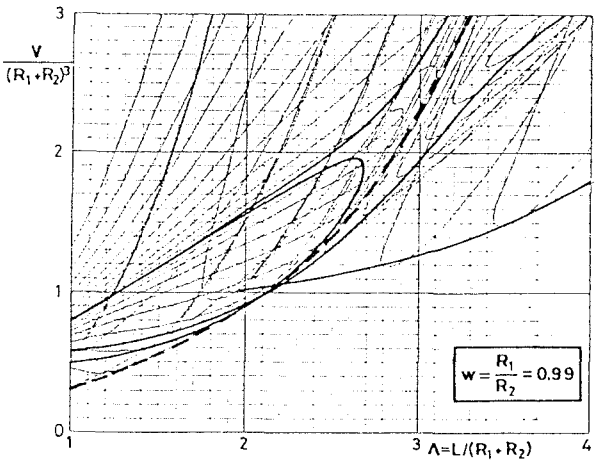

Figure 3. Volume-separation diagram for disc-diameter ratio w=0.99. Thin lines correspond to different Plateau curves (α=const). Thick lines correspond to bridges with one angle at the disc edge equal to π/2. The dashed line is the stability limit.

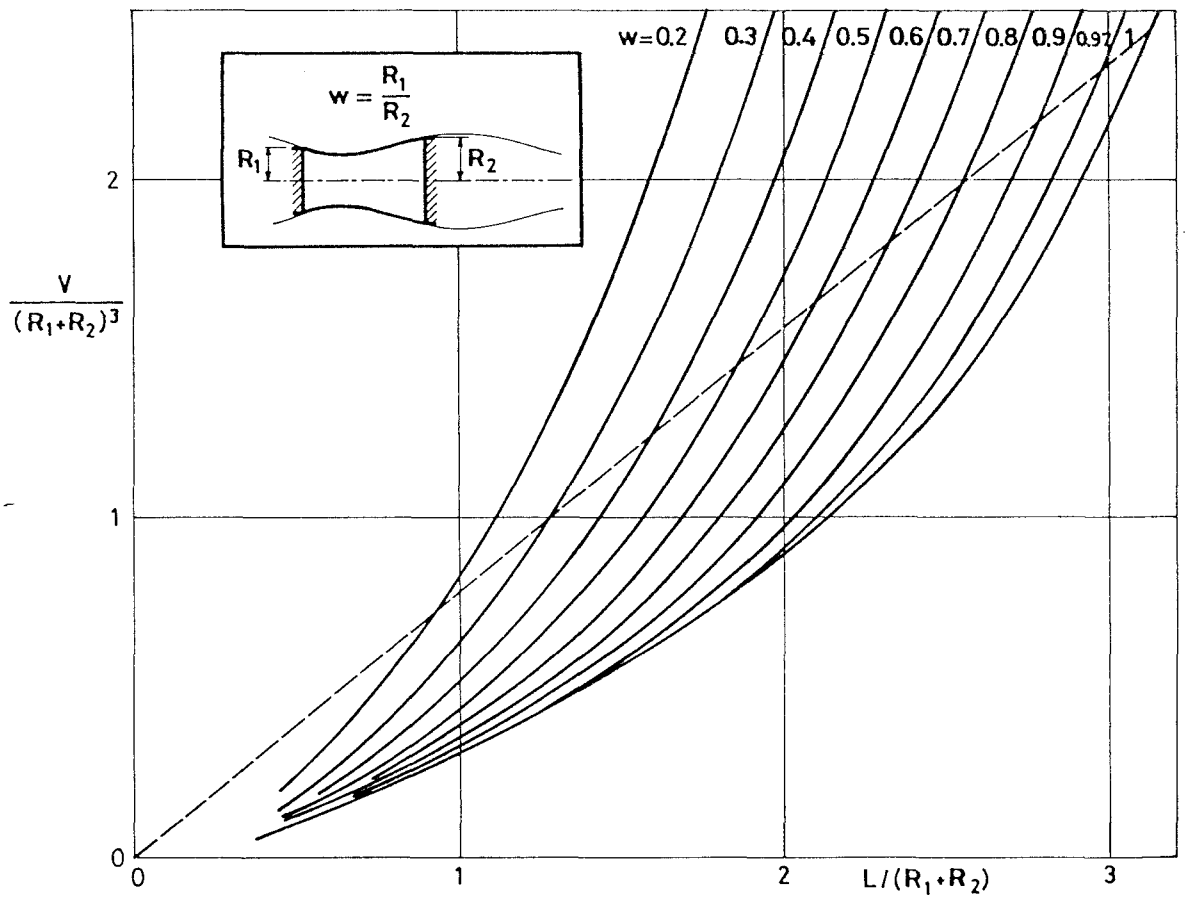

Figure 4. Stability limits for several disc-diameter ratios w, showing the minimum liquid volume for a bridge of span L. Dashed line corresponds to "cylindrical" configurations, i.e. $v=\pi(R_1+R_2)^2L/4$.

Normally, the local minimum in the volume will be the stability limit, but to verify that, (α,ϕ) couples of constant $L/(R_1+R_2)$ can be selected from the volume-separation diagram and its interface area $S/(R_1+R_2)^2$, equal to the nondimensional free energy of the system, plotted versus $V/(R_1+R_2)^3$. The true stability limit will become apparent, as shown in Figure 5, where the above-mentioned procedure has been followed for two cases, $\Lambda=1.5$ and $\Lambda=2.5$, with $w=0.99$ to compare with Figure 4.

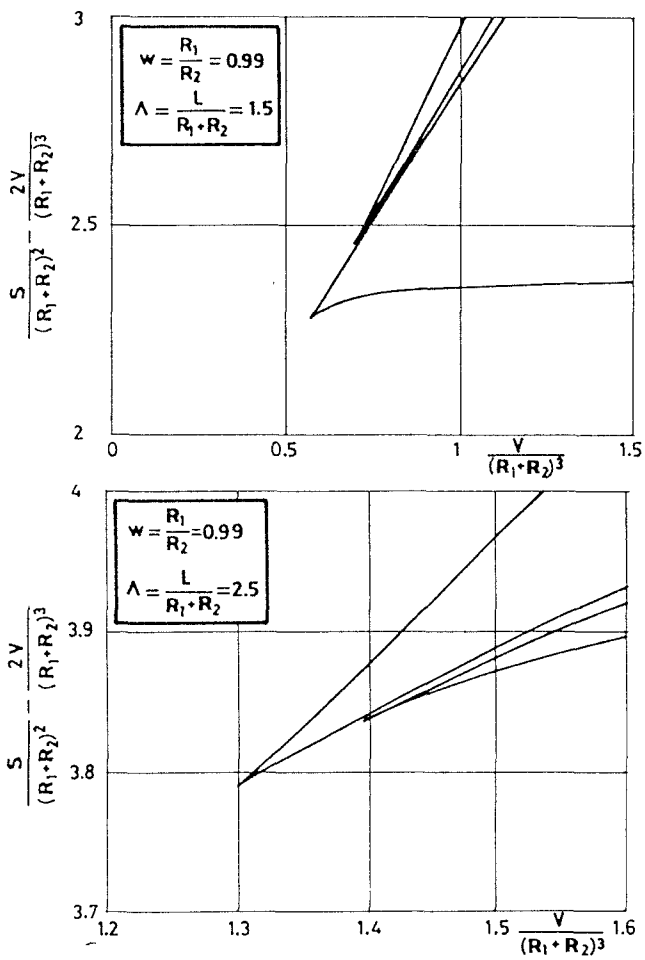

Figure 5. Free energy (interface area) S of a liquid bridge between discs of diameter-ratio w=0.99 versus volume V, for a constant separation Λ. The shift on the ordinates is just to enhance the graphic.

Other conclussions to be drawn from the analysis of unequal-disc configurations are that short bridges break with angles at both edges below $\pi/2$ whereas long bridges do it with one below and the other above $\pi/2$. Moreover, the breaking neck always forms near the smaller disc (it remains indeterminated with equal discs). Finally, edge dettachment for short bridges when decreasing the volume always take place at the larger disc.

Most of the above results can be easily understood if comparison is made with the equal-disc case in the special case $V=\pi L(R_1+R_2)^2/4$, corresponding to the cylindrical evolution $V=\pi R^2 L$ for equal discs. The bifurcation pattern is sketched in Figure 6

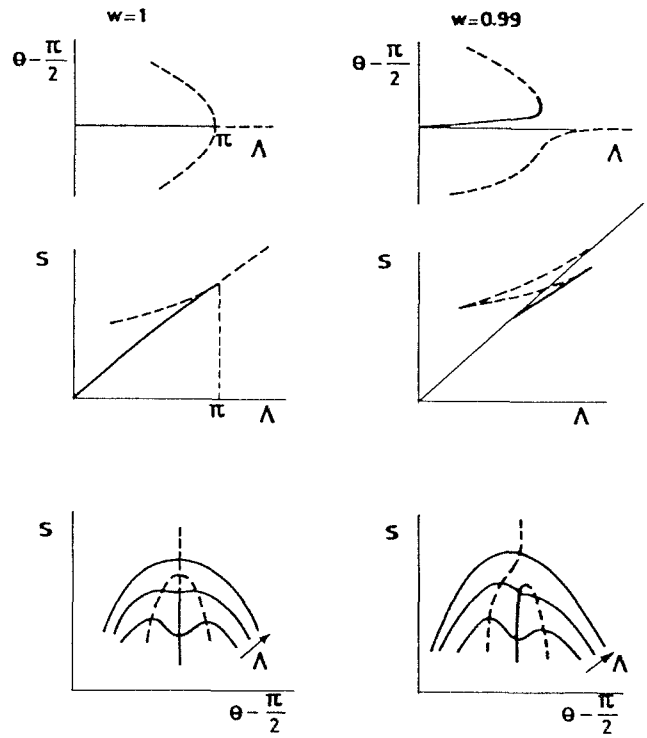

Figure 6. Comparison of the bifurcation at the stability limit for "cylindrical" bridges $(V=\pi L(R_1+R_2)^2/4)$ between equal discs w=1 and unequal discs of diameter ratio w=0.99.

where the angle with the larger disc is taken as bifurcating variable. In some respect, this effect is similar to that of a small axial gravity for equal discs (the role of the bottom disc is here played by the smaller disc).

Finally, the difference in the bifurcation pattern at constant disc separation is illustrated in Figure 7, where the unstable symmetrical cusp found for $\Lambda>2.13$ with equal discs is seen to yield a new local minimum in the volume.

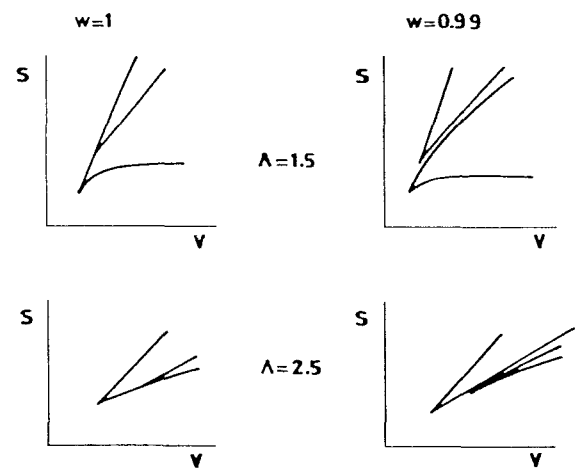

Figure 7. Free energy versus volume, showing the effect of a small difference in the diameter of the discs for constant disc separation $\Lambda=1.5$ and $\Lambda=2.5$.

4. FREE EDGE PLATES

The quasi-static modelling of a three phase line (at the intersection of the fluid-fluid interface with the solid boundary) as a constant contact-angle border seems rather poor and far from experimental evidence, but because of its simplicity it is a common assumption and will be followed here.

Using the only available length L as unity, the geometry rests specified in practice by giving the contact angle θ and the nondimensional volume V/L^3 (see Figure 1c). Since θ is the complementary of the slope angle γ given in Eq. 6, and due to its simple dependence on α and ϕ (not involving elliptical integrals) the procedure, though similar to that explained for unequal discs, can be carried out in a straightforward manner.

For a given θ, the maximum $\alpha \in (-\pi, 0)$ that can accomodate such a bridge is $\alpha_m = -2\,\mathrm{arctg}\sqrt{\cos\theta}$, thus a simple scan on α is enough to draw the $(S/L^2,\ V/L^3)$ plot from which the stability limit is found. Notice that now S represents the effective interface area, $S = S_{liq\text{-}gas} - S_{liq\text{-}sol}\cos\theta$, coincident (in nondimensional variables) with the free energy of the system. This has been carried out in Figure 8 for two contact angles: 10 and 45 degrees.

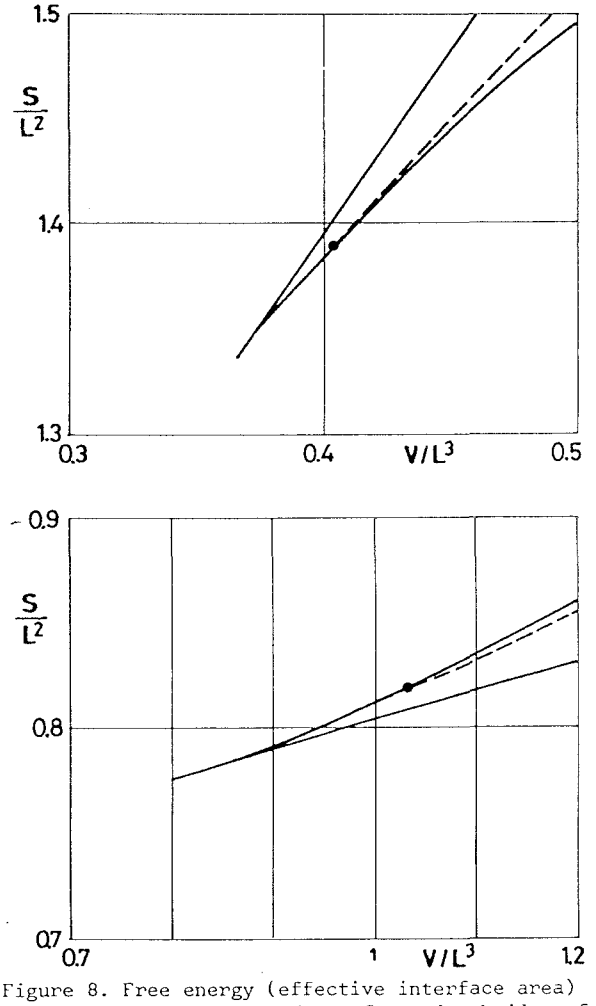

Figure 8. Free energy (effective interface area) versus volume for a free-edge bridge of constant contact angle θ. Dashed line corresponds to asymmetric shapes relative to the mid-plane between discs.

The procedure is as follows: the radius for the known θ and selected α is computed from

$$r = a\left(1 \pm \sqrt{1-\cos\alpha/a^2}\right) \quad \text{where } a = \frac{\sin\theta(1+\cos\alpha)}{2} \tag{11}$$

(there are two solutions). After that, the corresponding ϕ that defines the point in the Plateau curve is computed from

$$\phi = \text{arc tg}\sqrt{\frac{1-r^2}{r^2-\cos^2\alpha}} \tag{12}$$

(one for each of the two r's in Eq. 11). Once (α,ϕ) known, the V/L^3-S/L^2 diagram can be computed by means of

$$\frac{V}{L^3} = \frac{v(\alpha,\phi')-v(\alpha,\phi)}{[z(\alpha,\phi')-z(\alpha,\phi)]^3}$$

$$\frac{S}{L^2} = \frac{s(\alpha,\phi')-s(\alpha,\phi)}{[z(\alpha,\phi')-z(\alpha,\phi)]^2} \tag{13}$$

where r, z, v and s are given by Eq. 6 and ϕ' is related to the ϕ given by Eq. 12 in the following way: $\phi' = \phi$ for bulged bridges, $\phi' = -\phi$ for depleted shapes and ϕ' equal to the other value given by Eq. 12 when Eq. 11 is used accordingly (it corresponds to asymmetric bridges).

The limit of stability, i.e. the minimum volume for a stable bridge, is summarized in Figure 9 versus contact angle. The salient features are the minimum volume for $\theta=0$ ($V/L^3=0.98$), that of a catenoidal breakage (that occurs with $\theta=15°$ and $V/L^3=0.77$), that of a cylindrical breakage (that occurs with $\theta=\pi/2$ and $V/L^3=1/\pi$, corresponding to $L=\pi R$ as shown in Ref. 5) and the fact that bridge rupture is symmetric for $\theta<31.1°$, forming two equal drops, and asymmetric for $\theta>31.1°$, in a similar way as with anchored edges to equal discs.

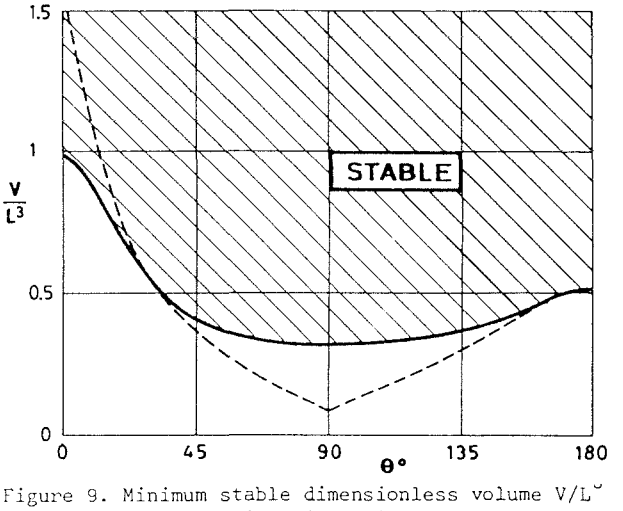

Figure 9. Minimum stable dimensionless volume V/L^3 for a liquid bridge with constant contact angle θ (see Figure 1c).

However, quasi-static evolutions are best followed in Figure 10, where shape variation when liquid is injected or removed is apparent.

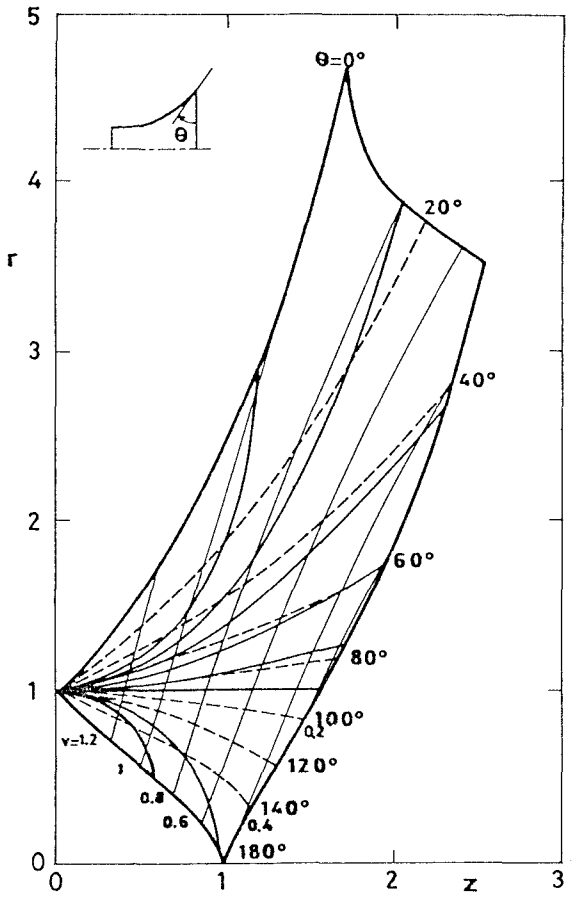

Figure 10. Stability diagram for shapes with constant contact angle θ. For a given θ and a volume $v=V/L^3$, the corresponding thin line gives half of the shape, as shown in the insert. Moving down lines with θ=const, succesives shapes following liquid injection or removal are visualized.

5. PARABOLOIDAL SUPPORTS

An interesting extension of the free-edge problem presented above is to consider curved end-plates as a model for liquid bridges formed in poorly soaked porous media. Convex paraboloidal supports have been included as the easiest approach. In this context, the geometry is specified given the vertex radius R_p of the paraboloids (Figure 1d), the separation L between vertices, the contact angle θ of the interface at the solid boundary and the volume V of liquid. Since θ and R_p are assumed to be fixed, the only two dimensionless parameters to be controlled are L/R_p and V/R_p^3 and, as before, the aim is to work out the stability limit.

As above, the interface shape is best described in terms of the internal variables (α,ϕ) of Plateau's curves (Eq. 6). In that scale the vertex radius r_p of the paraboloid is

$$r_p(\alpha,\phi) = r(\alpha,\phi)\,tg[\theta-\gamma(\alpha,\phi)] \qquad (14)$$

where r and γ are given by Eq. 6. The expression for L/R_p, V/R_p^3 and S/R_p^2 in this case take the form

$$\left.\begin{aligned}
\frac{L}{R_p} &= \frac{z(\alpha,\phi')-z(\alpha,\phi)}{r_p(\alpha,\phi)} - \frac{r^2(\alpha,\phi')+r^2(\alpha,\phi)}{2r_p^2(\alpha,\phi)} \\
\frac{V}{R_p^3} &= \frac{v(\alpha,\phi')-v(\alpha,\phi)}{r_p^3(\alpha,\phi)} - \frac{\pi[r^4(\alpha,\phi')+r^4(\alpha,\phi)]}{4r_p^4(\alpha,\phi)} \\
\frac{S}{R_p^2} &= \frac{s(\alpha,\phi')-s(\alpha,\phi)}{r_p^2(\alpha,\phi)} - \frac{2\pi}{3}\left[\left(1+\frac{r^2(\alpha,\phi')}{r_p^2(\alpha,\phi)}\right)^{3/2} + \right. \\
&\qquad \left. + \left(1+\frac{r^2(\alpha,\phi)}{r_p^2(\alpha,\phi)}\right)^{3/2} - 2\right]
\end{aligned}\right\} \qquad (15)$$

where last terms account for the effect of the immersed tip of paraboloids.

Following the same procedure detailed above for unequal discs, the following results have been obtained. Long bridges break in an asymmetric way when the shape approaches a complete period of Plateau's curves, being it applicable to liquids with large (say θ>45°) contact angles to the solid supports. In particular, cylindrical zones, formed when the liquid volume is the appropriate for the interface to reach the point where the paraboloidal shape matches the contact angle, break at $L=2\pi R$, though the volume is less than $\pi R^2 L$ due to the protruding paraboloidal tips (line a in Figure 11). Short zones, normally found with small contact angles, break in a symmetric way. The stability limits for configurations with contact angle 30°, 60° or 90° are drawn in Figure 11, where point A, separating symmetric breakage (for $L<L_A$) from asymmetric one ($L>L_A$) is seen in the case of 60°; for 30°it is beyond the limits shown, and for 90°it shifts to the origin.

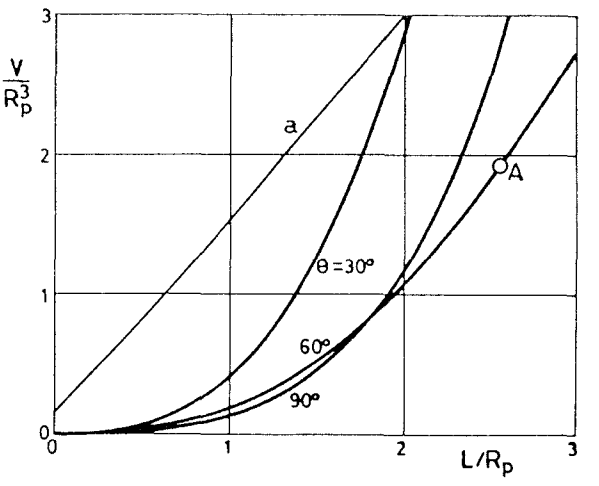

Figure 11. Stability limits for liquid bridges with constant contact-angle θ between paraboloidal supports. For θ=60° line a corresponds to cylindrical shapes, separating the upper region of bulged shapes from the lower one of spindled shapes. Point A separates symmetric (below) and asymmetric (above) modes of breaking.

6. CONCLUSIONS

The first step in the understanding of fluid-interface behaviour is to locate the interface shape, performing equilibrium and stability analysis, what has been done here for some interesting bridge configurations. As a general conclusion, long zones loose their stability through an asymmetric mode and yield two distinct drops, whereas short zones tend to neck in a symmetric way and yield similar drops. As expected, imperfections imposed to equal-disc bridges introduce deviations in the behaviour of such bridges that have very similar consequences: reduction of the stability limits, bias in the otherwise symmetric structure, etc.

When the bridge has not its borders anchored to sharp solid edges, the stability limits reduce nearly to a half (in achievable slenderness, for instance). Practical problems associated with the advancing and receding contact lines, however, seem to put in question the validity of results for free-contact-line bridges.

This work has been sponsored by the Spanish Commission for Space Research (CONIE).

1. Martínez I 1978, Floating zone: equilibrium shapes and stability criteria, *COSPAR Space Research* XVIII, 519-522.

2. Martínez I 1978, Hidrostática de la zona flotante, *Tesis Doctoral*, Universidad Politécnica de Madrid.

3. Vega J M & Perales J M 1983, Almost-cylindrical isorotating liquid bridges for small Bond numbers, in *ESA SP-191*.

4. Da Riva I & Martínez I 1979, Floating zone stability (Exp. 1-ES-331), *ESA SP-142*, 67-74.

5. Boucher E A & Evans M J B 1980, Properties of fluid bridges between solids in a gravitational field, *J. Colloid Interf. Sci.*, 75, 409-418.

6. Martínez I 1976, Floating zone under reduced gravity: axisymmetric equilibrium shapes, *ESA SP-114*, 277-282.

TANQUE PARA EXPERIMENTACION CON PUENTES LIQUIDOS EN CUALQUIER ORIENTACION

1. Introducción

La idea de construir un aparato que permita el manejo de zonas líquidas cuyo eje de simetría tuviese cualquier posición con respecto a la dirección del campo gravitatorio terrestre, y no únicamente restringido a posiciones próximas a la vertical, surge cuando se hace patente la necesidad de realizar la simulación en tierra del manejo del puente líquido en el interior de la cámara de ensayos del Módulo de Física de Fluidos (Fluid Physics Module, FPM), simulación de gran ayuda tanto para el entrenamiento de los especialistas de vuelo, como para los propios experimentadores a los que podría poner de manifiesto más directamente las relevantes capacidades que el FPM posee, así como las inevitables restricciones, todo ello de la máxima utilidad a la hora de diseñar un experimento.

Esta simulación sería de indudable interés para poner a disposición de la comunidad científica, sobre todo de los posibles usuarios no familiarizados con el FPM, un medio directo de manejo de líquidos en microgravedad simulada en tierra en el seno de un aparato tan sofisticado como el FPM y les daría la oportunidad de una rápida comprensión de los problemas involucrados en el uso del FPM.

Pero además, otra razón fundamental para el desarrollo de este aparato es la de disponer en nuestro laboratorio de la posibilidad de experimentar con zonas cuyo eje de simetría sea no vertical con el fin de investigar la influencia de una microgravedad cuya dirección sea distinta de la axial, como en realidad ocurrirá en los experimentos que se realicen en un laboratorio espacial.

El hecho de que exista una microgravedad no axial abre un campo de investigación teórica nuevo al no poderse seguir manteniendo la hipótesis de axilsimetría, lo que da lugar a un conjunto de problemas de una gran complejidad. Los resultados experimentales obtenidos por otros investigadores en el caso de la estabilidad de puentes líquidos horizontales (Coriell et al. 1977) adelantan el interés que tienen este tipo de configuraciones.

Para responder a las necesidades apuntadas se ha diseñado y construido en el laboratorio un aparato (PT2) que afronte este doble fin. Por un lado, que sea compatible con las rígidas especificaciones impuestas para su instalación en la cámara de ensayos del FPM (ausencia de contacto con cualquier tipo de líquidos, limitaciones obvias de espacio, transmisión de los movimientos de los discos del FPM a los del aparato en cuestión, etc.), y por otro lado, que también sea compatible con los aparatos ya existentes, como por ejemplo el PTF (ya descrito en otros informes) para poder ser utilizado en este laboratorio.

2. Descripción

Con el objeto de poner de relieve las primeras limitaciones que aparecen en el diseño del PT2, en la Fig. 1 se muestra un esquema de la instalación proyectada para poder realizar la formación de puentes líquidos en microgravedad simulada directamente, en el interior de la cámara de ensayo del FPM, cuando éste se encuentra instalado en el Material Science Double Rack (MSDR), en la configuración empleada en vuelo, posición que es indudablemente la más conveniente desde el punto de vista del entrenamiento de los astronautas, y por otra parte, la que más restricciones impone en el diseño del PT2. El montaje en un entorno con menos requisitos obviamente es me

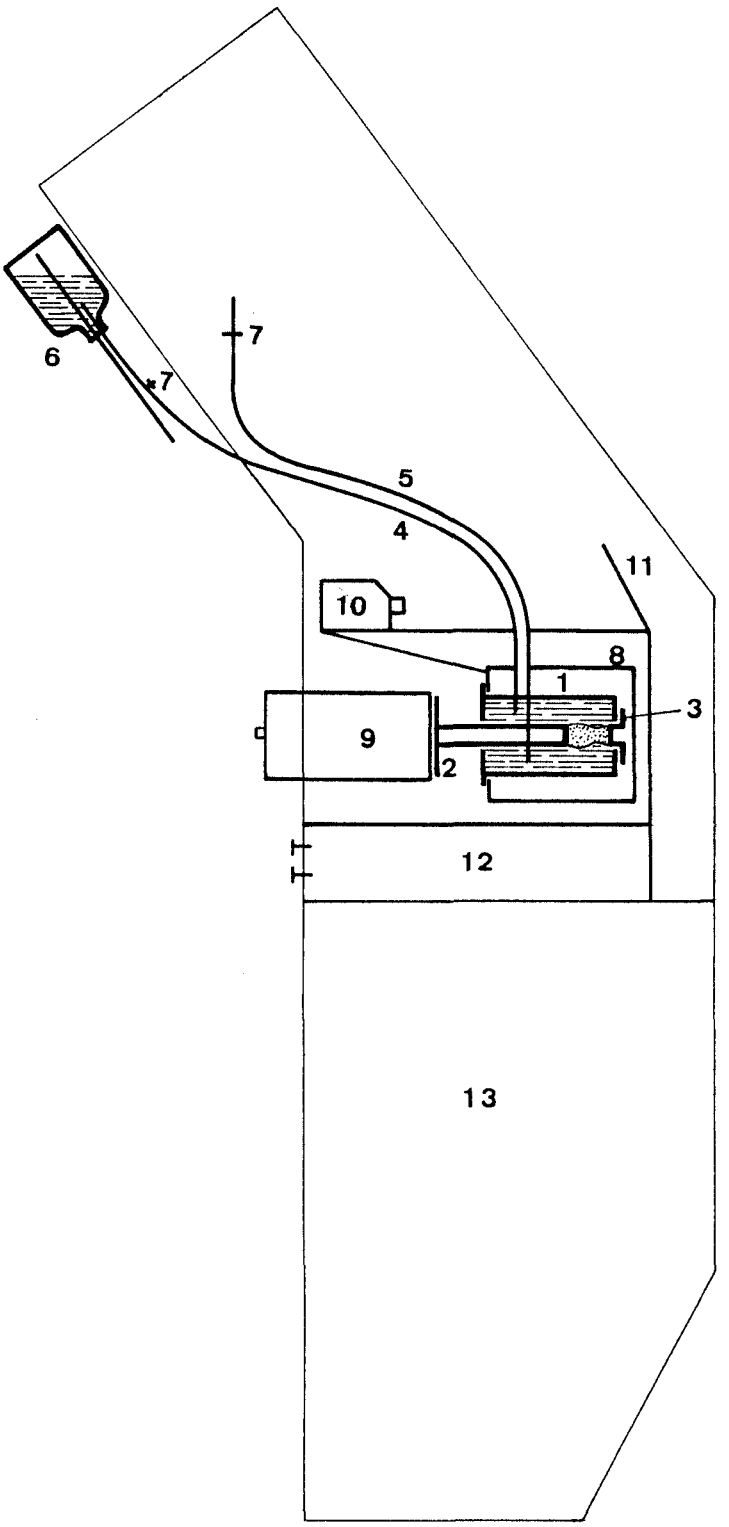

Fig. 1. Esquema de la instalación del PT2 dentro del FPM, montado a su vez en el MSDR. 1, tanque (PT2); 2, adaptador del disco de inyección (FPA); 3, adaptador del disco opuesto (RPA); 4, conducto de alimentación de líquido del baño; 5, conducto de purga; 6, depósito de líquido del baño (BR); 7, válvulas; 8, cámara de ensayos del FPM; 9, cilindro soporte del disco de inyección del FPM; 10, cámara de cine del FPM; 11, espejo; 12, FPM; 13, MSDR.

nos crítico en lo concerniente al diseño por lo que se usará el montaje del PT2 en el FPM situado en el MSDR para ilustrar una configuración genérica, bien entendido que en otros casos podría ser más sencillo, y que la posición horizontal del puente líquido es un requisito del conjunto FPM-MSDR pero que no compromete en modo alguno su uso en otra orientación, aprovechando la versátil maniobrabilidad del PTF, que permite la disposición de los restantes componentes de la instalación (sistemas de iluminación, captación de imágenes, etc.) sin problemas adicionales.

En las Figs. 2, 3 y 4 se muestran el PT2 y los elementos auxiliares desarrollados para adaptarlo al FPM.

El PT2 es un tanque rectangular de cuyas paredes laterales tres son de vidrio transparente y una de metacrilato, la cual, junto con las paredes anterior y posterior (también de metacrilato), proporcionan la necesaria rigidez al conjunto. Las dimensiones que se muestran en las figuras correspondientes, son las máximas compatibles con el tamaño de la cámara de ensayos del FPM. Las paredes anterior y posterior disponen de sendos orificios por los que se realizan los desplazamientos de los soportes de los discos. Dichos orificios están provistos de juntas de estanqueidad que impiden que el líquido del baño salga del tanque y moje las paredes de la cámara del FPM. Una vista de dicho tanque se muestra en la Fig. 2. La pared anterior o frontal tiene forma circular para facilitar la sujeción del tanque a los bordes de orificio existente en la pared de la cámara de ensayo del FPM por el que en condiciones normales se introduciría el cilindro soporte del disco de inyección (ver Figs. 1 y 3). Cuando está montado el tanque no presenta ninguna comunicación libre con el ambiente exterior, razón por la que puede disponerse en cualquier orientación sin que se produzca la pérdida de líquido

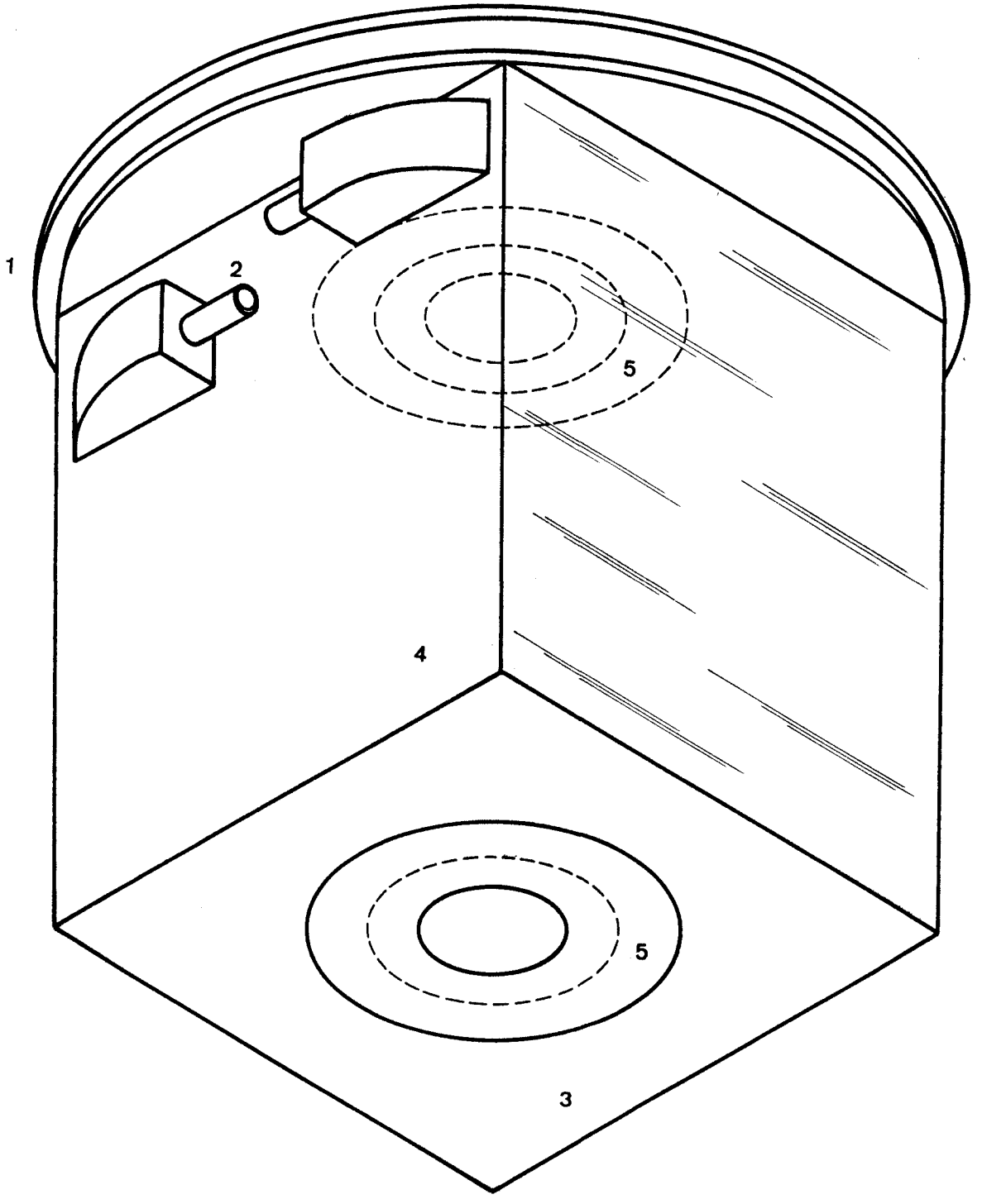

Fig. 2. Tanque que contiene el baño. 1, pared frontal; 2, orificios de alimentación del líquido del baño; 3, pared opuesta; 4, pared lateral de metacrilato; 5, juntas.

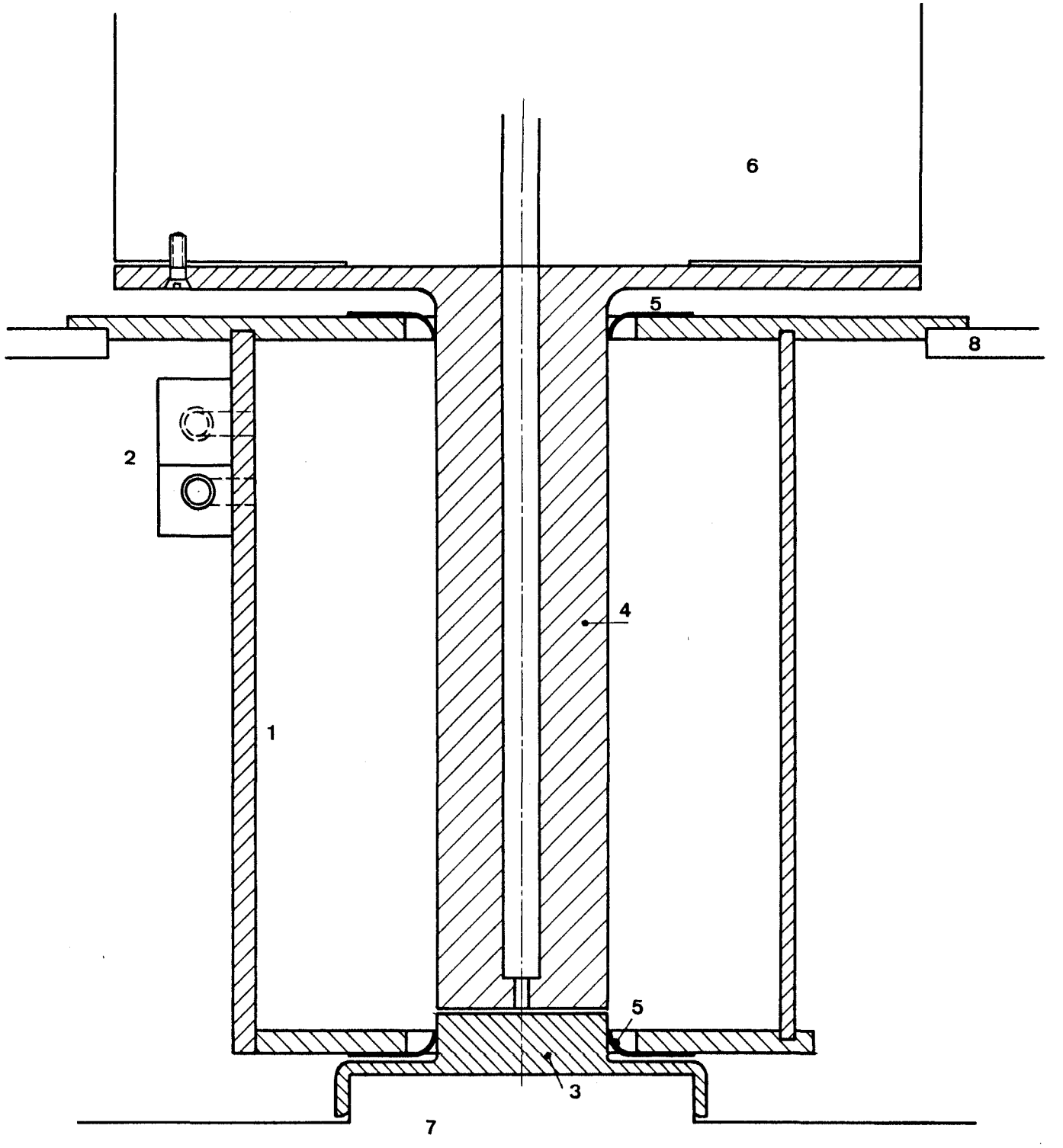

Fig. 3. Vista en sección del PT2 (partes rayadas) montado en la cámara de ensayo del FPM. 1, tanque; 2, orificios de alimentación del líquido del baño; 3, adaptador del disco opuesto (RPA); 4, adaptador del disco de inyección; 5, junta; 6, cilindro soporte del disco de inyección; 7, disco opuesto; 8, paredes de la cámara de ensayo.

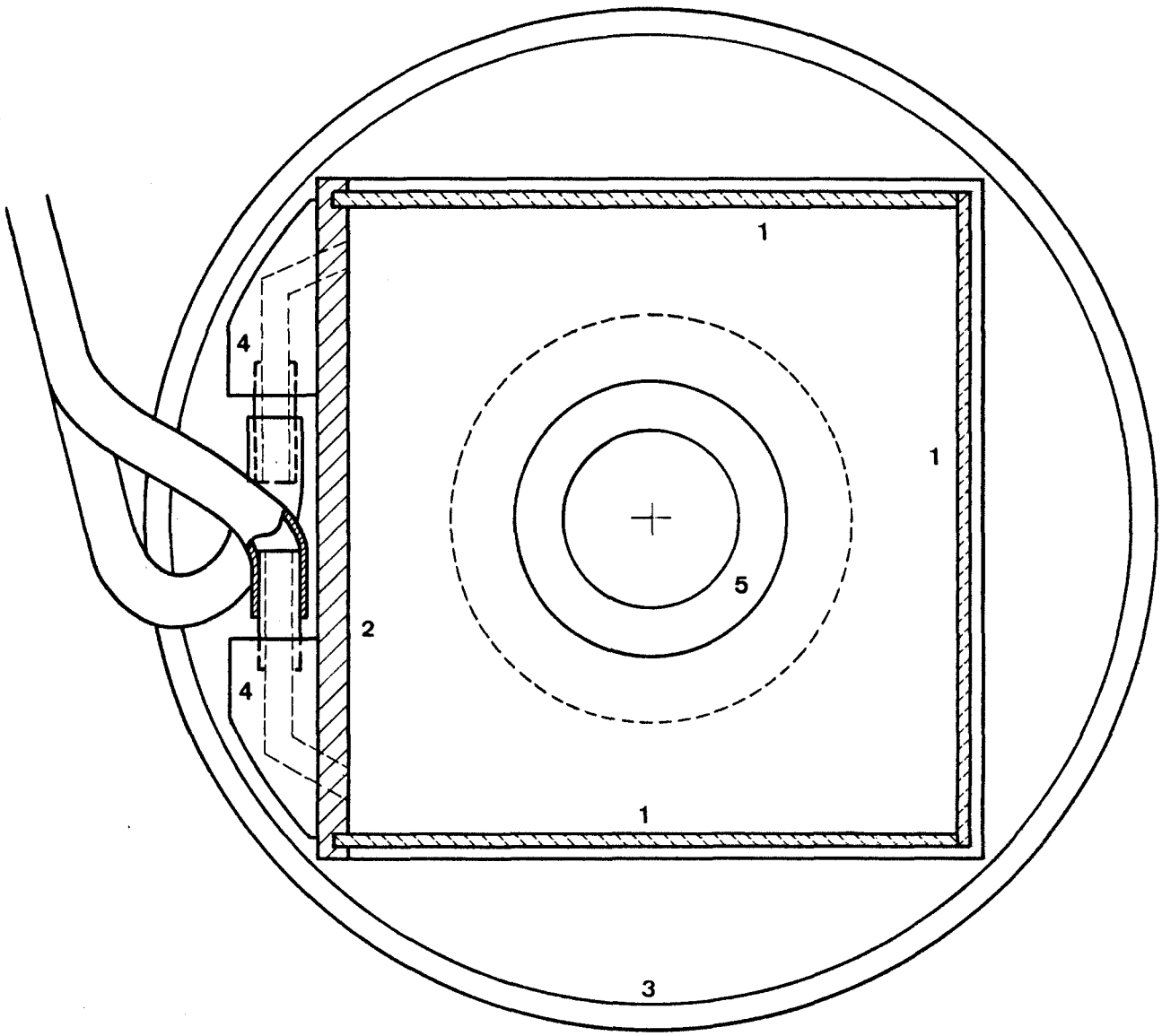

Fig. 4. Vista del tanque (PT2) según el eje de simetría. 1, paredes laterales de vidrio; 2, pared lateral de metacrilato; 3, pared frontal; 4, orificios de alimentación del líquido del baño; 5, juntas.

del baño, como ocurriría en el caso de un tanque abierto en la cara superior, tipo de tanque en la actualidad en uso en nuestro laboratorio.

La alimentación del líquido para el baño (bath liquid, BL) se realiza por medio de un recipiente externo (bath reservoir, BR) que contiene dicho líquido, y es trasvasado al interior del tanque por medio de un conducto de alimentación a través de un orificio practicado en la pared lateral de metacrilato. En dicha pared se encuentra también otro orificio, al cual está conectado un conducto de purga, con el fin de facilitar el llenado y la eliminación del aire contenido inicialmente en el tanque. Ambos conductos van provistos de sus correspondientes válvulas.

Los elementos auxiliares para montar el PT2 en una configuración cualquiera son los adaptadores del disco de inyección y del disco opuesto. Dado su carácter de acople entre el PT2 y el entorno específico que le rodea, la forma de los adaptadores refleja este carácter y por lo tanto son las partes que pueden estar sometidas a cambio de uno a otro montaje. Loas adaptadores desarrollados han sido diseñados para permitir el montaje en el FPM.

Así, en el seno del FPM, el adaptador del disco opuesto (rear plate adaptor, RPA) es soportado por fricción en el rebaje que encaja en el disco opuesto y la junta permite los movimientos de oscilación y de giro del RPA. Debido a la reducción efectiva de la máxima distancia de separación de los discos por la presencia de los adaptadores, el diámetro de los discos es de 30 mm frente a los 40 mm utilizados en el FPM.

En cuanto al adaptador del disco de inyección (front plate adaptor, FPA), está formado por un cilindro cuya superficie lateral, en contacto en todo momento con la junta de la pared frontal, mantie

ne la estanqueidad del tanque aun cuando se realicen desplazamientos de esta pieza. La cara de la sección recta del cilindro que permanece en el interior del tanque se utiliza como disco de inyección y el extremo opuesto va unido a una pletina que dispone de tornillos de fijación al cilindro soporte del disco de inyección. En el interior del FPA se encuentra el conducto de inyección que se acopla con el extremo del conducto del FPM. El tipo de sellado utilizado permite realizar las mismas operaciones que es capaz de efectuar el disco de inyección con el FPM libre: desplazamiento axial, movimiento de rotación y control del volumen del puente líquido.

3. Ensayos iniciales

Una vez construido el PT2 se han realizado unas primeras pruebas para estimar sus principales características, así como para encontrar los problemas que pudieran surgir tanto en su uso dentro de la cámara de ensayos del FPM en el curso de programas de entrenamiento como en sesiones de experimentación con puentes líquidos en este laboratorio. Para ello se ha montado el PT2 en un sencillo soporte que permitiese el desplazamiento del disco de inyección y la orientación del tanque con respecto a la vertical. Con ayuda de esta instalación se han formado zonas que se han sometido a diferentes orientaciones de la gravedad con respecto al eje de los discos. La microgravedad producida por una pequeña diferencia entre las densidades del líquido del baño y de la zona obliga a la entrefase de la zona a adoptar la forma de equilibrio apropiada que ya no será axilsimétrica, salvo cuando la vertical y el eje de la zona coincidan. Con el fin de ilustrar este fenómeno, en la Fig. 5 se muestra la forma de la entrefase de una zona sometida a una misma microgravedad cuya dirección adopta diversas orientaciones.

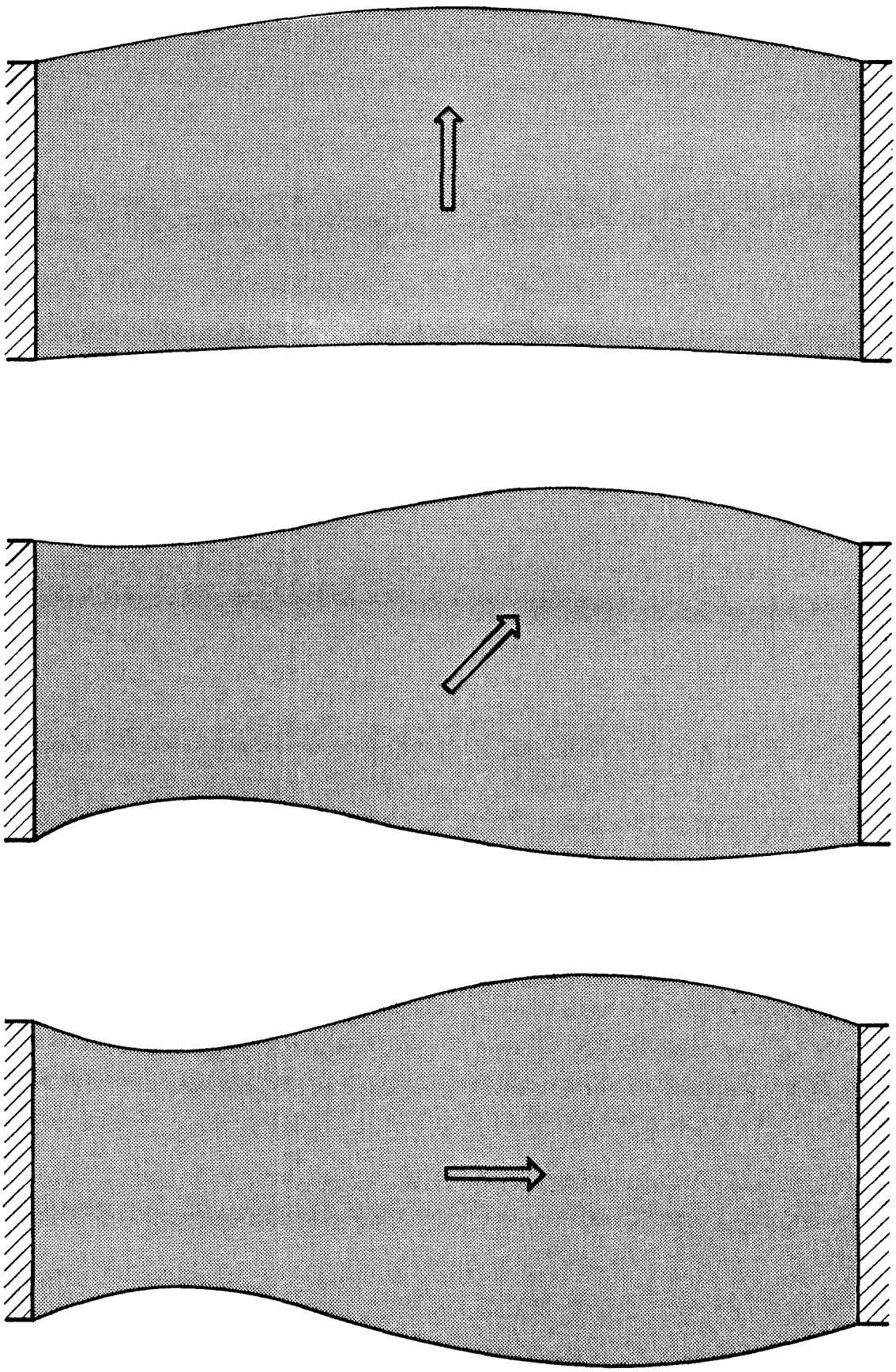

Fig. 5. Formas de la entrefase de una zona obtenidas a partir de fotografías tomadas durante pruebas con el PT2. La flecha indica la dirección de la microgravedad existente.

Entre los problemas detectados cabe destacar el de la imposibilidad, en la configuración actual, de introducir en el seno del baño cualquier elemento, tal como pinceles (utilizados habitualmente para la eliminación de burbujas de aire, sobre todo de las paredes de cristal a través de las cuales se observa la zona) y varillas para forzar la unión de las gotas formadas en la rotura. También sería de indudable interés el acondicionar la instalación para poder inducir la circulación de líquido del baño, siempre necesaria aunque en esta configuración el problema de la evaporación se haya eliminado.

De menor relevancia son las dificultades para llenar completamente el tanque, (lo que no es siempre necesario, aunque sea preferible no tener superficies libres dentro del tanque), así como la variación temporal de presión en el baño producida en la inyección o extracción de líquido de la zona por la pérdida de carga en los conductos de alimentación de líquido del baño y de purga, que conviene disminuir en lo posible con el fin de evitar sobrepresiones que podrían originar fugas momentáneas de líquido del tanque.

4. Instrucciones de montaje en el FPM

A la vista de la experiencia adquirida en las sesiones de manejo del FPM, y en los ensayos realizados en el laboratorio con el PT2, se han elaborado las siguientes instrucciones para el montaje del PT2 en la cámara de ensayos del FPM cuando éste se encuentra instalado en el interior del MSDR.

1. Extraer el FPM. Separar al máximo los discos. Abrir la cámara de ensayos. Colocar el disco de 60 mm como si fuera para el vuelo. Insertar el RPA.
2. Sujetar el FPA al disco de inyección.

3. Conectar los conductos de alimentación y de purga al PT2.
4. Montar el PT2 en la cámara de ensayos, apretando para forzar que el RPA penetre a través de la junta del PT2. Fijar el PT2 al orificio de la cámara de ensayos. Sacar los conductos a través de la ventana de la cámara.
5. Montar el conjunto disco de inyección + FPA en el cilindro soporte según el procedimiento usual. Llenar manualmente el conducto de inyección. Desplazar el FPA hasta que penetre a través de la junta del PT2. Poner a cero la separación de los discos.
6. Llenar el BR con el BL. Conectarle el conducto de alimentación. Sujetar el conducto de purga.
7. Abrir las válvulas y llenar el PT2. Podría emplearse uno de los siguientes métodos: llenar completamente el PT2 y no preocuparse en adelante del BL (deben eliminarse las burbujas de aire en la parte superior del PT2), o bien llenar del orden de los 4/5 del PT2 y cuidar de que se mantenga el nivel de BL durante las operaciones.
8. Empezar los ensayos.

SOPORTE DE LA MISION SPACELAB 1

1. Introducción

Con la proximidad de las fechas de lanzamiento se han multiplicado las actividades de soporte directo de la misión: preparación de la carga de vuelo, integración, últimas sesiones de entrenamiento, ensayo general de la misión, etc.

En algunos casos ha habido que realizar pequeños ajustes de última hora que dificultan el necesario control de materiales y procesos (nos referimos, por ejemplo, a los arreglos últimos de los depósitos de los líquidos tras descubrir una pequeña fuga, lo que obligó a vaciarlos y volverlos a llenar, con la consiguiente incertidumbre sobre contaminación y concentración de trazadores, pues la premura de tiempo y la logística asociada impidieron un estricto control de las operaciones).

En otros casos se trata de la incidencia de los dos meses de retraso en el lanzamiento sobre ciertos materiales perecederos. Por ejemplo, en abril último se procedió a realizar el tratamiento de los discos con una pintura especial, aquí en Madrid, y a finales de julio, ya dentro del Spacelab, se volvió a aplicar esta pintura. Como no se está seguro del envejecimiento del recubrimiento y el acceso al Spacelab es muy restringido, se ha añadido a la carga una muestra de pintura y un pincel para su aplicación, pero al necesitarse un calentamiento previo de la pintura, los problemas (afortunadamente ya resueltos) han sido considerables.

Ciñéndonos al Módulo de Física de Fluidos (FPM), los materiales embarcados en el Spacelab pueden dividirse en: 1) el FPM propiamente dicho, 2) el equipo auxiliar propio del FPM (herramientas

y útiles para su uso y piezas de repuesto), y 3) el equipo asociado a los experimentos en esta primera misión (líquidos, depósitos, discos, películas de cine y equipo auxiliar). Además, el Spacelab provee ciertos materiales de uso común, como toallas de papel, tan necesarias para la limpieza cuando se trabajo con líquidos no confinados.

Debido al desarrollo paralelo del FPM y los experimentos a realizar en esta primera misión, se ha tratado de que FIAT C.R. (Italia) que suministra el FPM se encargase también del desarrollo de depósitos, discos, equipo de registro de imagen, etc., para evitar interferencias en las interfases correspondientes.

Aunque los demás grupos usuarios del FPM se han visto obligados finalmente (algunos ya lo previeron en un principio) a suministrar algunas piezas propias para mejor adaptar el FPM disponible a sus necesidades actuales, en nuestro caso hemos podido llevar hasta sus últimas consecuencias esta filosofía de "evitar interfases" y sólo hemos tenido que suministrar las partículas usadas como trazadores en la visualización: no llega a un gramo de polvo (y aún esto en realidad se ha reducido a la selección del tamaño y concentración, pues el material bruto también fue suministrado por FIAT).

2. Formación de los astronautas

Tras el entrenamiento de Octubre-1982 se vio la conveniencia de insistir todavía más en la formación de los astronautas, no ya en los aspectos básicos de la Física de Fluidos en Microgravedad, sino en la interacción con los investigadores durante el vuelo.

Con este fin se prepararon dos sesiones más dedicadas específicamente al Banco Doble de Ciencia de los Materiales (MSDR) y en especial al Módulo de Física de Fluidos (FPM), la primera del

8 al 12 de Marzo y la segunda del 8 al 19 de Julio. De ellas se obtuvieron las siguientes consecuencias.

- el estado de los Procedimientos de ejecución de las secuencias de ensayos en vuelo es satisfactorio y a partir del 15 de Julio se consideran definitivos.
- el sistema de comunicaciones simulaba perfectamente la configuración esperada en Houston durante el vuelo, y todo el personal quedaba capacitado para su manejo. Desgraciadamente ha resultado algo engañosa esta simulación, pues los novísimos equipos usados en Colonia (Alemania) daban una fidelidad y sensibilidad muy superiores a los veteranos equipos de Houston (USA). En Alemania se podía seguir el desarrollo del experimento "de oído", pues los característicos ruidos de la cámara de cine, los motores, los interruptores, etc., todos ellos discernibles, permitían al investigador conocer exactamente el desarrollo del experimento.
- el grupo de supervisores de la NASA necesitaba ganar más confianza para permitir el uso discrecional de las comunicaciones a los investigadores del FPM. Se acordó intensificar esta interacción en el ensayo general de septiembre en Houston.
- el funcionamiento del grupo de apoyo científico (experimentadores en edificio contiguo al de control de operaciones) no pudo ser simulado fidedignamente ya que su misión principal es la de replantear el desarrollo de los experimentos del MSDR en conjunción con los del resto del Spacelab, y para ello se requiere una continuidad (24 horas diarias) que no podía alcanzarse en las 12 horas de jornada de tra-

bajo en Colonia. En realidad fue esta falta de continuidad la que impidió simular los relevos, tanto de los astronautas como de los experimentadores y el grupo de supervisores, que tanta importancia han demostrado tener en la simulación, más realista, en América.

- la preparación de la Documentación a aportar en caso (muy frecuente) de cambios sobre el plan previsto, es complicada y laboriosa, y el equipo de supervisores no estaba satisfecho con la situación actual. Por otra parte, los investigadores a su vez, se quejaban de la lentidud de esta burocracia.
- la simulación de ciertos problemas conflictivos dio origen a duras polémicas que han obligado a los responsables a establecer un riguroso orden de prioridades, favoreciendo a los ingenieros de sistemas (ver tabla 1), que deben velar por la seguridad y operatividad de los equipos, en posible detrimento de los experimentadores. La filosofía es que el primer vuelo del Spacelab (y del MSDR y el FPM) debe servir, como primer objetivo, para comprobar que funciona según el diseño, siendo la realización de experimentos un segundo (pero importante) objetivo que permita ilustrar sobre la amplia gama de utilizaciones que el laboratorio espacial puede tener.
- el último entrenamiento fue ya teniendo en cuenta que debido al fallo del satélite de comunicaciones TDRSS, el contacto por radio era menos frecuente.

Tabla 1.- Criterio de prioridades durante la ejecución de los experimentos en el Spacelab 1.

OPERATIONS GUIDELINES

1. ALWAYS WORK TO GET BACK TO THE MASTER T/L. SHOULD ANY EVENT INTERRUPT, MINIMIZE THE INTERRUPTIONS AND GET BACK TO THE T/L.

2. AN EXCEPTION TO THE SACRED NATURE OF THE MASTER T/L WOULD BE FOR 12 HOURS TUNING TO ADJUST FOR ORBITAL PREDICTION INACCURACIES. THE T/L SHOULD BE BUILT IN SUCH A WAY AS TO PERMIT SUCH UPDATES.

3. IF AN EXPERIMENT RUNS INTO TROUBLE, IT SHOULD NOT HAVE ACCESS TO ANOTHER EXPERIMENTS' TIME. (I.E.) - AN EXPERIMENT RUNNING OVER SHOULD BE TERMINATED: IT CAN BE COMPLETED ONLY IF IT DOES NOT IMPACT ANOTHER EXPERIMENT.

4. IF A SYSTEM FAILURE CAUSES AN EXPERIMENT OVERRUN, CUT IF OFF ANYWAY AT THE END OF ITS TIME BLOCK BUT REPLAN IT AS SOON AS T/L PERMITS. IF THERE ARE SYSTEM DROP-OUTS RETURN TO THE ORIGINAL T/L AFTER RECOVERY AND WORK TO INCLUDE THE AFFECTED EXPERIMENT AT SUBSEQUENT VACANCIES IN THE MASTER T/L.

5. EACH EXPERIMENTER SHOULD IDENTIFY HIS CONTINGENCY OPERATIONS. IF THE EXPERIMENT FAILS COMPLETELY, THE EXPERIMENTER SHOULD RELEASE HIS TIME.

6. RESUSITATION OF FAILED EXPERIMENTS USING CREW TIME OR OTHER RESOURCES NOT PREVIOUSLY PLANNED WOULD BE PERMITTED ONLY IF SUCH EXTRA RESOURCES WERE AVAILABLE AT THAT POINT IN THE MISSION. THEY WOULD NOT BE TAKEN FROM ANY OTHER EXPERIMENT.

7. IF EXTRA TIME IS AVAILABLE, SUBSTITUTE ONLY THOSE EXPERIMENTS WHICH FIT THE CURRENT CONFIGURATION (HRM, ATTITUDE, ETC.). FO'S THAT FIT A GIVEN CONFIGURATION WOULD BE AVAILABLE TO THE MISSION SCIENTIST FOR INCLUSION BASED ON THE ADVICE OF THE SCIENCE OPERATIONS PLANNING GROUP. SELECTION CRITERIA FOR THE F.O. TO BE SUBSTITUTED ARE AS FOLLOWS:

   A) CAN THE SUBSTITUTE FO OBTAIN USEFUL DATA IN THE TIME REMAINING (OR WILL IT ONLY REACH INITIALIZATION BY THE END OF THE OPPORTUNITY).

   B) FIRST PRIORITY SHOULD BE GIVEN TO AN EXPERIMENT ON THE SUBSTITUTE LIST THAT COINCIDENTALLY COULD USE THE OPPORTUNITY TO OBSERVE A RARE EVENT.

   C) NEXT, PRIORITY SHOULD BE GIVEN TO AN EXPERIMENT THAT HAS LOST OPPORTUNITIES DUE TO S/L AND FACILITY PROBLEMS.

   D) NEXT, PRIORITY SHOULD BE GIVEN TO A SUBSTITUTE THAT REQUIRES TROUBLESHOOTING AND COULD BEST UTILIZE THE OPPORTUNITY (AND POSSIBLY A FREE CREW MEMBER).

   E) NEXT, PRIORITY SHOULD BE GIVEN TO AN EXPERIMENT THAT HAS LOST OPPORTUNITIES DUE TO HARDWARE/SOFTWARE PROBLEMS FROM WHICH IT HAS NOW RECOVERED.

   F) RUN AN EXPERIMENT THAT HAS NOT PREVIOUSLY RECEIVED A FREED UP SLOT OVER ONE THAT HAS.

   G) GIVE PREFERENCE TO ANOTHER INVESTIGATION IN THE SAME DISCIPLINE GROUP, AS THIS GROUP WILL BE SUFFERING AS A RESULT OF THE FAILURE.

3. Ensayo general del vuelo

En una reunión previa celebrada en Munich (Alemania), del 22 al 24 de Agosto, el grupo de operaciones del MSDR discutió la necesidad de participar desde el mismo Centro de Control de Houston en el seguimiento de la misión, a pesar de que el Gobierno alemán ha puesto a punto un centro de seguimiento en Europa (con vista al control de la futura misión Spacelab D1 en 1985, en que también tomaremos parte). En esta reunión se puso de manifiesto el hecho significativo de que aunque en este vuelo inicial del Spacelab la carga de pago se reparte al 50 % entre la NASA y la ESA, en el área de Ciencia de los Materiales, la participación americana (y por tanto el interés de la NASA?) es muy pequeña.

El ensayo general tuvo lugar del 15 al 25 de Septiembre en Houston (USA). Allí surgieron nuevos problemas en el protocolo de comunicaciones y prioridades, y se puso de manifiesto la gran inercia de todo el sistema, con tiempos de espera de varias horas en la tramitación de solicitudes de cambio de secuencia. Téngase en cuenta que los experimentos de física de fluidos de este vuelo se realizan manualmente y en contacto continuo (siempre que haya cobertura de radio) con los experimentadores, sacando el máximo rendimiento a un laboratorio espacial habitado, a diferencia de otro tipo de experimentos más automáticos, donde, como en el caso de los hornos del propio MSDR, el control lo lleva un microprocesador y el análisis de resultados se hace a posteriori.

Además de la presencia en el Centro de Control de los experimentadores del FPM durante la ejecución de sus propios experimentos, se establecieron turnos de 6 horas para la permanencia continuada de un investigador del FPM en la sala del grupo de apoyo científico (en un edificio cercano).

Se verificaron también las comunicaciones de voz y datos con el centro de seguimiento europeo GSOC en Alemania desde donde participará uno de los experimentadores del FPM.

Al final de la simulación tuvo lugar una reunión de todos los experimentadores del Spacelab 1 y se reconoció la especial circunstancia de los experimentadores en el FPM, que requiere un tratamiento menos rígido por parte de los supervisores ya que consume poca potencia y es el operador quien controla completamente el aparato, con escasa incidencia sobre el resto del Spacelab.

4. Preparación de la carga de vuelo

Aparte del equipo básico del FPM, el experimento 1-ES-331 hace uso de los siguientes materiales:

- 2 depósitos para los líquidos. La ESA ha provisto de tres depósitos idénticos, diseñados por FIAT, para el Spacelab 1.
- 1300 cm^3 de aceite de silicona de baja viscosidad (DMS 5), provisto por ESTEC en calidad comercial y purificado por uno de los experimentadores (J. Padday). Este líquido va a ser compartido por dos experimentadores (L. Napolitano e I. Da Riva).
- 1300 cm^3 de aceite de silicona de alta viscosidad (DMS 100) en las mismas condiciones que el anterior, pero a compartir entre cuatro experimentadores (Padday, Haynes, Napolitano y Da Riva).
- dos muestras de 0.4 gramos de polvo cerámico (Eccospheres, FA-A) suministradas en bruto por Emerson & Cuming a FIAT y seleccionadas en tamaño y cantidad por nosotros (ver tabla 2) para mezclado con el aceite antes descrito, con objeto de que sirvan de trazadores del movimento. La adición de traza-

Tabla 2.- Normas de preparación de la mezcla de trazadores para el Spacelab 1.

TRACER MIXTURE PREPARATION

by I. Martínez. 5-APRIL-83

GENERAL

Small ceramic spheres are used to visualize motion inside the liquid bridge of silicone oil.

These hollow spheres do not tend to coalesce, but do show some adhesion to solid walls and interfaces. Besides shaking instructions to the crew before reservoir installation in flight, some extra amount of tracers is accounted for to compensate for that. The tracers will be added during the final filling of the reservoirs on ground.

Homogeneity of size and shape is desired (brittles and powder tend to mask the photographic scene), and best results on trials have been obtained with ASTM gauge no. 270, corresponding to particles of 53 to 74 microns, though any near value would work.

To keep contamination to a minimum, a strong mixture will be prepared, adding to the preweighed sample of 0.40 grams of tracers per reservoir some 10 cm^3 of the corresponding oil: i.e., one to the 100 centistokes oil and the other to one of the two 5 centistokes oil.

Three identical tracer samples are provided, one for each of the two reservoirs with tracers, and a spare one.

PROCEDURES TO ADD THE TRACERS

1. The reservoirs to hold oil with tracers should be half filled with oil first.
2. Then, pour some 10 cm^3 of the same oil into one of the test tubes supplied with tracers.
3. Put the cork back and shake the tube vigorously until a homogeneous mixture is apparent.
4. Add the strong mixture to the half filled reservoir.
5. Refill once or twicethe test tube to rinse the walls of any tracers left, adding the rinsing oil to the half filled reservoir.
6. Complete the filling of the reservoir with the rest of oil.
7. Repeat similarly with the other reservoir of oil with different viscosity.
8. Once the filling completed, shake the reservoir with a gentle turning oscillation.
9. No verification of the reservoir contents is foreseen.

dores es requerida en los experimentos de Napolitano y Da Riva, pero por cuestiones logísticas también serán usados por Padday y Haynes.

- un disco de inyección de 40 mm de diámetro en su superficie de trabajo, con un resalte de 0.5 mm para anclaje del líquido, y con orificio central de 6 mm de diámetro para la inyección. Este disco ha sido suministrado por FIAT y tratado con pintura antimigratoria en su superficie exterior por J. Padday (quien ha desarrollado la pintura). Va a ser usado en los experimentos de Da Riva y Haynes.
- un disco frontal (opuesto al de inyección) de 40 mm de diámetro con un resalte de 0.5 mm para el anclaje del líquido. Este disco, también suministrado por FIAT, va a usarse exclusívamente en el Exp. 1-ES-331.
- dos casettes cargados con película de cine de 16 mm, en blanco y negro, con un total de 4500 fotogramas disponibles, suministrados gratuitamente por KODAK, que también se ha ofrecido a revelar la película y entregarla a los experimentadores.

Además de este equipo embarcado, la ESA proveerá cintas magnéticas donde se grabarán, desde el centro de seguimiento de Alemania, los datos transmitidos por el Sapcelab durante el vuelo sobre los parámetros de funcionamiento del FPM.

LISTA DE SIMBOLOS

A, Amplitud de la deformación de la entrefase respecto de la forma cilíndrica, [m].

A_e, Amplitud del movimiento de oscilación del disco excitador, [m].

B, Radio del recipiente cilíndrico que contiene el baño (posición de la pared), adimensionalizado con R.

Bo, Número de Bond: $Bo = \delta\rho R^2 g/\sigma$.

F, Radio de la superficie libre, adimensionalizado con R.

I_o, I_1, Funciones hiperbólicas de Bessel de primera especie, de orden cero y primer orden, respectivamente.

K_o, K_1, Funciones hiperbólicas de Bessel de segunda especie, de orden cero y primer orden, respectivamente.

L, Longitud de la zona, [m].

L, Función auxiliar adimensional, $L = Q^2/(B^2-S)$.

M_i, Peso molecular del constituyente i de una mezcla, $[kg.mol^{-1}]$.

N, Número de puntos experimentales.

OL, Eje de simetría de la construcción geométrica de la Fig. A1-1.

OM, Distancia de la rejilla difusora al eje de la zona, [m].

OS_1, OS_2, Distancia de los rayos luminosos en su recorrido por el medio exterior al eje de la zona, [m].

P, Presión capilar, adimensional.

P, Anexo 1: punto que representa una línea longitudinal de la rejilla difusora.

P^j, Presión en el medio j, [Pa].

P_1, Presión de referencia, [Pa].

P^j, Presión reducida en el medio j, $(P^j-P_1)/\rho^i$, adimensionalizada con $\sigma/(\rho^i R)$.

P_i, Refractividad molecular del constituyente i de una mezcla, $[m^3.mol^{-1}]$.

PM, Distancia, para el observador, del punto P al eje de la zona, [m].

P'M', Distancia, para el observador, de la imagen del punto P al eje de la zona, [m].

Q, Variable adimensional utilizada en la integración numérica de las ecuaciones generales del modelo unidimensional, $Q = F^2W^i$.

Q*, Valor de Q en el caso de un puente líquido aislado.

R, Radio de los discos, [m].

R, Función auxiliar adimensional que contiene la influencia de la relación de densidades, $R = \rho S/[B^2-S(1-\rho)]$.

S, Variable adimensional utilizada en la integración numérica de las ecuaciones generales del modelo unidimensional, $S = F^2$.

S_n, Coeficiente auxiliar, adimensional.

S_σ, Desviación típica del conjunto de σ_i, $[kg.s^{-2}]$.

T, Temperatura del baño, [°C].

T_b, Tiempo de rotura adimensionalizado con $(\rho^i R^3/\sigma)^{1/2}$.

T_{bo}, Valor de T_b en el caso de un puente líquido aislado.

T_{lb}, Tiempo de rotura obtenido a partir del modelo unidimensional linealizado, adimensionalizado con $(\rho^i R^3/\sigma)^{1/2}$.

T_{lb_o}, Valor de T_{lb} en el caso de un puente líquido aislado.

U^j, Componente radial de la velocidad en el médio j, adimensionalizada con $(\rho^i R/\sigma)^{-1/2}$.

U_c^j, Velocidad característica radial en el medio j, $[m.s^{-1}]$

V_p, Volumen parcial de rotura (relación del volumen de una de las gotas producidas en la rotura al volumen total de la zona).

V_{p_o}, Valor de V_p en el caso de un puente líquido aislado.

W^j, Componente axial de la velocidad en el medio j, adimensionalizada con $(\rho^i R/\sigma)^{-1/2}$.

W_c^j, Velocidad característica axial en el medio j, $[m.s^{-1}]$.

a, b, a_n, b_n, c_n, Constantes adimensionales.

$d(\sigma,B)$, Desviación media cuadrática entre las pulsaciones adimensionales teóricas y experimentales.

f, Deformación de la entrefase respecto a la forma cilíndrica, adimensional.

f_e, Frecuencia de oscilación del movimiento del disco excitador, [Hz].

f_g, Distancia focal equivalente de una lente gruesa, [m].

f_{min}, Valor mínimo de f.

f_R, Frecuencia de resonancia, [Hz].

f_{Ri}, Valor de la variable f_R obtenido en el experimento i, [Hz].

g, Aceleración de la gravedad, $g = 9.81\ m.s^{-2}$.

g^j, g_o, Constantes adimensionales.

h, Factor de proporcionalidad entre el número de Bond, Bo, y la diferencia de densidades, $\delta\rho$, $h = gR^2/\sigma$, $[kg^{-1}.m^3]$.

i_n, j_n, k_n, l_n, Coeficientes auxiliares, adimensionales.

n, Anexo 2: índice de refracción.

n^j, Indice de refracción del medio j.

p^j, Presión reducida de perturbación, adimensional.

r, Coordenada radial, adimensionalizada con R.

s, Coeficiente que distingue las deformaciones simétricas (s = 2) de las antisimétricas (s = 1).

t, Tiempo, [s].

t, Tiempo, adimensionalizado con $(\rho^i R^3/\sigma)^{1/2}$.

u^j, Velocidad radial de perturbación, adimensional.

w^j, Velocidad axial de perturbación, adimensional.

x_w, Fracción en peso de metanol de una mezcla de metanol y agua.

x_{w_i}, Fracción en peso del constituyente i de una mezcla.

x_v, Fracción en volumen de metanol de una mezcla de metanol y agua.

z, Coordenada axial, adimensionalizada con R.

z_m, Valor de z para el que se produce la máxima deformación de la entrefase de la zona respecto de la forma cilíndrica.

Λ, Esbeltez de la zona, $\Lambda = L/(2R)$.

Δ, Indica la variación experimentada por la variable a la que precede.

Δ_r, Variación según la coordenada radial.

$\mathbf{\Omega}$, Pulsación del movimiento de oscilación o factor de amplificación, $[s^{-1}]$.

Ω, Exponente adimensional del factor temporal de la solución de los problemas linealizados.

Ω_o, Valor de Ω en el caso de un puente líquido aislado.

Ω_p, Uno de los diversos valores de Ω que se obtienen como solución de la ecuación característica para un valor dado de Λ.

α, β, Parámetros auxiliares adimensionales empleados en la solución del problema unidimensional linealizado.

α, Anexo 1: ángulo formado por el eje óptico OM y la línea que une el punto P y el centro de la sección de la zona (ver Figura A1-1).

β, Anexo 1: diferencia entre los ángulos que forma un rayo luminoso con la normal a la entrefase en cada uno de los medios que atraviesa, $\beta = \theta^o - \theta^i$ (ver Figura A1-1).

γ, Factor de amplificación, amortiguamiento (adimensional).

γ, Anexo 1: ángulo formado por el rayo que parte del punto P de la rejilla y la línea que une P con el centro de la sección de la zona (ver Figura A1-1).

γ_o, Valor de γ en el caso del puente aislado.

δr, Deformación máxima de la zona respecto de la forma cilíndrica, adimensionalizada con R.

$\delta\rho$, Diferencia entre la densidad del líquido interior y el del baño, $\delta\rho = \rho^i - \rho^o$.

ε, Parámetro pequeño adimensional que mide, en general, la máxima deformación inicial de la superficie libre.

θ^j, Angulo formado por un rayo luminoso y la normal a la entrefase en el medio j.

λ, Longitud característica de la deformación de la entrefase, cuyo valor es la longitud de la zona dividida por el número de ondas de la deformación, [m].

ν, Viscosidad cinemática, $[m^2.s^{-1}]$.

ν^o, Viscosidad cinemática de una mezcla de metanol y agua, $[m^2.s^{-1}]$.

ρ, Relación entre las densidades del líquido del baño y de la zona, $\rho = \rho^o/\rho^i$.

ρ, Anexo 2: densidad, $[kg.m^{-3}]$.

ρ^j, Densidad del medio j, $[kg.m^{-3}]$.

σ, Tensión interfacial, $[kg.s^{-2}]$.

σ_i, Valor de la tensión interfacial calculado a partir del valor de la frecuencia de resonancia determinada en el experimento i, $[kg.s^{-2}]$.

$\overline{\sigma}_i$, Valor medio del conjunto de σ_i, $[kg.s^{-2}]$.

$\sigma^*(B)$, Valor de la tensión interfacial para el que se produce el mínimo de la función $d(\sigma,B)_{B=cte}$, $[kg.s^{-2}]$.

σ^*_m, Valor de la tensión interfacial para el que se produce el mínimo de la función $d(\sigma^*(B),B)$, $[kg.s^{-2}]$.

ω, Pulsación adimensional.

ω_o, Valor de ω en el caso de un puente líquido aislado.

ω_{E_i}, Valor de ω obtenido en el experimento i.

ω_{T_i}, Valor de ω obtenido teóricamente para la configuración del experimento i.

Superíndices

j, Indica la región en la que está definida la cantidad en consideración: i, líquido de la zona; o, baño.

Subíndices

r,t,z, Indican, respectivamente, derivación respecto a la coordenada radial, al tiempo y a la coordenada axial, adimensionales.